Toward an Automated System
for the Analysis of Cell Behavior:
Cellular Event Detection and Cell Tracking
in Time-lapse Live Cell Microscopy

Seungil Huh

CMU-RI-TR-13-06

*Submitted in partial fulfillment of the
requirements for the degree of
Doctor of Philosophy in Robotics.*

The Robotics Institute
Carnegie Mellon University
Pittsburgh, PA 15213

February 2013

Thesis Committee:
Takeo Kanade, Co-chair
Stephen E. Fienberg, Co-chair
Robert F. Murphy
Fernando De la Torre
Alan J. Russell

Abstract

Time-lapse live cell imaging has been increasingly employed by biological and biomedical researchers to understand the underlying mechanisms in cell physiology and development by investigating behavior of cells. This trend has led to a huge amount of image data, the analysis of which becomes a bottleneck in related research. Consequently, how to efficiently analyze the data is emerging as one of the major challenges in the fields.

Computer vision analysis of non-fluorescent microscopy images, representatively phase-contrast microscopy images, promises to realize a long-term monitoring of live cell behavior with minimal perturbation and human intervention. To take a step forward to such a system, this thesis proposes computer vision algorithms that monitor cell growth, migration, and differentiation by detecting three cellular events—mitosis (cell division), apoptosis (programmed cell death), and differentiation—and tracking individual cells. Among the cellular events, to the best our knowledge, apoptosis and a certain type of differentiation, namely muscle myotubes, have never been detected without fluorescent labeling. We address these challenging problems by developing computer vision algorithms adopting phase contrast microscopy. We also significantly improve the accuracy of mitosis detection and cell tracking in phase contrast microscopy over previous methods, particularly under non-trivial conditions, such as high cell density or confluence. We demonstrate the usefulness of our methods in biological research by analyzing cell behavior in scratch wound healing assays. The automated system that we are pursuing would lead to a new paradigm of biological research by enabling quantitative and individualized assessment in behavior of a large population of intact cells.

This dissertation is dedicated to

my beloved wife Song and little girl Ellie.

Acknowledgments

I have received many blessings over the last several years of my doctoral studies.

First, I would like to thank my advisors, Takeo Kanade and Stephen E. Fienberg, who are not only world-class pioneers and visionaries in the field, but also considerate mentors to me. I would not be here without their advice and guidance.

I also want to thank the other members of my thesis committee, Robert F. Murphy, Fernando De la Torre, and Alan J. Russell, for their insightful comments and encouragements.

I am grateful to have the opportunity to work with the colleagues in my research group and my collaborators. I would especially like to thank Phil G. Campbell, Lee E. Weiss, Dai Fei E. Ker, Mei Chen, Silvina N. Junkers, Sho Sanami, Hang Su, Ryoma Bise, Sungeun Eom, Zhaozheng Yin, and Jinseok Park.

I am blessed to have many good friends here in Pittsburgh, each of whom I would like to name unless there were too many. Their friendships have never allowed me to be depressed during my graduate studies and made me love the life in Pittsburgh.

I would like to express gratitude to my family members in South Korea, especially my parents and parents-in-law for many years of unconditional love and continuous prayers.

Song, my beloved wife, and Ellie, my tiny girl, thank you for your love and your being. I am grateful for the time we have been together and also for our journey ahead toward our dreams.

Finally, I would like to give my utmost thanks to God, who is gracious to me during my entire life as well as my doctoral studies. I am excited in the next adventure that He is planning for me. "Speak, for your servant is listening."

Contents

List of Figures

List of Tables

Chapter 1

Introduction

In recent years, as microscopy imaging technology has been improved and automated, tremendous volumes of microscopy image data are being generated in biology and biomedical science fields [16, 91, 101]. Accordingly, how to efficiently process and analyze the data becomes one of the major issues in the fields since manual analysis is often not feasible any more [38, 103]. This challenge leads to rapidly increasing attention to systems for bioimage analysis based on computer vision or image processing algorithms that enable automated and quantitative analysis of visual data.

Monitoring the behavior of live cells, particularly cell growth, migration, and differentiation, is of great importance in order to understand the underlying mechanisms of cell physiology and development [6]. For instance, monitoring cell growth and differentiation is critical for extending our knowledge of both normal and aberrant cell behavior in physiological processes, such as proper organ development [124], virus replication [28], and cancer development [3]. Quantitative analysis of cell migration is also crucial for investigating several biological phenomena that involve cell migration, such as embryonic development [64], wound healing process [29], and metastasis [3].

In this work, we propose a computer vision-based system that detects cellular events and tracks individual cells in order to realize an automated long-term monitoring of cell behavior.

The system detects cell division and cell death to measure cell growth, tracks cells to quantify cell migration, and locates differentiated cells to capture cell differentiation. This system aims at helping researchers in biological or biomedical sciences to more efficiently determine the effect of exogenous biochemical or physical signals on the activity of cells, e.g., expansion of cells with minimal cell death or loss of their self-renewal capability.

In the rest of this section, we introduce the historical background of our work, outline the scope of our research, present thesis contributions, and overview the thesis.

1.1   Background and Motivation

In this section, we briefly explore the background and motivation of our research. The previous work closely related to our thesis work will be reviewed later in more detail.

Automation of the acquisition and interpretation of data in microscopy began in 1950s and 1960s [85, 86, 93, 105, 122]. These early works first digitalized optical information in microscopy cell images and then employed image processing to obtain basic measurements, such as cell count and cell size. They also computed various types of features, e.g., nuclear area and optical density frequency distribution, based on which further analyses, such as cell type classification and cell morphology analysis, were performed. These kinds of approaches were innovative, but had not gained serious attention until recently when the data became too cumbersome for one person or a small group of people to manually analyze.

As advanced technology in microscopy has allowed to capture more precise details and facilitated image acquisition through automation [10, 16, 27, 49, 91, 116], not only has the amount of data exceeded the capacity of manual analysis, but also the complexity of tasks has become significantly increased. In order to meet these demands, in the late 1990s, computer vision or image processing methods began to be broadly applied to high-throughput microscopy image analysis [14]. As a result, in the last decade, there has been a great improvement particularly in automatic analysis of fluorescent microscopy images, where regions and phenomena of interest

are labeled by fluorescent markers, such as red/green fluorescent protein (RFP/GFP) [77], fluorescently labeled antibodies, and many other stains. The achievements in fluorescent microscopy image analysis include, but not limited to: classification of cell types and protein subcellular location images, 2D/3D segmentation of cells and nuclei, multiple cell tracking, and other computational image analyses [14, 18, 19, 33, 76, 120].

Despite the great success in fluorescent microscopy imaging and analysis, the application of fluorescent microscopy to capturing dynamics of live cells is quite limited, mainly due to phototoxicity and photobleaching. Phototoxicity often occurs during the process of time-lapse fluorescent microscopy imaging as cells containing fluorescence are repeatedly exposed to illumination and in response the fluorescent molecules tend to generate reactive chemical species, such as oxygen radicals. These free radicals subsequently damage subcellular components, and thus often affect cell behavior and fate [30, 31]. Furthermore, photobleaching or loss of fluorescence signal due to the loss of fluorophores' ability to fluoresce during time-lapse imaging limits the number of image acquisitions, preventing a long-time monitoring of cells [9, 44]. In addition, the utility of fluorescent microscopy is limited in that it only allows observation of fluorescently labeled structures.

Hence, monitoring of live cells for a long duration mostly uses non-fluorescent (transmitted and reflected light) live cell microscopy. And unfortunately, the analysis of the microscopy images is heavily reliant on manual annotation due to the lack of proper computer vision methods. Considering the importance of monitoring live cells as a fundamental study for a variety of applications, it is imperative to develop an automated system to analyze cell behavior in time-lapse non-fluorescent live cell microscopy. Such a system will not only accelerate the processing of cell behavior analysis, but also lead to a new design of research in biological science and biomedical engineering since it provides a new methodology in quantitative and individualized analysis of cell behavior with minimal perturbation and human intervention.

(a)	(b)	(c)	(d)
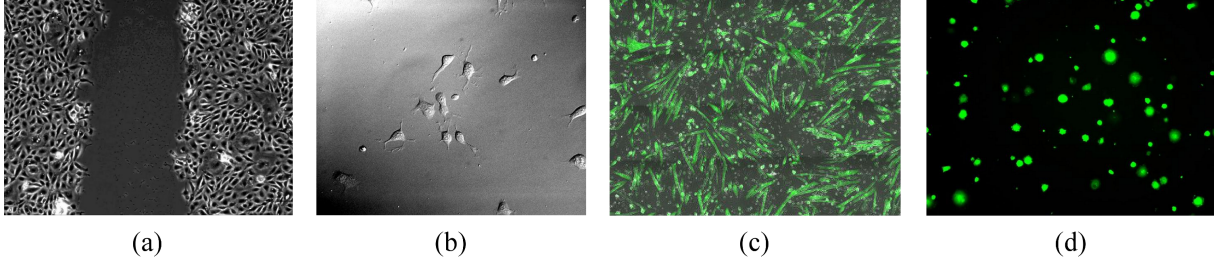
Figure 1.1: Sample images from different microscopy imaging methods: (a) phase contrast image, (b) differential interference contrast image, (c) immunohistochemically stained image (overlaid with a bright field image), and (d) green fluorescent protein (GFP) image. Non-fluorescent microscopy images ((a) and (b)) allow monitoring of live and intact cells for a long time period, but are more difficult to analyze due to lack of guidance. On the other hand, fluorescent microscopy images ((c) and (d)) are relatively easy to process due to the fluorescent marker labeling regions of interest, but allow only one time point observation of fixed cells ((c)) or a short-term monitoring of live cells ((d)). In this thesis, we use non-fluorescent microscopy images.

1.2   Goals and Scope

The goal of this thesis is to develop computer vision-based methods that monitor various behaviors of cells over a long-time period.

Among various microscopy modalities, we have chosen to use phase contrast microscopy [8]. This microscopy imaging methods do not involve any process that may affect cell behavior, allowing for a long-term monitoring of live and intact cells. On the other hand, most of the current high-throughput image analysis approaches resort to the use of immunohistochemically stained images or fluorescent protein tagging. Aforementioned, with this fluorescent microscopy only a one-time measurement or a short-term monitoring of cells is allowed due to the fixation or phototoxicity of reagents used, respectively. Figure 1.1 demonstrates examples of non-fluorescent and fluorescent microscopy images.

The scope of this dissertation work is divided into three detection and one tracking tasks: mitosis (cell division) detection, apoptosis (programmed cell death) detection, differentiation detection, and cell tracking, as shown in Figure 1.2. Note that among different kinds of cell deaths, i.e., apoptosis (programmed cell death) and necrosis (uncontrolled or traumatic cell death), we
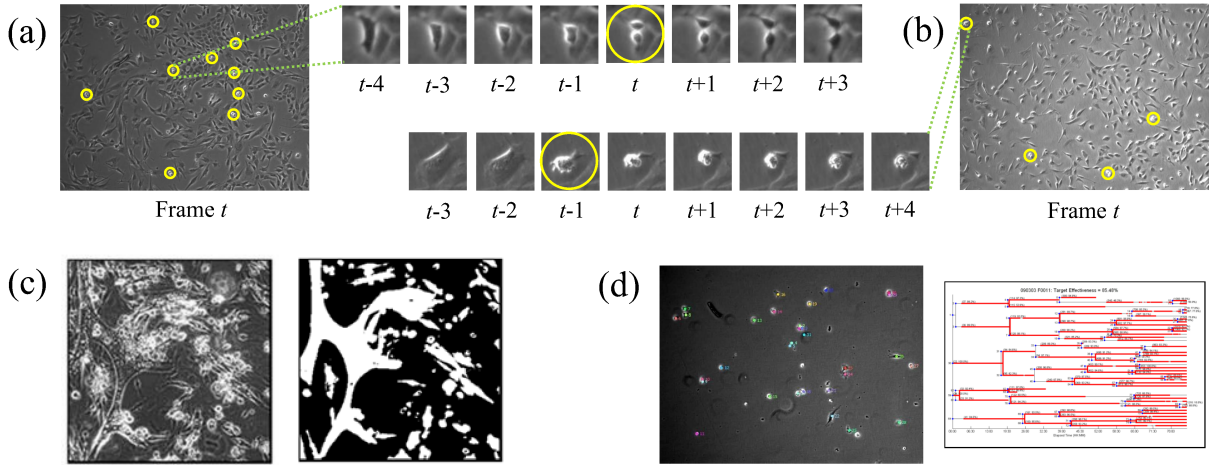
Figure 1.2: Scope of this dissertation work: (a) mitosis (cell division) detection, (b) apoptosis (programmed cell death) detection, (c) differentiation detection, and (d) cell tracking. In (a) and (b), yellow circles enclose the completion of mitosis and the initiation of apoptosis, respectively. In (c), the binary image represents differentiated cell regions in the phase contrast microscopy image. In (d), individual cells are tracked over time and cell lineages (the biologist's equivalent of family trees which describes mother-daughter cell relationships) are constructed.

detect apoptosis, which is the most common and of the most interest in the community. While not entirely comprehensive, these tasks cover most of important cell behaviors—detection of mitosis and apoptosis monitors the proliferative activity of cells and measures the growth of a cell population; detection of differentiation monitors cell fate, the process whereby a cell acquires a specialized phenotype to perform specific tasks related to its tissue function; cell tracking characterizes various types of cell behavior including cell area and shape, cell cycle length, and migration direction and speed.

Mitosis and apoptosis detections specify the time and location that each of mitotic and apoptotic processes is completed or initiated in time-lapse microscopy images, respectively. Differentiation detection locates differentiated cells in each frame. Cell tracking involves segmenting cells at each frame, maintaining cell identities over time, and constructing a cell lineage tree that illustrates the relationship between mother and daughter cells.

Automated cell behavior analysis in our problem setting meets following challenges:

- The major difficulty of microscopy cell image analysis lies in properties of the images.

5

Cells under non-fluorescent microscopy often do not have distinctive textures, have a highly amorphous shape, form a cluster involving blurred boundaries, and have boundary-like structures within cells [100]. In addition, artifacts, such as bright halos, often appear when cells form a cluster or undergo a certain process, which makes image processing more complicated. In contrast to fluorescent microscopy, non-fluorescent microscopy does not take advantage of fluorescent marker, thus detection of interest regions is not trivial.

- Another difficulty stems from a variety of cell types, culture conditions, and imaging conditions. Different types of cells often show significant variance in cell appearance and behavior. Within the same cell type, such variance may not be trivial as culture conditions vary since different biochemical or physical signals induce different cell behavior. Even with the same cell type and culture condition, images are often quite different over experiments depending on several factors including microscope model, illumination, and focus. To develop universal methods that can be applied to any cell type is hardly attainable due to non-trivial variance; on the other hand, to develop methods for each cell and condition is unrealistic due to the large number of cell types and conditions.

One would think that live cell microscopy image analysis is a mere application of start-of-the-art computer vision techniques. In fact, benefits from computer vision methods developed for general image and video analysis are quite limited. In other words, event detection and object tracking methods that have been developed in the computer vision field may provide some ideas, but most of the frameworks and methods are neither applicable to nor effective for live cell microscopy image analysis. In computer vision, event detection in video and object tracking are active and popular topics, e.g., abnormality detection [81, 130], human action detection [68, 82], face tracking [63], pedestrian tracking [7], and vehicle tracking [20]. However, the methods do not take into account major behavior that cells show, such as division and differentiation, simply because the objects that interest the community do not show such behavior. Moreover, recent algorithms in the field often too much rely on domain knowledge of target objects, such as facial

landmark locations for face tracking or human body pose for human action detection, in order to be generalized and applicable to microscopy images for cells, which are often amorphous and do not have any landmark. For the same reason, sliding window schemes [22, 115] and typical interest region detection schemes [48, 87], which are popularly used in computer vision to detect objects and reduce the search space, respectively, are not effective in candidate detection for cellular event detection and cell region detection for cell tracking.

1.3 Thesis Contributions

The contributions of this thesis work can be summarized as follows:

- We pursue a comprehensive system for automated cell behavior analysis without compromising viability and intactness of cells by adopting non-fluorescent microscopy. Among cell behavior that we listed (mitosis, apoptosis, migration, and differentiation), to the best of our knowledge, detection of apoptosis and detection of a certain type of differentiation, namely muscle myotubes, have never been proposed in non-fluorescent microscopy without fluorescent labeling. We address these challenging problems by developing computer vision algorithms adopting phase contrast microscopy. We also significantly improve the accuracy of mitosis detection and cell tracking in phase contrast microscopy under nontrivial conditions, such as high cell confluence.

- We show that the performance of cell behavior analysis can be enhanced by reflecting domain knowledge of cell behavior and cell microscopy. In our work, cell region and event candidate region detections are more effectively performed by understanding and modeling the image formation process in the phase contrast microscope. Mitotic events are also more accurately detected by developing new temporal models that jointly model visual dynamics of the mitotic and post-mitotic processes.

- We formulate an effective framework for cellular event detection consisting of three steps:

7
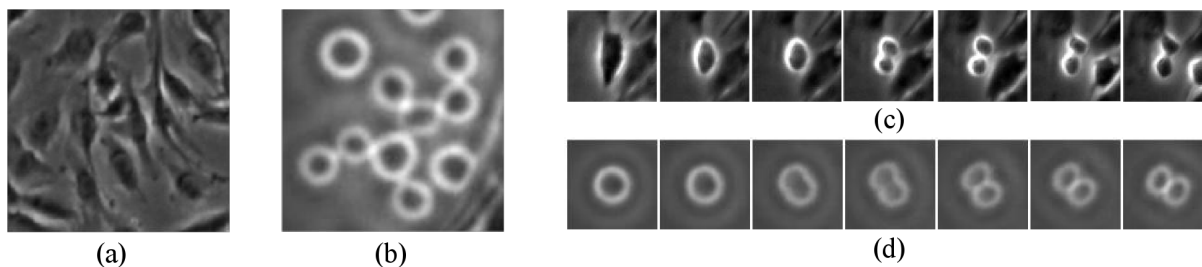
Figure 1.3: Sample images showing (a) adherent and (b) non-adherent cells in phase contrast microscopy. Sub-figures (c) and (d) show typical mitotic events of adherent and non-adherent cells, respectively. As shown in these figures, adherent cells show dramatic morphological and brightness changes during the mitotic process; on the other hand, non-adherent cells are not accompanied by dramatic alterations in cell shape and intensity during mitosis.

detection of candidates, incorporation of temporal information, and validation of the candidates. In this framework, the search space is first reduced by candidate detection using a simple model and subsequently the candidates are validated by a more complicated model; as a result, both efficiency and effectiveness are achieved.

- We propose and develop methods to address variance in cell appearance and behavior within and across cell types. Within the same cell type, we employ machine learning methods for candidate detection and validation to statistically handle the variance. In this framework, events are defined by examples annotated by human, and thus small variance can be dealt with by sufficient labeled samples along with effective models. Across cell types, we categorize cell types into two groups: adherent cells and non-adherent cells. Figure 1.3 clearly demonstrates the visual difference between these two groups of cells. Adherent cells are attached to a petri dish and thus typically show an amorphous shape as it stretches out on the dish. On the other hand, non-adherent cells float or are suspended freely in the culture medium and thus show a circular or elliptical shape. We develop cellular events and tracking methods for these two groups of cells to cover a major portion of cell types.

- We claim that cellular event detection and cell tracking bolster the other's performance, and empirically substantiate the claim. In our work, mitosis detection provides information on

time and location that each cell trajectory needs to branch, thereby considerably improving the quality of cell lineage construction. Similarly, cell tracking determines when and where each cell trajectory is terminated or lost, providing candidates for mitosis and apoptosis.

1.4 Thesis Overview

The remainder of this dissertation is organized as follows:

- In Chapter 2, we introduce our three detection tasks—mitosis, apoptosis, and differentiation detection—and cell tracking task in more detail. In addition, we overview the previous vision-based methods for event detection in non-fluorescent microscopy and previous cell tracking algorithms.

- In Chapter 3, we define the task of mitosis detection and present mitosis detection methods and results on adherent and non-adherent cell populations. For the methods, we propose new temporal probabilistic models that simultaneously validate whether a candidate patch sequence shows mitosis occurrence in it and determine when the mitosis is completed in the sequence, if it determined to occur. We also demonstrate that our mitosis detection method can be applied to the analysis of wound healing assay.

- In Chapter 4, we define the task of apoptosis detection and present apoptosis detection methods and results on adherent and non-adherent cell populations. For adherent cells, we propose a candidate detection method based on the phase contrast microscopy image formation process. For non-adherent cells, we propose a semi-supervised learning framework for apoptosis detection.

- In Chapter 5, we define the task of differentiation detection and present a supervised learning framework for differentiation detection. As the first step of the framework, we propose diffraction pattern filtering that enhances the quality of phase contrast microscopy based on the image formation model. We apply the framework to C2C12 myoblastic stem cell

populations for myotube detection and report the results.

- In Chapter 6, we present cell tracking algorithms that incorporate mitosis detection functionality, and show that independently performed mitosis detection can significantly improve cell tracking accuracy. We also empirically demonstrate that our cell tracking method outperforms state-of-the-art methods. In addition, we introduce the application of our tracking method to the analysis of wound healing process.

- Finally, we conclude the thesis with discussion and future research direction in Chapter 7.

Chapter 2

Cellular Event Detection and Cell Tracking in Time-lapse Non-fluorescent Microscopy

In order to realize an automated system for the analysis of cell behavior including cell proliferation, fate, and migration, we focus on the detection of three types of cellular events—mitosis, apoptosis, and differentiation—and the tracking of cells. In this section, we explain the processes of these cellular events and the benefits of detection of the events. We also review previous vision-based algorithms for the cellular event detection in non-fluorescent microscopy and previous cell tracking algorithms.

2.1   Mitosis and Mitosis Detection

Mitosis is the process whereby the genetic material of a eukaryotic cell is equally distributed between its descendants through nuclear division, resulting in the birth of daughter cells, as illustrated in Figure 2.1. Detection of mitosis is important because methods for assessing the proliferative activity of stem cells have historically relied on detecting mitosis [107]. In other words, mitosis detection is a critical tool for monitoring the health and growth rate of a cell population. Presently, many cell proliferation assays that are compatible with automated sample handling
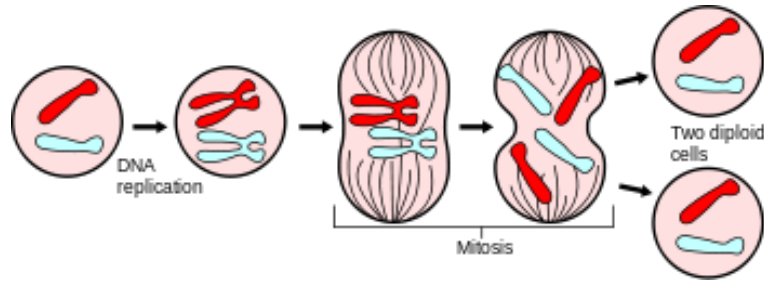
Figure 2.1: Schematic illustrating the process of mitosis[1].

and high-throughput screening have been developed to measure cell proliferation. However, the majority of these procedures utilize fluorescent, luminescent or colorimetric assays which may require destructive methods of cell manipulation, such as cell lysis and *in vitro* staining, and do not allow for continuous monitoring of cells in culture.

2.1.1   Previous Work on Mitosis Detection in Non-fluorescent Microscopy

Several mitosis detection methods for phase-contrast time-lapse microscopy images have been proposed based on cell tracking. Yang *et al.* [131] obtained blob regions along each cell's trajectory produced by a tracking method. Each blob region was then examined to determine if it contained a mitotic event based on several blob properties, including area, perimeter, circularity, and average intensity. Debeir *et al.* [23] adopted a combination of several mean-shift-processes to track cells using an ensemble of nested kernels. One of the kernels was designed to model cells in the mitotic state by taking into account their morphological changes. Al-Kofahi *et al.* [2] presented a multiple-object matching method that can handle cell divisions in the typical frame-by-frame segmentation tracking method. Padfield *et al.* [99] investigated cell cycle phases through tracking each nucleus over time. Mitotic events were then identified by linking non-mitotic phases using both the Euclidean distance metric and the fast marching method. These approaches are intuitive but limited in that mitosis detection is dependent on tracking per-

---

[1]This figure is from Wikipedia, http://en.wikipedia.org/wiki/Mitosis.

formance, which is generally more challenging to achieve than mitosis detection performance itself.

Several mitosis detection algorithms that do not involve cell tracking have recently been proposed. Li *et al.* [73] applied a fast cascade learning framework [125] adopting AdaBoost classifiers [42] to volumetric Haar-like features extracted from spatio-temporal patches covering the whole image region. This approach requires a large number of training samples and searches through the entire space due to the lack of explicit candidate detection. Debeir *et al.* [24] proposed a method to detect mitotic cell regions based on brightness change and link the regions in consecutive frames into a cell division candidate linkage. Each candidate was then validated based on its length (the number of frames). This approach is efficient due to the reduced search space by the candidate detection, but the validation scheme is too simple to effectively distinguish actual mitotic events from the other candidates.

More recently, Liu *et al.* [78] proposed an approach to compensate for the drawbacks of the previous methods. After mitosis candidate patch sequences are constructed through 3D seeded region growing, Hidden Conditional Random Fields (HCRF) [109] are trained to examine each of the candidates. This approach does not resort to tracking and adopts explicit candidate detection as well as model-based validation, achieving good performance on C3H10T1/2 stem cell populations. However, this work does not specify the timing of cell birth and is as such limited in that its mitosis detection results may not be sufficient for accurate quantitative analysis of cell proliferation or cell tracking. In fact, the HCRF model is intrinsically not capable of modeling the timing of cell birth. In addition to inadequate modeling power, this approach is computationally expensive due to the preconditioning step [71], which was originally devised to segment non-mitotic cell regions from background rather than mitotic cell regions.

As cell confluence increases beyond a certain point and thus most of cells are in contact with other cells, mitosis detection becomes far more difficult in extracting mitosis candidates and validating them. No existing approach has been even close to addressing such a task to date.

13
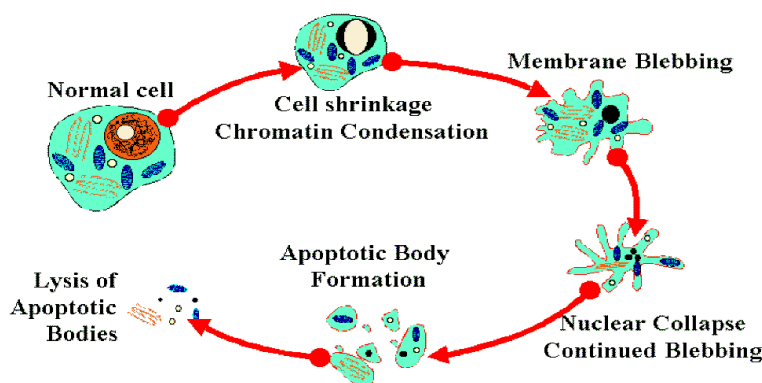
Figure 2.2: Schematic illustrating the process of apoptosis[2].

2.2 Apoptosis and Apoptosis Detection

Apoptosis is programmed cell death, which occurs in an orderly, step-wise manner starting with a series of biochemical events that lead to characteristic changes in the cell prior to its death. [3] The process of apoptosis includes cell shrinking, membrane blebbing, DNA degradation, and the formation of apoptotic bodies that serve to minimize spillage of the internal contents of a dying cell to its surroundings [43], as illustrated in Figure 2.2. The detection of apoptosis, or programmed cell death, is critical for furthering our understanding in biology as apoptosis plays a significant role in both normal tissue development and disease progression, e.g., proper organ development [106], stress-induced neurodegeneration [134], and cancer cell development [40]. In addition, apoptosis detection is often used for toxicity screening of compounds, such as pharmacological reagents [128] and biomaterials [37], as well as drug discovery and subsequent dosage optimization of chemotherapeutic agents [45, 113]. Presently, apoptosis is detected using a variety of assays, which include absorbance measurements and fluorescence or colorimetric

---

[2]This figure is from http://muta-tion.blogspot.com/2011/08/apoptosis.html.

[3]On the other hand, necrosis is uncontrolled cell death, which often occurs as a result of traumatic cell damage owing to tissue injury, lack of an oxygen supply, or chemical insult. In this thesis, we focus on apoptosis since it is more common and of more interest in the community. We use the term "cell death" as the equivalent of "apoptosis".

stains, to measure the levels and activity of apoptotic molecules. These procedures often require a sample to be harvested for each time-point measurement; thus, long-term cell monitoring is not feasible and multiple samples may be required. On the other hand, image analysis of cells using non-destructive imaging such as phase contrast microscopy offers a way to monitor and detect apoptosis in a population of cells over time without adversely affecting cell behavior or requiring additional samples.

2.2.1 Previous Work on Apoptosis Detection in Non-fluorescent Microscopy

There have been little-to-no reports of apoptosis detection in non-fluorescent microscopy. To the best of our knowledge, cell death event detection has only been implicitly performed as a byproduct of cell tracking; i.e., if the trajectory of a cell terminates during cell tracking, the cell is considered dead. However, this simple heuristic often yields poor results because many cell trajectories terminate due to failures in cell tracking as opposed to actual cell death. In addition, this method assumes that cell death occurs at the end of trajectory and thus does not specify the timing of cell deaths. Yet, that is not necessarily true because dead cells that appear morphologically similar to live cells may still be tracked.

2.3 Differentiation and Differentiation Detection

Cell differentiation is the process by which a less specialized cell develops or matures to a more specialized cell type that has more distinct form and function as shown in Figure 2.3. Through this process, a single celled zygote develops into a multicellular organism. Cell differentiation is critical in embryonic development since it allows the organism to generate various types of cells, such as epidermis, muscle, neuron, and blood cells. Differentiation also occurs in adults as adult stem cells generate all cell types of the organ from which they originate during tissue repair and normal cell turnover. Differentiation often involves dramatic changes in size, shape,
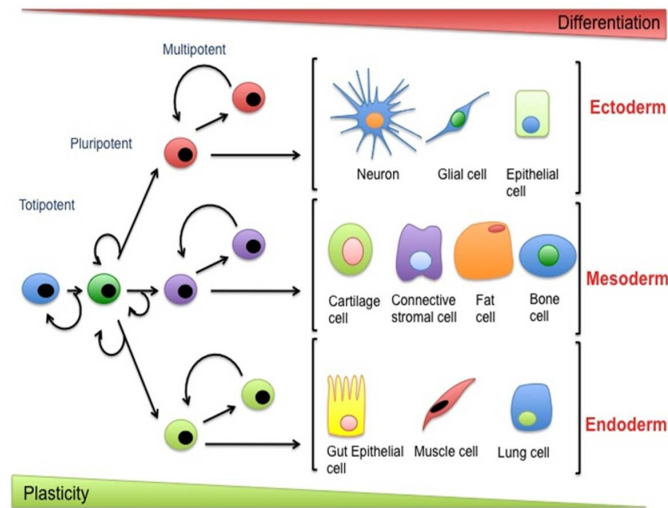
Figure 2.3: Schematic illustrating the process of differentiation[4]. Totipotent cells can give rise to any cells and the potential to create an entire organism. Pluripotent cells can be differentiated into any type cells like totipotent cells, but cannot develop into a fetal or adult organism. Multipotent cells can develop into closely related family of cells, but not any other kind of cell.

and other properties of a cell. Detection of differentiation is important in two folds. First, it helps better understanding on the mechanism of differentiation, which is required to improve the treatment of various disorders associated with a loss of tissue, e.g., bone loss, muscle atrophy, and fat loss. In addition, precise detection of differentiation enables to automate the process of finding the optimal condition to keep stem cells from differentiating and thus losing self-renewal capability, which is critical for stem cell therapy. Presently, differentiation detection relies on time-consuming manual or semi-automated detection that often involves costly reagents such as fixatives, histological stains, antibodies, or fluorescent dyes. Furthermore, for a time-course experiment, multiple number of samples are required to be extracted from various time points because the use of reagents may affect behavior of cells.

---

[4]This figure is from http://www.fastbleep.com/biology-notes/32/158/852.

2.3.1 Previous Work on Differentiation Detection

Automated differentiation detection in non-fluorescent microscopy has been proposed for certain types of cells, mostly for neural stem cells [41, 61, 110], but to the best of our knowledge there is little to no published work for the other types of cells.

2.4 Other Cell Behavior and Cell Tracking

In addition to cells' proliferative activity and fate, we are also interested in other cell behavior, such as cell density, shape, migration direction and speed, and cell cycle length. etc. These cell properties can be analyzed by a cell tracking system, a comprehensive tool for cell behavior analysis that consists of several modules: modules for cell segmentation, cellular event detection, cell tracking, and biological metric computation, etc. Automated systems for visual-tracking of cell populations *in vitro* enable high-throughput analysis of time-lapse microscopy images, whereas manual analysis is often intractable [25, 84, 135]. Of particular interest is cell tracking adopting non-fluorescent microscopy since it enables a long-term monitoring of live and intact cells. Such cell tracking systems can not only provide quantitative analysis of cell behaviors, bu also be useful for the discovery of optimal conditions or quality assurance/control measures of a specific cell behavior of interest.

2.4.1 Previous Work on Cell Tracking

Existing multiple cell tracking methods can be categorized into three methods: filtering-based approach, model-based approach, and detection and association approach.

Kalman filtering [114] or particle filtering [4] and their variations have been popularly used for multiple object tracking in computer vision; their applications include, but not limited to: radar, mobile robot, vehicle, and human motion tracking [26, 95, 127, 129]. In the filtering process, tracking is performed by finding out the most probable current state from the poste-

rior probability distribution computed based on two factors: (1) a predefined model of the expected dynamics between consecutive time frames and (2) (noisy) measurements of the current state [112]. Several variations of particle filtering have been applied to cell tracking. Smal et. al [120] proposed a fully automated particle filtering-based cell tracking method with non-linear and non-Gaussian models by applying sequential Monte Carlo (SMC) methods [34]. Li et al. and Shen et al. also developed cell tracking methods using particle filtering in combination with level-sets [72] and active contours [119], respectively.

Model-based tracking is performed by modeling a target and updating the model in the consecutive frames. Depending on how to model a target, model-based algorithms are mainly grouped into blob tracking, kernel-based tracking or mean-shift tracking [21], contour tracking such as active contours [60], and visual feature matching. Among these algorithms, active contours has been the most popularly used for cell tracking [32, 35, 36, 90, 99]. In this framework, an energy function is defined as a sum of internal and external energies associated to a cell contour in the previous frame, and the function is minimized to find the same cell's contour in the current frame. Other than active contours, Debeir et al. developed a coupled mean-shift algorithm to track migrating cells in phase-contrast microscopy [23].

Another methodology for cell tracking is to first segment and locate cells and then associate them over consecutive frames [47, 84]. Cell segmentation methods employed in cell tracking include intensity thresholding [2], edge detection [50], morphological operations [74], and watershed algorithms [131]. After detecting cell regions, linear programming with multiple hypotheses [2, 74] or min-cost flow [98] was applied to match the cells across frames.

Every approach has its pros and cons depending on many factors including what microscopy is used, how cells look like and behave, and how much human intervention is available. For example, mean-shift cell tracking is effective if cell shape is well characterized and cell movement is not fast, but otherwise the approach may not perform well. Particle filtering-based methods outperform deterministic methods, but they require to define the prior distributions of object

18

states, which are often not obvious for cell tracking. Active contour methods generally handle cell shape deformation well, but often get stuck in local minimum states (there are several strategy to escape from the states, such as simulated annealing [104], at the expense of computation time.). Detection-based association approach is the most efficient, but only effective when cells are accurately detected (cell association over frames can in some degree compensate for the error.).

Chapter 3

Mitosis Detection

In this chapter, we present automated mitosis detection methods in time-lapse phase contrast microscopy. Mitosis detection in phase contrast microscopy enables continuous monitoring of cell growth, which is critical to experimentally assess how altering the conditions under which cells are cultured can impact population growth. In addition, detection of mitosis facilitate the quantification of biological metrics, such as the mitotic index and synchrony, by allowing quality cell lineage construction.

To formulate the problem, we define *birth event* as the time and location at which a mitotic process is completed and the two daughter cells first clearly appear (See Figure 3.1.). A birth event is the most noticeable moment of mitosis and is typically shown as a figure eight shape as the cell membrane splits into two.

In order to know when (in which frame) and where (at which x and y positions) birth events occur, we propose a framework that consists of three steps: detection of candidates, incorporation of temporal information, and validation of the candidates.

1. *Detection of candidates*: The goal of this step is to reduce the search space without missing birth events. Ideally, we should detect all true birth events while containing as few false positives as possible. In practice, we may miss a small number of birth events that are outliers in morphology or brightness.

21
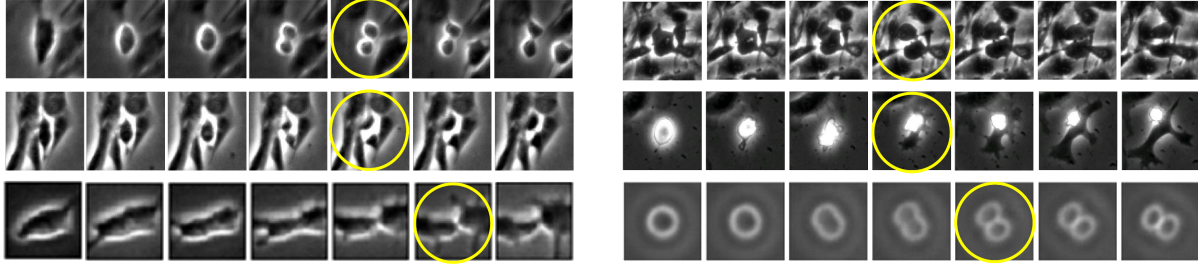
Figure 3.1: Examples of birth events in phase contrast microscopy. Yellow circles enclose birth events, the location and time in which mitosis is completed and daughter cells are born. A birth event is typically shown as a figure eight shape, as the end of the mitotic phase involves cytokinesis, which is the pinching of the cell membrane to split a cell into two; but, sometimes a figure eight shape is not clearly observed.

2. *Incorporation of temporal information*: To accurately determine whether a birth event candidate is indeed a birth event, temporal information needs to be taken into account. By inspecting neighboring frames, confusing cases can be resolved so that both birth event occurrence and timing can be more accurately identified.

3. *Validation of the candidates*: Now the problem reduces to determining whether the birth event candidate in each candidate patch sequence is indeed a birth event. We tackle this problem with temporal probabilistic models developed newly devised for cellular events detection.

The remainder of this chapter is organized as follows. For adherent cell population, we propose a mitosis detection method in Section 3.1 and another advanced mitosis detection method that works under high confluence in Section 3.2. In Section 3.3, we present a mitosis detection method for non-adherent cell populations. We summarize this chapter in Section 3.4.

3.1 Mitosis Detection for Adherent Cells

In this section, we propose a birth event detection method for adherent cell populations in phase contrast microscopy [53]. Since adherent cells that undergo mitosis show changes in morphology and brightness, the method detects candidates based on brightness change and validates the
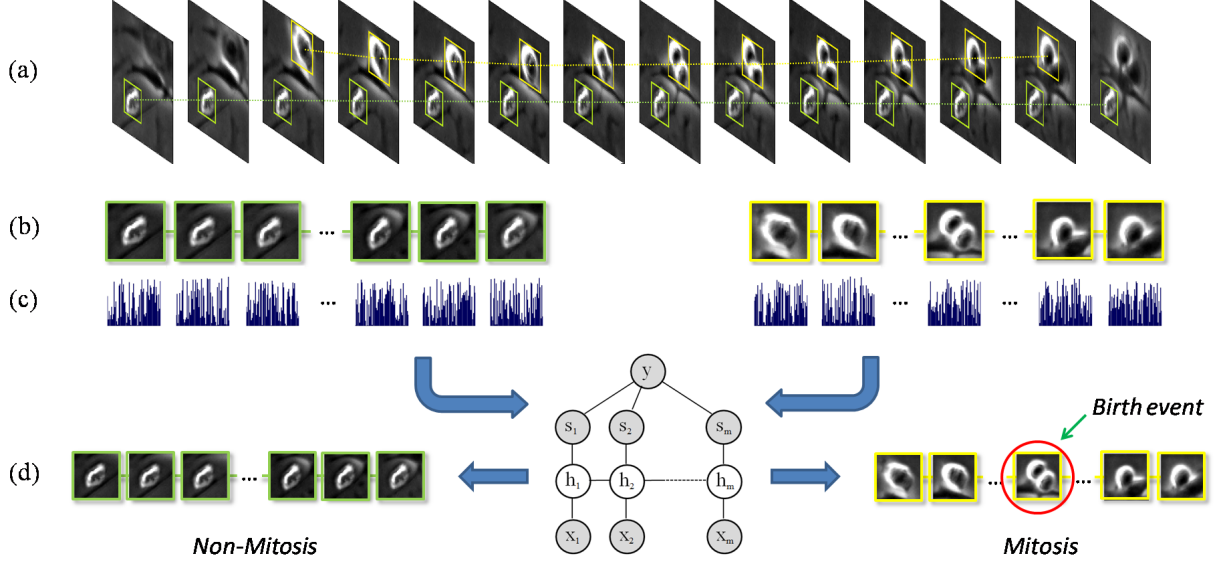
Figure 3.2: Mitosis detection procedure for adherent cells in time-lapse phase contrast microscopy. (a) Candidate patch detection based on brightness and patch sequence extraction over consecutive frames. (b) Examples of candidate patch sequences. (c) Visual features computed for candidate patch sequences. (d) Identification of mitosis occurrence and temporal localization of a birth event using Event Detection Conditional Random Field (EDCRF).

candidates by modeling visual dynamics in mitotic and post-mitotic stages. For candidate validation, we develop a temporal probabilistic model named Event Detection Conditional Random Field (EDCRF) that can jointly model event occurrence and timing. The proposed approach significantly outperforms previous approaches in terms of both detection accuracy and computational efficiency, when applied to multipotent C3H10T1/2 mesenchymal and C2C12 myoblastic stem cell populations. The overall procedure is illustrated in Figure 3.2.

3.1.1 Algorithm

For preprocessing, the average image is computed and subtracted from each image. We present our approach in the three-step framework:

Candidate patch detection: For each image frame, candidate patches are first detected based on brightness, i.e., pixel intensity (Figure 3.2(a)); it is known that the process of mitosis typically exhibits a series of distinctive cell features including increased brightness, increased circularity,

and decreased size [73]. More specifically, each image is convolved with an average filter and the result is thresholded, producing a binary image. For each connected component in the binary image, a bounding box is obtained and bounding boxes that overlap one another are then combined into one bounding box that encloses all the overlapping boxes. From the center point of each bounding box, a candidate patch is extracted.

Candidate patch sequence construction: Candidate patch sequences are constructed by associating spatially overlapping patches in consecutive frames (Figure 3.2(a, b)). For each patch in a candidate patch sequence, we compute Histograms of Oriented Gradient (HOG) features [22] (Figure 3.2(c)) as follows: After dividing each patch into 4×4 subregions, we accumulate gradient magnitudes weighted by a Gaussian function into 4 bins along the orientations at each subregion. After $4 \times 4 \times 4 = 64$ features are computed for each patch, L2 normalization is applied to the feature vectors. To achieve rotation invariance, each training candidate patch sequence is duplicated by rotating or mirroring after rotating all patches in the sequence along several different orientations. This scheme results in performance improvement when training samples are insufficient. In our experiments, we applied three different orientations: $90°$, $180°$, and $270°$. Other rotation schemes are not as effective as this simple duplication scheme because the major axis is not reliably found in phase-contrast microscopy images [80] or the relative spatial information is generally lost [69].

Identification of mitosis occurrence and temporal localization of birth event: After the two previous steps, the problem reduces to determining whether each candidate contains a birth event and which frame the birth event is located in. For these two decision tasks, we propose Event Detection Conditional Random Field (EDCRF), the graphical representation is shown in Figure 3.2(d).

24
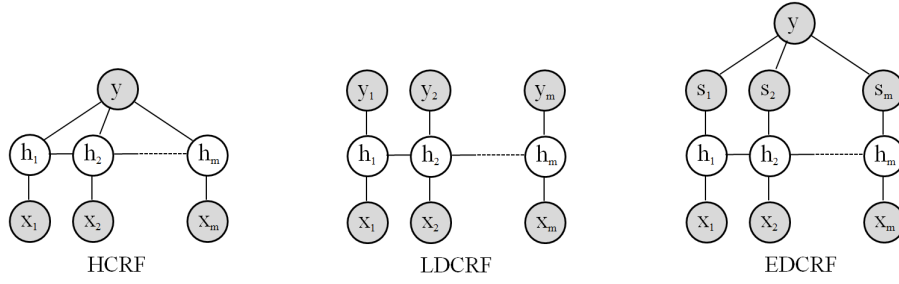
Figure 3.3: Graphical representations of two previous models (HCRF and LDCRF) and our EDCRF model. x_i and h_i represent the i-th observation (the i-th patch in a given candidate sequence in our work) and the hidden state assigned on x_i, respectively. y represents a class label; one class label is assigned on the entire sequence in HCRF, while a class label is assigned for each of observations in LDCRF. In EDCRF, y is the label indicating the timing of the birth event and s_i is the i-th sub-label determined by y. Gray circles denote observed variables for training. For testing, y and s are not observed.

3.1.2 Event Detection Conditional Random Field

Before introducing EDCRF, we review two previous probabilistic models: Hidden Conditional Random Fields (HCRF) [109] and Latent-Dynamic Conditional Random Fields (LDCRF) [89]. The graphical representations of these two models are shown in Figure 3.3.

HCRF was devised to analyze temporal sequences, such as vision and speech applications [46, 108]. Particularly, it has been applied to gesture recognition tasks and demonstrates its superiority to Hidden Markov Models (HMM) and Conditional Random Fields (CRF) [126]. HCRF also excels in mitosis occurrence detection [78]. However, since HCRF handles sequences on each of which only one label is imposed, it cannot capture the timing of particular events, such as birth events, in candidate patch sequences.

LDCRF was proposed to additionally capture extrinsic class dynamics based on the idea of HCRF [89]. Hidden variables in LDCRF not only model sub-structure of a class sequence, but also learn dynamics between class labels; thus, the model can be directly applied to unsegmented sequences. Efficient training and inference schemes can be achieved by constraining each class label to have a disjoint set of associated hidden states. LDCRF has the potential to be modified

into a model for event detection in that an event can be expressed as a class dynamic change when different labels are assigned on observations before and after the event.

The main idea of EDCRF is as follows: if an event occurs, visual changes before and after the event are separately modeled; otherwise, the entire visual transition is modeled together. This strategy is useful when an event shows a totally different pattern of visual change before and after the event when an event occurs. In our problem, before a birth event, a mitotic cell becomes bright and shrunken, while after the event, two newborn cells become dark and stretched. Therefore, by separately modeling mitotic and post-mitotic stages, not only is the visual change over time more precisely modeled during cell division, but also the timing of a birth event is explicitly modeled.

The formulation of EDCRF is as follows. Suppose that n candidate patch sequence and label pairs $\{(\mathbf{x_1}, y_1), (\mathbf{x_2}, y_2), \cdots, (\mathbf{x_n}, y_n)\}$ are given. Each label y_i is defined as

$$
y_i = \begin{cases} p & \text{if the } p\text{-th patch of } \mathbf{x_i} \text{ contains a birth event} \\ \\ 0 & \text{if there exists no birth event in } \mathbf{x_i} \end{cases} \tag{3.1}
$$

Each sequence $\mathbf{x} = (x_1, x_2, \cdots, x_m)$ consists of m candidate patches where x_j denotes the j-th patch (m can be varied for different sequences.). We assume hidden variables $\mathbf{h} = (h_1, h_2, \cdots, h_m)$ and sub-labels $\mathbf{s} = (s_1, s_2, \cdots, s_m)$ where h_j and s_j correspond to x_j. When a sequence label y is given, the sub-labels $s_1, s_2, \cdots,$ and s_m are defined as

$$
s_j = \begin{cases} N & \text{if } y = 0 \\ \\ B & \text{if } y > 0 \text{ and } j < y \\ \\ A & \text{if } y > 0 \text{ and } j \geq y \end{cases} \tag{3.2}
$$

where label N, B, and A represent *No event*, *Before the event*, and *After the event (including the event)*, respectively. In other words, if there exists a birth event in a given candidate sequence, the sub-labels before the event are set to be B and the other sub-labels set to be A. Otherwise,

26

all the sub-labels are set to be N.

Under these definitions, we define a latent conditional model for each sequence:

$$P(y|\mathbf{x}, \theta) = P(\mathbf{s}|\mathbf{x}, \theta) = \sum_{\mathbf{h}} P(\mathbf{s}|\mathbf{h}, \mathbf{x}, \theta) P(\mathbf{h}|\mathbf{x}, \theta) \tag{3.3}$$

where θ is a set of parameters of the model.

In order to make the modeling efficient, we adopt the same scheme as Latent-Dynamic Conditional Random Fields (LDCRF) [89], which restricts that each sub-class label s is associated only with hidden states in a disjoint set $\mathcal{H}_s$. Then

$$P(\mathbf{s}|\mathbf{h}, \mathbf{x}, \theta) = \begin{cases} 1 & \text{if } \forall h_j \in \mathcal{H}_{s_j} \\ 0 & \text{otherwise} \end{cases} \tag{3.4}$$

The proposed model is thus simplified as

$$P(y|\mathbf{x}, \theta) = \sum_{\mathbf{h}: \forall h_j \in \mathcal{H}_{s_j}} P(\mathbf{h}|\mathbf{x}, \theta) \tag{3.5}$$

We define $P(\mathbf{h}|\mathbf{x}, \theta)$ using the typical conditional random field (CRF) formulation.

$$P(\mathbf{h}|\mathbf{x}, \theta) = \frac{1}{Z} exp\Big(\sum_{j=1}^{m} f^{(s)}(h_j, \mathbf{x}, j) \cdot \theta^{(s)}(h_j) + \sum_{j=2}^{m} f^{(t)}(h_{j-1}, h_j, \mathbf{x}, j) \cdot \theta^{(t)}(h_{j-1}, h_j) \Big) \tag{3.6}$$

where Z is a partition function. $f^{(s)}(h_j, \mathbf{x}, j)$ and $f^{(t)}(h_{j-1}, h_j, \mathbf{x}, j)$ are a state and a transition function, respectively. $\theta^{(s)}$ and $\theta^{(t)}$ are the parameters of state and transition functions, respectively. Also, $\theta = \{\theta^{(s)}, \theta^{(t)}\}$.

We define state functions as

$$f^{(s)}(h_j, \mathbf{x}, j) = \phi(x_j) \tag{3.7}$$

27

where $\phi(x_j)$ is a visual feature vector of x_j. The inner product of $\phi(x_j) \cdot \theta^{(s)}(h_j)$ can be interpreted as a compatibility measure between observation x_j and hidden state h_j [109]. We define transition functions as

$$f^{(t)}(h_{j-1}, h_j, \mathbf{x}, j) = \begin{cases} 1 & \text{if } (h_j - 1, h_j) \in \mathcal{U} \\ 0 & \text{otherwise} \end{cases} \tag{3.8}$$

where $\mathcal{U} = \mathcal{H}_N \times \mathcal{H}_N \cup \mathcal{H}_B \times \mathcal{H}_B \cup \mathcal{H}_B \times \mathcal{H}_A \cup \mathcal{H}_A \times \mathcal{H}_A$. We restrict sub-level transitions among (N, N), (B, B), (B, A), and (A, A), which respectively represent *no event*, *before the event*, *during the event*, and *after the event*. Aside from these four transitions, there exists no other transition in our setting.

For learning parameters, we maximize the following regularized log-likelihood function as conventionally [66, 67].

$$L(\theta) = \sum_{i=1}^{n} \log P(y_i | \mathbf{x_i}, \theta) - \frac{1}{2\sigma^2} ||\theta||^2 \tag{3.9}$$

where σ is the variance of a Gaussian prior. This optimization problem can be solved by gradient ascent methods and belief propagation [102].

For testing of a new sequence $\mathbf{x}$, we first compute the probabilities of our conditional model with all possible y and the optimal parameter θ^* obtained in the training step.

$P(y = 0 | \mathbf{x}, \theta^*)$ can be computed as

$$P(y = 0 | \mathbf{x}, \theta^*) = P(s_1 = N, \cdots, s_m = N | \mathbf{x}, \theta^*) = P(s_1 = N | \mathbf{x}, \theta^*) = \sum_{h_1 \in H_N} P(h_1 | \mathbf{x}, \theta^*) \tag{3.10}$$

because $s_1 = N$ leads to $s_2, \cdots, s_m = N$ under our restricted transition rule. Similarly,

$$P(y = 1 | \mathbf{x}, \theta^*) = P(s_1 = A, \cdots, s_m = A | \mathbf{x}, \theta^*) = P(s_1 = A | \mathbf{x}, \theta^*) = \sum_{h_1 \in H_A} P(h_1 | \mathbf{x}, \theta^*) \tag{3.11}$$

The other conditional probabilities can be computed as

$$P(y = j|\mathbf{x}, \theta^*) = P(s_1 = B, \cdots, s_{j-1} = B, s_j = A, \cdots, s_m = A|\mathbf{x}, \theta^*) \qquad (3.12)$$

$$= P(s_{j-1} = B, s_j = A|\mathbf{x}, \theta^*) = P(s_{j-1} = B|\mathbf{x}, \theta^*) - P(s_{j-1} = B, s_j = B|\mathbf{x}, \theta^*)$$

$$= P(s_{j-1} = B|\mathbf{x}, \theta^*) - P(s_j = B|\mathbf{x}, \theta^*) = \sum_{h_{j-1} \in H_B} P(h_{j-1}|\mathbf{x}, \theta^*) - \sum_{h_j \in H_B} P(h_j|\mathbf{x}, \theta^*)$$

for $j = 2, ..., m$.

For mitosis occurrence decision on each candidate sequence, we compare $P(y = 0|\mathbf{x}, \theta^*)$ and $1 - P(y = 0|\mathbf{x}, \theta^*)$. If the former is greater, EDCRF determines that there is no mitotic event in the given sequence. Otherwise, the temporal localization of the birth event follows by comparing $P(y = 1|\mathbf{x}, \theta^*), \cdots,$ and $P(y = m|\mathbf{x}, \theta^*)$. More formally,

$$y^* = \begin{cases} 0 & \text{if } P(y = 0|\mathbf{x}, \theta^*) > 0.5 \\ \arg\max_{y=1,\cdots,m} P(y|\mathbf{x}, \theta^*) & \text{otherwise} \end{cases} \qquad (3.13)$$

3.1.3 Experiments

Data and ground truth: Multipotent C3H10T1/2 mesenchymal stem cells (ATTC, Manassas, VA) serve as a model for the adult human mesenchymal stem cell and were grown in Dulbecco's Modified Eagle's Media (DMEM; Invitrogen, Carlsbad, CA), 10% fetal bovine serum (Invitrogen, Carlsbad, CA) and 1% penicillin-streptomycin (PS; Invitrogen, Carlsbad, CA). C2C12 myoblastic stem cells (ATTC, Manassas, VA) have the capacity to differentiate into osteoblasts and myocytes and were grown in DMEM, 10% bovine serum (Invitrogen, Carlsbad, CA) and 1% PS. All cells were kept at 37°C, 5% CO_2 in a humidified incubator.

Phase contrast microscopy images of the two types of stem cell populations (C3H10T1/2 and C2C12) were generated as follows. During the growth of stem cells, microscopy cell images were acquired every 5min using a Zeiss Axiovert T135V microscope (Carl Zeiss Microimaging,

Thornwood, NY) equipped with a 5X, 0.15 N.A. phase contrast objective, a custom-stage incubator, and the InVitro software (Media Cybernetics Inc., Bethesda, MD). Each of the images contains 1392×1040 pixels with a resolution of 1.3μm/pixel. C3H10T1/2 and C2C12 microscopy image sequences consist of 1436 and 1013 images, respectively.

After acquiring the image sequences, manual annotation of birth events was performed on one C2C12 and five C3H10T1/2 image sequences. For each birth event, the center of the boundary between two daughter cells was marked when the boundary is clearly observed. Since C2C12 myoblasts were cultured to a much higher level of confluence than C3H10T1/2 mesenchymal stem cells in our data, each of the C3H10T1/2 sequences contain 41 to 128 mitotic events, while the C2C12 sequence contains 673 mitotic events.

Experiments: For mitosis detection without considering the timing of birth events, we compare EDCRF with HCRF [109], which was previously used for mitosis occurrence detection. HCRF is known to outperform Hidden Markov Models (HMM) and Conditional Random Fields (CRF) [78, 126].

To the best of our knowledge, there exists no probabilistic model which has been used for automated temporal localization of birth events given candidate patch sequences; in this respect, our EDCRF model is original. In order to compare EDCRF with possible alternatives, we additionally use either Support Vector Machines (SVM) or Conditional Random Fields (CRF) for the temporal localization of the birth event after the identification of mitosis occurrence using HCRF. In these alternative approaches, the identification of mitosis occurrence and the temporal localization of birth event are sequentially performed.

In the model incorporating HCRF and SVM (HCRF+SVM), a version of SVM that outputs probabilities is applied to the sequences determined by HCRF to have a mitosis occurrence. More specifically, for training, candidate patches containing manual annotation of birth events are used as positive samples and all patches in the candidate patch sequences that do not contain mitosis as negative samples. For testing, the SVM produces the probabilities that each patch contains a

birth event; the patch with the highest probability in the sequence is then decided to contain a birth event.

In the model combining HCRF and CRF (HCRF+CRF), the same labeling scheme as EDCRF is applied to temporally localize birth events. More specifically, for training, one label is assigned to the label variables before the birth event and another label is assigned after the event. If there exists no birth event, a third label is assigned to all the label variables. For testing, the same inference scheme as the EDCRF model is utilized to determine a birth event's temporal location.

For C3H10T1/2 image data, one sequence is used for training and the other four sequences for testing whereas for C2C12 image data, half of all mitotic cells are used for training in turn, and the other half are used for testing.

Evaluation: After constructing candidate patch sequences, the number of undetected mitosis is counted. Each mitotic event, specifically the birth event, is expected to be captured by one of the candidate patch sequences. However, if there are birth events which are not contained in any candidate patch sequence, such cases are considered undetected. If one candidate patch sequence contains more than one birth event, all of the birth events except the first one are considered undetected as well. All of the undetected mitosis are counted as false negatives when precision and recall are computed.

After applying the probabilistic models, we first evaluated the identification of mitosis occurrence in terms of precision and recall without examining the timing of birth events. In this case, true positive is defined as the case that a candidate patch sequence containing a birth event is correctly identified no matter how great the timing error of the birth event is. If one birth event is located in more than one candidate patches, the birth event is considered to exclusively belong to the patch whose center is the closest to the birth event among the candidate patches.

We then evaluate the identification of mitosis occurrence with the constraint of birth event timing. In this case, among the aforementioned true positive cases, only the cases in which the timing error of the birth event is not greater than a certain threshold are considered true posi-

	C3H10T1/2				C2C12			
Model	Precision	Recall	F-measure	AUC	Precision	Recall	F-measure	AUC
EDCRF	0.913±0.040	0.870±0.048	0.889±0.007	0.958±0.006	0.950	0.893	0.921	0.930
HCRF	0.890±0.019	0.863±0.033	0.876±0.010	0.952±0.005	0.924	0.875	0.899	0.866

Table 3.1: Comparison of mitosis detection performance between EDCRF and HCRF models when the timing of birth events is not considered. The comparison is conducted in terms of precision, recall, F-measure, and the AUC of the PR-curve on four C3H10T1/2 and one C2C12 stem cell populations. EDCRF outperforms HCRF in all cases.
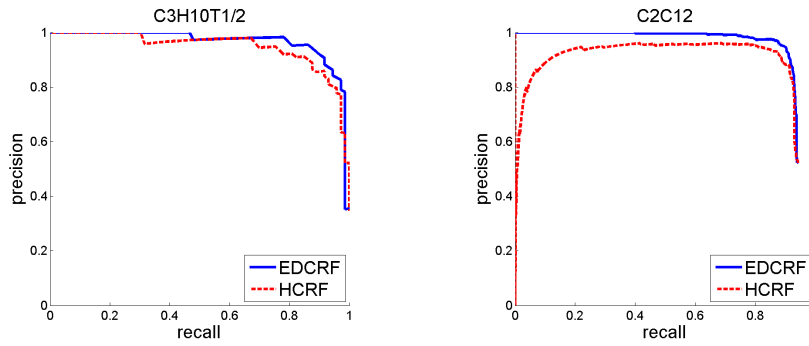
Figure 3.4: The PR-curves of mitosis detection on the first C3H10T1/2 and the C2C12 image sequences when the timing of birth events is not considered. In terms of AUC, EDCRF outperforms HCRF in both cell types.

tive. In other words, although a candidate sequence including an actual birth event is correctly identified, if the timing error of the birth event is greater than the threshold, the birth event is considered undetected as well as the detection is regarded false. More specifically, the timing error is measured as the frame difference between the patch containing the ground truth and the patch containing the detected birth event in the sequence. We use four different thresholds (1, 3, 5, and 10) and report precision and recall for each case. The smaller a threshold is, the stricter the evaluation is. To compare the detection results, we also compute F-measure, which is the harmonic mean of precision and recall, and the area under the curve (AUC) of the precision-recall curve (PR-curve). PR-curves are obtained by varying the decision probability in Eq. 3.13.

3.1.4 Results and Discussions

During candidate patch sequence extraction, one birth event is not captured in four C3H10T1/2 sequences which are used for testing. There is no case that one candidate patch sequence contains more than one birth event in the C3H10T1/2 sequences. In the case of the C2C12 sequence, one birth event is missed and 36 birth events are detected following another birth event in the same sequence; as a result, a total of 37 false negative cases are reported before the decision tasks. Multiple mitosis in a candidate patch sequence occur due to the adhesion of mitotic cells at high confluence present in the C2C12 sequence. Under such circumstances, it is difficult to identify attached cells as separate entities.

As shown in Table 3.1, the proposed mitosis detection method achieves 0.913/0.870 and 0.950/0.893 in terms of precision/recall on C3H10T1/2 and C2C12 stem cell populations, respectively, when only mitosis occurrence is considered. In terms of F-measure and AUC, the accuracy on C2C12 is comparable to that of C3H10T1/2, although the C2C12 cell population is more challenging due to its higher level of confluence and deformability. Having more training samples for C2C12 might be the reason.

Compared with the HCRF model, the EDCRF model is superior in mitosis occurrence detection in terms of precision, recall, F-measure, and the AUC of the PR-curve as shown in Table 3.1 and Figure 3.4. A Student's paired t-test on the F-measures shows that the performance improvement is statistically significant at the significance level 0.01 (p=0.0008). These results indicate that the information of birth event timing is actually helpful for identifying the occurrence of mitosis. HCRF cannot utilize such additional information due to its limited expression power. On the other hand, EDCRF simultaneously models both mitosis occurrence and birth event timing, resulting in higher discriminating power than HCRF in mitosis occurrence identification.

When we additionally consider the timing errors of birth events and threshold them to obtain true positive cases, the superiority of EDCRF is more obvious. Compared to the alternative models, HCRF+SVM and HCRF+CRF, EDCRF consistently outperforms them in terms of precision,

recall, F-measure, and AUC regardless of the cell type and the threshold for the timing error of birth events as shown in Table 3.2. Student's paired t-tests on the F-measures show that the performance improvements are statistically significant at the significance level 0.01 regardless of the threshold of the timing error (EDCRF *vs.* HCRF+SVM: p=0.0024, 0.0038, 0.0092, and 0.0028; EDCRF *vs.* HCRF+CRF: p=0.0001, 0.0013, 0.0055, and 0.0037 for the threshold=1, 3, 5, and 10, respectively). When a smaller threshold corresponding to a stricter evaluation of temporal localization is applied, our approach significantly outperforms the alternative approaches as seen in Figure 3.5. In the alternative models, the identification of mitosis occurrence and the temporal localization of birth events are separately performed so the localization step may not be meaningful if mitosis occurrence is incorrectly identified. In this sense, the preceding mitosis occurrence decision may undermine the full potential of the localization step that follows. It is worth mentioning that recalls do not reach one in the PR-curves because some of existing mitosis are not detected regardless of the decision probability of mitosis occurrence. The undetected mitosis occur due to either imperfect extraction of candidate patch sequences or inaccurate temporal localization of birth events.

Figure 3.6 shows the distribution of the frame differences between the human and computer annotations of birth events among true positive samples on C3H10T1/2 and C2C12 sequences when at most 10 frame difference is allowed in temporal localization of birth events. The averages of the (absolute) frame differences using EDCRF are smaller than using the alternative models as shown in Table 3.3. EDCRF achieves statistically significant improvements in the temporal localization of birth events; when applying Student's t-tests, we obtain p-values less than 0.001 for all of the four cases: comparison with HCRF+SVM on C3H10T1/2 (p=0.0006), HCRF+CRF on C3H10T1/2 (p<0.0001), HCRF+SVM on C2C12 (p<0.0001), and HCRF+CRF on C2C12 (p<0.0001). In addition to the lesser performance of HCRF in the identification of mitosis occurrence, SVM and CRF also fall short of the capability of EDCRF in the temporal localization of birth events. SVM is not capable of modeling temporal dynamic and CRF does

	EDCRF							
	C3H10T1/2				C2C12			
th	Precision	Recall	F-measure	AUC	Precision	Recall	F-measure	AUC
1	0.740±0.067	0.703±0.035	0.720±0.041	0.660±0.047	0.880	0.828	0.853	0.819
3	0.863±0.044	0.822±0.043	0.840±0.015	0.882±0.026	0.925	0.870	0.897	0.895
5	0.899±0.037	0.857±0.052	0.876±0.014	0.934±0.017	0.940	0.884	0.911	0.913
10	0.910±0.042	0.867±0.047	0.886±0.009	0.952±0.013	0.947	0.890	0.918	0.923
	HCRF + SVM							
	C3H10T1/2				C2C12			
th	Precision	Recall	F-measure	AUC	Precision	Recall	F-measure	AUC
1	0.604±0.052	0.585±0.051	0.594±0.049	0.466±0.055	0.550	0.520	0.535	0.270
3	0.795±0.045	0.773±0.064	0.783±0.052	0.785±0.090	0.765	0.724	0.744	0.552
5	0.872±0.010	0.847±0.043	0.859±0.019	0.920±0.022	0.873	0.826	0.849	0.745
10	0.887±0.019	0.860±0.033	0.873±0.010	0.946±0.007	0.909	0.861	0.884	0.828
	HCRF + CRF							
	C3H10T1/2				C2C12			
th	Precision	Recall	F-measure	AUC	Precision	Recall	F-measure	AUC
1	0.583±0.044	0.565±0.036	0.574±0.037	0.463±0.031	0.687	0.650	0.668	0.473
3	0.771±0.055	0.749±0.071	0.759±0.060	0.744±0.099	0.788	0.746	0.767	0.612
5	0.853±0.036	0.827±0.039	0.839±0.028	0.890±0.043	0.838	0.793	0.815	0.685
10	0.884±0.020	0.857±0.034	0.870±0.012	0.943±0.018	0.892	0.845	0.868	0.787

Table 3.2: The mitosis detection performance comparison when the timing of birth events is examined in addition to mitosis occurrence. Our approach is compared with the alternative approaches based on HCRF (HCRF+SVM and HCRF+CRF) in terms of precision, recall, F-measure, and the AUC of the PR-curve on C3H10T1/2 and C2C12 stem cell populations. Detection results are considered true positive when the timing error of the birth event is not greater than a given threshold (one of 1, 3, 5, and 10). When a threshold is small (the evaluation is strict), our approach more clearly outperforms the alternatives. (*th*: threshold of frame difference)

not capture the hidden state structures in candidate patch sequences.

Using our design, the overall process of mitosis detection is more computationally efficient
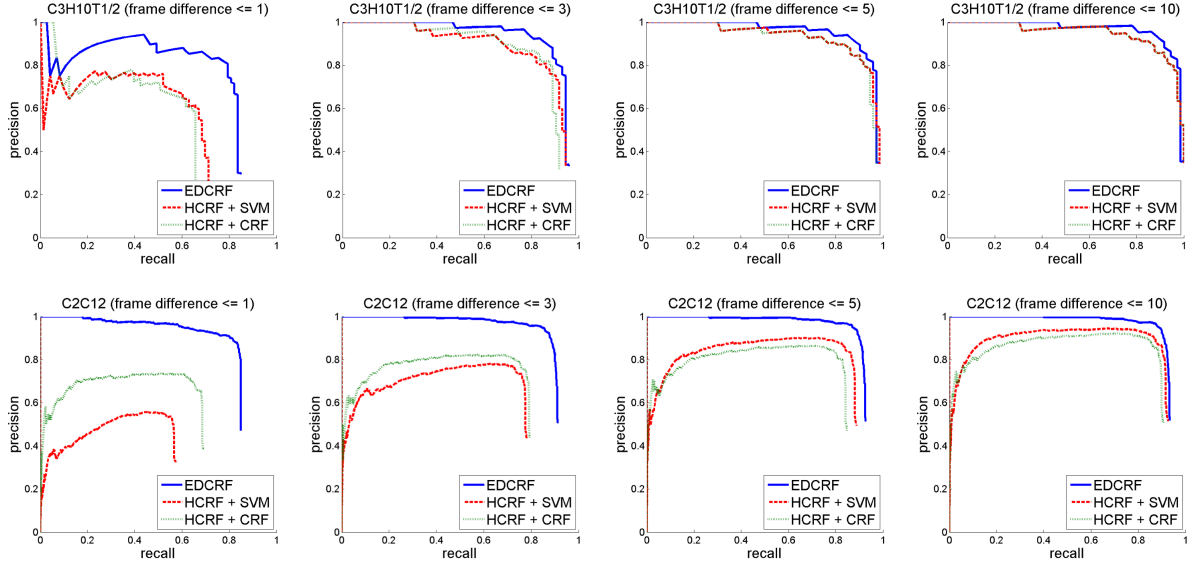
Figure 3.5: The PR-curves of mitosis detection with EDCRF and two alternative models (HCRF+SVM and HCRF+CRF) on the first C3H10T1/2 (top) and the C2C12 (bottom) image sequences. A detection is considered true positive when the timing error is not greater than a given threshold (one of 1, 3, 5, and 10). The superiority of our approach is more evident when the threshold is small, *i.e.*, the evaluation on birth event timing is strict.
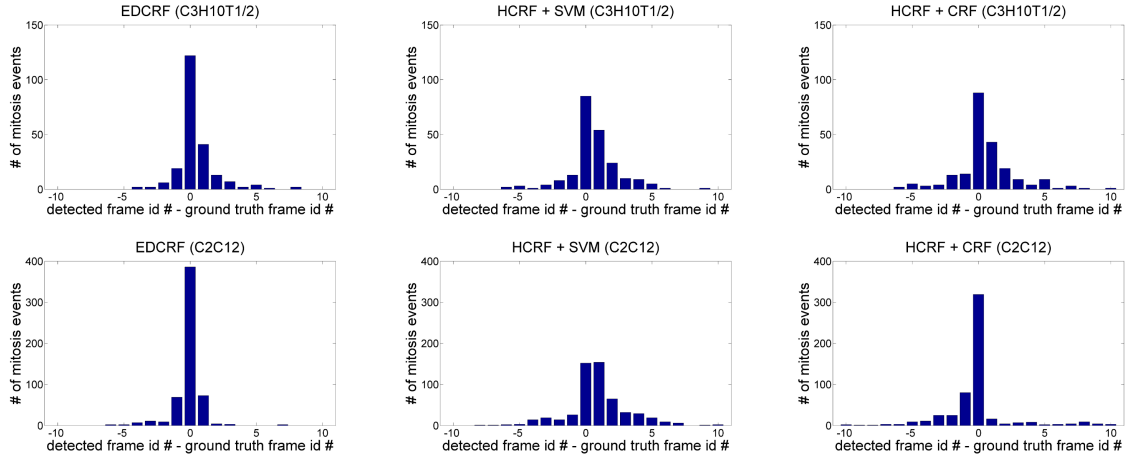
Figure 3.6: Temporal localization precision of birth events of three approaches: EDCRF (left), HCRF+SVM (middle), and HCRF+CRF (right) on two cell populations: C3H10T1/2 (top) and C2C12 (bottom). The histograms show the frequency distribution of birth event timing errors when at most 10 frame error is allowed. Timing error is measured as the frame difference between the patches containing the ground truth and the detected result of the birth event among true positive samples. The temporal localization of EDCRF is more accurate than the alternatives.

36

Cell type	EDCRF	HCRF+SVM	HCRF+CRF
C3H10T1/2	0.828±1.334	1.273±1.528	1.438±1.826
C2C12	0.482±0.957	1.685±1.769	1.189±2.120

Table 3.3: The average and standard deviation of the timing error of birth events in terms of (absolute) frame difference. The error of EDCRF is smaller than the alternative models and the improvement is statistically significant.

Frame 674   Frame 676   Frame 678   Frame 680   Frame 682   Frame 684
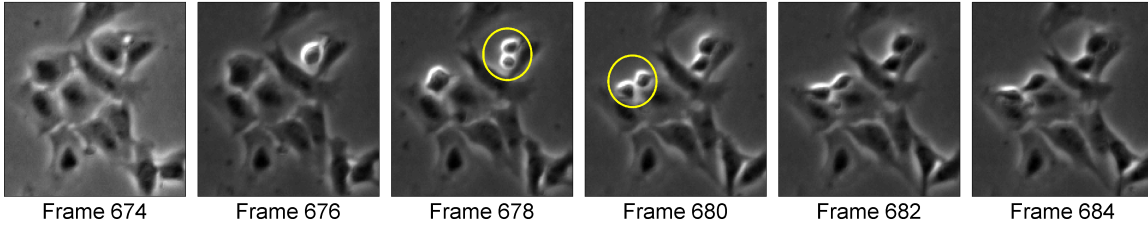
Figure 3.7: Sample images illustrating examples of mitosis detection on the C2C12 microscopy image sequence. Each of the yellow circles in frames 678 and 680 surrounds a detected birth event. The EDCRF model temporally localizes birth events when there is a distinct boundary between daughter cells.

compared to the previous work [78]. By removing the time-consuming preconditioning [71], our approach can process a test image of 1392×1040 pixels in less than 5 seconds, while the previous method spends more than 5 minutes on the preconditioning step alone when using a computer with a dual core 2GHz processor and 2GB memory. This computational improvement enables real-time analysis of microscopy images periodically taken even with a short time interval. The previously used preconditioning scheme [71] is not required because cells show distinctive characteristics during mitosis. Mitotic cells can be recognized without applying the complex method devised for non-mitotic cells rather than mitotic cells.

Figure 3.7 demonstrates two examples of birth events in the C2C12 myoblastic stem cell population automatically detected by our approach. Our approach shows good performance on the C2C12 stem population with higher confluence (approximately 80∼90%) as shown in Figure 3.8.
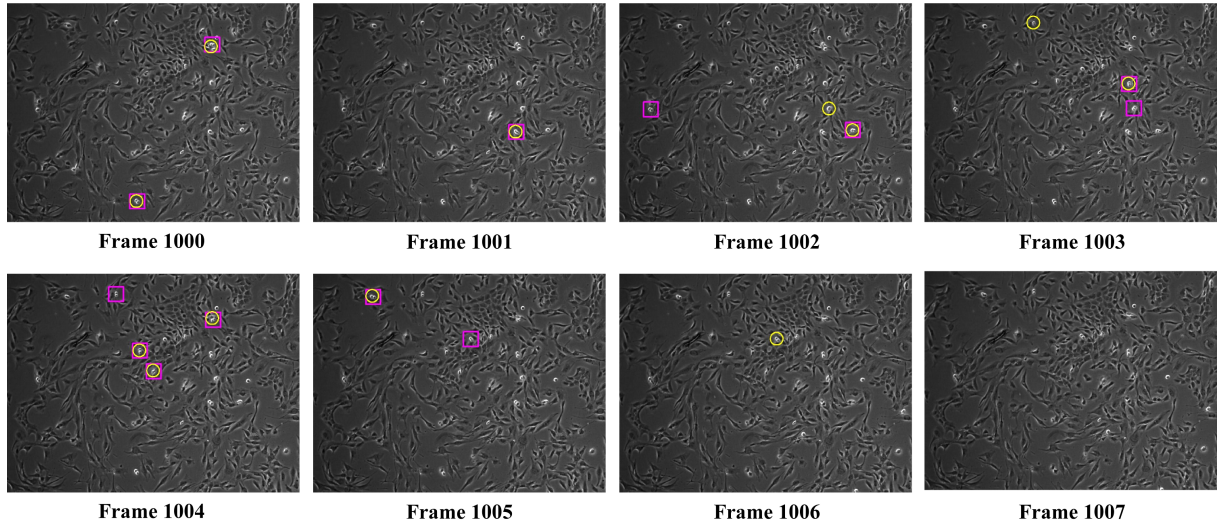
Figure 3.8: Sample images illustrating examples of mitosis detection on the C2C12 microscopy image sequence from frames 1000 through 1007. Each of the yellow circles surrounds a detected birth event produced by our approach, whereas each of magenta squares encloses a ground truth birth event annotated by a human. During these eight frames, twelve birth events are correctly detected within one frame error and one birth event is missed in frame 1002.
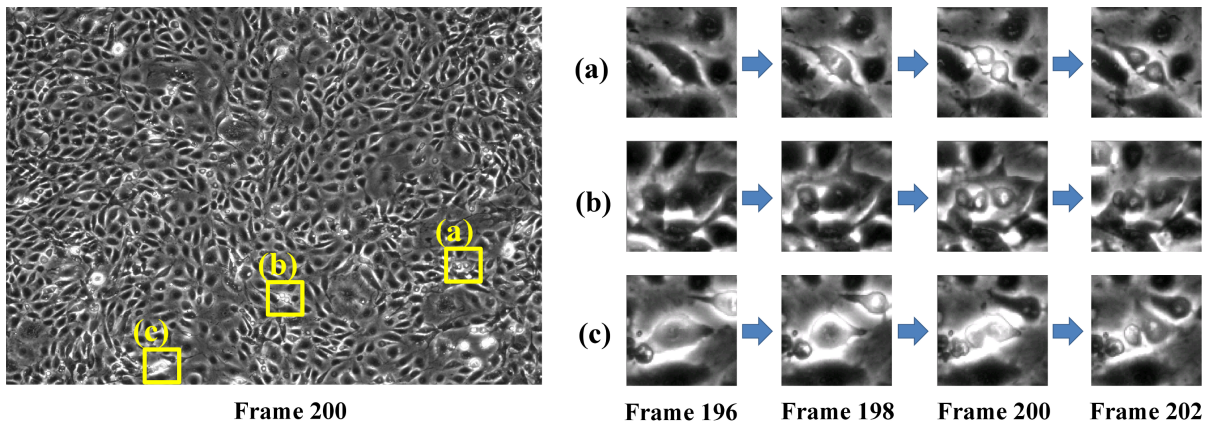
Figure 3.9: Example of a phase contrast microscopy image with high cell confluence, or cell density (top), and three examples of mitosis (bottom). During cell division, mitotic (mother) and newborn (daughter) cells typically demonstrate increased brightness and circularity as well as decreased size. At the dividing moment, frame 200 in these examples, a bright figure eight shape is expected to be observed; but, such a shape is often not clear.

| Frame *t* | Frame *t*-3 | Frame *t*-2 | Frame *t*-1 | Frame *t* | Frame *t*+1 | Frame *t*+2 | Frame *t*+3 |
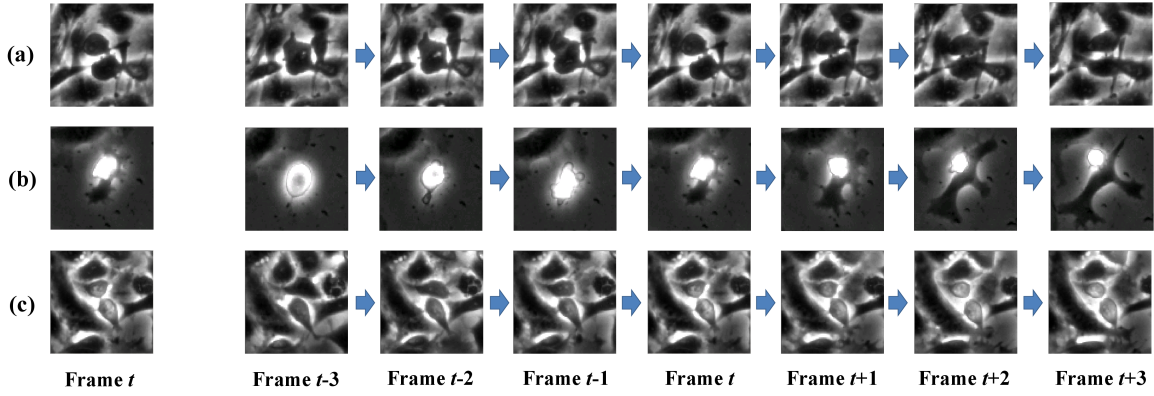
Figure 3.10: Confusing birth and non-birth event examples. When only one patch in frame t is observed (left), (a) and (b) do not seem to show a birth event, but (c) does. Investigating the neighboring frames (right), however, leads to the opposite conclusion. (a) In contrast to typical mitosis of adherent cells, mother and daughter cells do not appear bright; such a birth event is often missed even by human. (b) After a birth event, one daughter cell stretches out and becomes dark while the other daughter cell remains bright and circular. (c) Two cells that are brighter than typical cells are in contact with each other, forming a bright figure eight shape in frame t.

3.2   Mitosis Detection under High Cell Confluence

In this section, we propose a birth event detection method for adherent cell populations in phase contrast microscopy under high cell confluence [51]. The difficulty of birth event detection in time-lapse phase contrast microscopy of high cell confluence is twofold. First, the search space for birth event detection is huge because birth events simultaneously occur at various locations among numerous cells in time-lapse microscopy. (See Figure 3.9.) Since hundreds of deformable cells are moving and bright halos appear and disappear among the cells, regions of interest should be carefully selected. Second, visual properties of birth events are not uniform but vary in shape and appearance since they are determined by the external stimuli from neighboring cells as well as the internal state of the mitotic cells. In addition, non-mitotic cells often appear bright and circular, looking like mitotic or newborn cells. Figure 3.10 shows examples of confusing birth and non-birth events. For resolving the confusion, the change of cell visual properties over time must be taken into account.

We propose a birth event detection method that addresses these difficulties. We first reduce the search space by locating image patches that express visual properties of birth events. For this birth event candidate detection, a cascaded filtering strategy is presented. Each candidate is extended to a candidate patch sequence by incorporating patches in the neighboring frames that precede and follow the potential birth event. The patch sequence is then examined to determine whether the birth event candidate is indeed a birth event. For this decision, we develop a probabilistic model named Two-Labeled Hidden Conditional Random Field (TL-HCRF) that can model the most probable timing of a birth event as well as the visual change of the candidate mitotic (mother) and newborn (daughter) cells over time. We tested the proposed method on five time-lapse phase contrast microscopy image sequences containing more than 1000 birth events in total. The performance of our method on birth event detection is significantly superior to that of previous methods. Our test data contain two types of cells under different culture conditions that cause different cell behavior and appearance, demonstrating the robustness of the proposed method.

3.2.1 Algorithm

We propose a method that detects birth events in time-lapse phase contrast microscopy of a highly dense cell population. The method finds when (in which frame) and where (at which x and y positions) birth events occur through three steps: detection of birth event candidates, incorporation of temporal information, and validation of the candidates. The overall approach is summarized in Figure 3.11.

Detection of Birth Event Candidates: To detect birth event candidates, we examine all image patches with different orientations in a given microscopy image to determine where and with which orientation potential birth events are placed in the image. To facilitate this process, we present a cascaded filtering scheme that is designed to first remove easily recognizable non-birth events using a simple model, and then more difficult cases with more complex models.
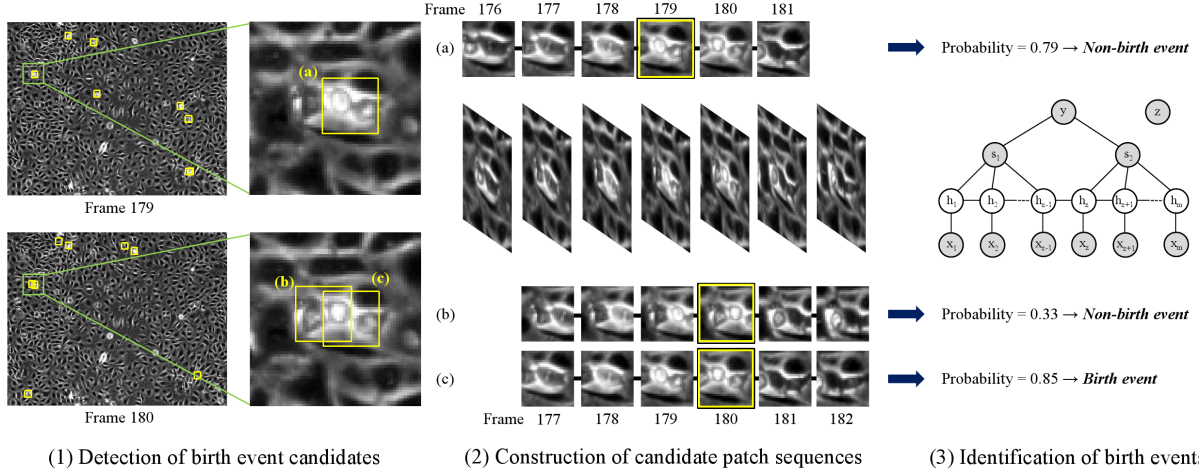
Figure 3.11: Overall approach. (1) Candidates of birth events are detected in each frame of a time-lapse phase contrast microscopy image sequence. In the figure, each yellow square encloses a birth event candidate. (2) Each birth event candidate is expanded into a candidate patch sequence by tracking it in the neighboring frames. The figure shows three examples of candidate patch sequences ((a)-(c)). (3) Each candidate patch sequence is examined to determine whether the birth event candidate located in it is indeed a birth event. For this examination, a probabilistic model named TL-HCRF is used, which produces a probability that a given candidate is a real one. If the probability is less than 0.5, the candidate is determined to be a non-birth event (case (b)). Among the remaining candidates that are closely placed one another in both time and location, only one candidate that has the greatest probability is confirmed as a detected birth event (case (c)); the other candidates are considered to be extracted from the neighboring patches to the same birth event and thus determined to be non-birth events (case (a)).

Examples of birth event candidates are illustrated in Figure 3.11(1). The details of this step is presented in Section 3.2.2.

Incorporation of Temporal Information: As shown in Figure 3.11(2), a candidate patch sequence is constructed by tracking a birth event candidate in the frames that precede and follow the candidate. Each birth event candidate is tracked rather than simply linked with the patches at the same location and orientation in the neighboring frames because mitotic cells often move by themselves or external forces. Tracking is performed based on HOG features [80]. Specifically, we first compute HOG features of a birth event candidate with the given position and orientation. Then, we find the closest patch (position and orientation) of the birth event in the preceding

41

frame in terms of the Euclidean distance between HOG features. With the patch found, the same process is repeated in the preceding frames. After tracking in the preceding frames, we track the birth event candidate in the succeeding frames in the same manner. We determine the spatial search range and the numbers of frames tracked using a typical validation scheme.

Validation of the candidates: For candidate validation, we propose a probabilistic model named Two Labeled Hidden Conditional Random Field (TL-HCRF). We defer the details of the learning and inference processes of TL-HCRF to Section 3.2.3. TL-HCRF outputs a probability that the candidate birth event in it is indeed a birth event. After applying TL-HCRF to each test candidate patch sequence, if the probability is less than 0.5, the candidate birth event is determined to be a non-birth event and excluded (e.g., case (b) in Figure 3.11). We further examine the remaining candidates since birth event candidates are often captured not only at a birth event, but also at its spatio-temporally neighboring patches; thus we need precisely localize birth event timing as well as to avoid duplicate detection of the same birth event. For this task, we first build a graph in which each node represents a birth event candidate. An edge is then added between two nodes if the corresponding candidates are closely located in the spatio-temporal volume. In each connected component in the graph, only one birth event candidate that has the greatest probability is determined to be a birth event (e.g., case (c) in Figure 3.11). The others are considered to be extracted from the neighboring patches to the same birth event and thus determined to be non-birth events (e.g., case (a) in Figure 3.11).

3.2.2 Cascaded Filtering for the Detection of Birth Event Candidates

We present a cascaded filtering framework, which consists of four steps: initial screening with basic features, filtering with appearance similarity to birth event samples, further filtering with RBF kernel Support Vector Machine (SVM) [117], and selecting a birth event candidate among each cluster of remaining cases. This scheme is different from conventional cascade schemes [125] in that different levels of filters are sequentially applied. As a result, easily recognizable non-birth
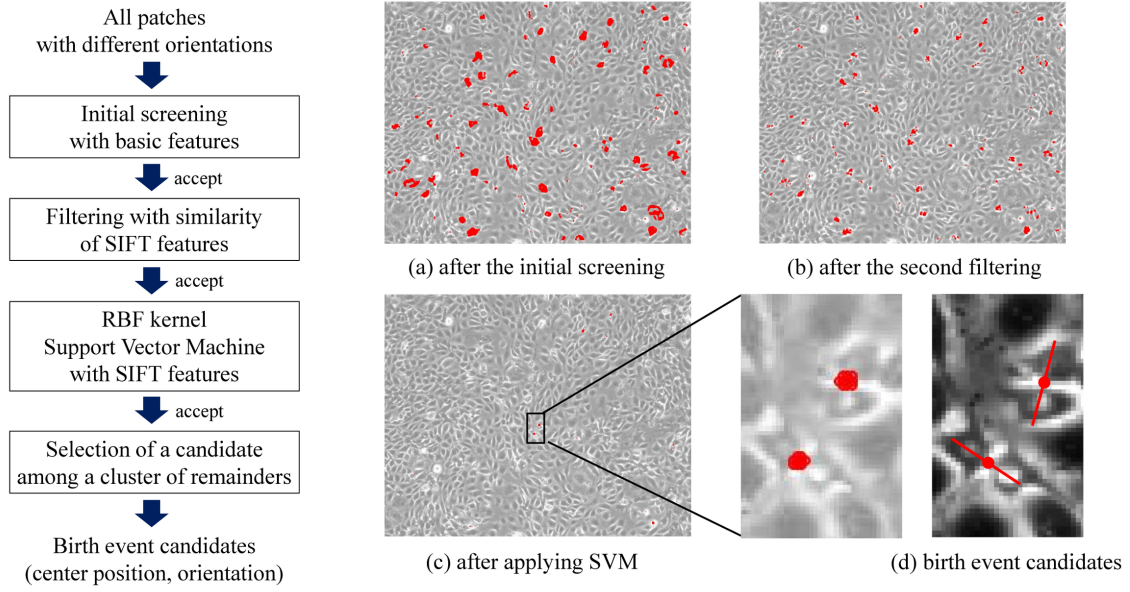
Figure 3.12: The procedure (left) and examples (right) of birth event candidate detection. Through cascaded filtering, the search space is reduced from the entire patches with various orientations in an image to birth event candidates, a small number of selected patches that are likely to contain a birth event. Red dots indicate the centers of candidate patches, i.e., the locations where birth events are possibly placed after (a) initial screening with basic features is performed; (b) filtering with similarity of HOG feature [80] to birth event samples is applied; (c) RBF kernel Support Vector Machine (SVM) with HOG features is applied; and (d) a birth event candidate is selected among each cluster of remaining patches. Orientation is not shown in (a)-(c) due to the limited space; in (d), the orientations of birth events are indicated by red lines. (Best viewed in color.)

events are first efficiently excluded by simple filters and then more difficult cases are examined by more complicated models, thereby resulting in both efficient computation and accurate detection. The overall procedure and examples of birth event candidate detection is demonstrated in Figure 3.12.

Initial Screening with Basic Features: As illustrated in Figure 3.13, we first model the appearance of a birth event using a combination of two small circles, one large circle, and one ellipse, which represent two daughter cell regions (D), halo region (H), and the contacting region of daughter cells (C), respectively. The radius of the daughter cell region is found to be roughly the average radius of newborn cells observed in the training image sequence. Based on this

43
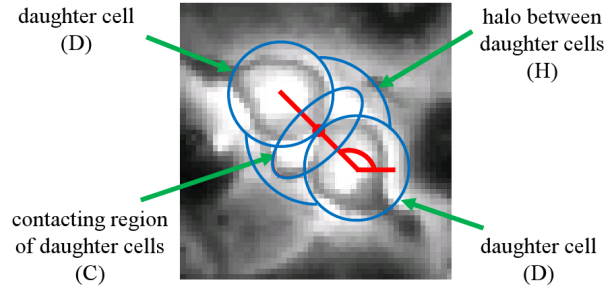
Figure 3.13: The appearance of a birth event is modeled with two small circles (radius=r), one large circle (radius=$\sqrt{2}r$), and one ellipse (major axis=$2r$, minor axis=r), which represent two daughter cell regions (D), the halo region (H), and the contacting region of two daughter cells (C), respectively. The large circle and the ellipse share the center position, which is the contact point of two small circles. The red dot in the center and the angle between the two red lines indicate the center and orientation of the patch, respectively.

model, the following four features are computed for a patch with a specific orientation in a gray-scale phase contrast microscopy image frame.

- *Brightness*: average pixel value in $D \cup H$

- *Brightness change*: difference between the average pixel values in $D \cup H$ and the same region in the previous frame

- *Brightness of the contacting region of two daughter cells*: average pixel value in C

- *Asymmetry*: difference between the average pixel values of the two half regions in $D \cup H$ divided by the major axis of the birth event, which is the line connecting the centers of daughter cells

These four features are carefully chosen based on the domain knowledge. For a birth event, the first two features are expected to be large because a typical birth event appears bright and shows considerable change in brightness and appearance compared to the previous frame. The third feature is also generally large at a birth event because a bright boundary separates two new-born cells when they are born. On the other hand, the last feature, asymmetry, is expected to be small at a birth event because typical mitotic and newborn cells are circular and thus symmetric with respect to the major axis of the birth event.

44
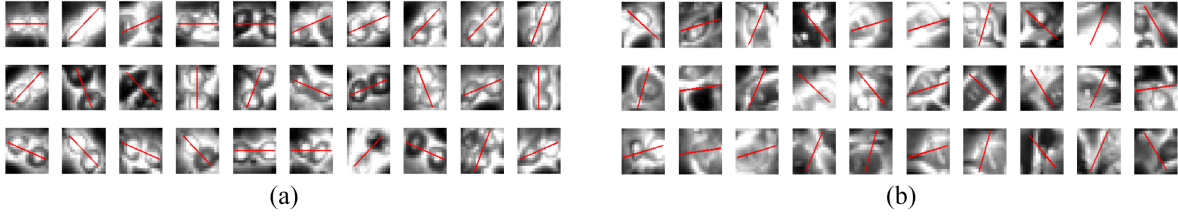
Figure 3.14: (a) Birth event samples obtained by manual annotation. (b) Remaining patches after the initial screening. These samples are extracted from where visual characteristics in terms of the four basic features including brightness are within the range of those of manually annotated samples.

We first compute the four basic features of birth events annotated in a training image sequence. Given a test image, we examine all patches that has the same size of the birth event model with different orientations to find the patches whose basic features are within the range of the features of annotated birth events.

Figure 3.14 shows the manually annotated birth event samples and examples of the remaining patches after this initial screening step. As can be seen, through this step, background and most of non-mitotic cells that are easily distinguishable from birth events are eliminated from the search space.

Filtering with Similarity of HOG features: In order to further reduce the search space, for each patch we compute HOG features [80] with fixed scale and a given orientation. The scale is fixed because scale change is minimal in microscopy cell images. The scale is set to be the size of the birth event model. We did not apply the original rotation invariance scheme of HOG since it does not reliably find a major axis of a birth event due to bright halo around the event. Instead, we consider 8 different orientations. We compute HOG features of remaining patches after the initial screening. Among the patches, those that do not have similar appearance to any birth event sample in terms of L2 distance of HOG descriptors are excluded from further consideration. We determine the threshold to keep as many as 30000 samples in the training sequence so that a Support Vector Machine (SVM) can handle them without extra resources.

Filtering with Support Vector Machine: The initial screening and the second filtering are

applied to a given training images where birth events are annotated. Among the remaining patches, we exclude actual birth events and use the remainder as negative samples while using the annotated birth events as positive samples. With these positive and negative samples, we train a Support Vector Machine (SVM) [117] with an RBF kernel. SVM parameters are determined by a validation scheme to maximize precision while achieving at least a certain level of recall in the training data. In our experiments, the level of recall was set to be 99%. To efficiently handle a large number of training samples, SVM^{light} [58] was used for implementation. The trained SVM was applied to the remaining patches from test image sequences.

Birth event candidate selection: After applying SVM, the remaining patches tend to form clusters as shown in Figure 3.12(c). Among the patches in each cluster, only the most probable patch is selected to contain a birth event candidate and the other patches are discarded. We select the patch that is located the farthest from the SVM decision boundary as the most probable one. As a result, candidate birth events are obtained, each of which is represented by a center position and an orientation in a microscopy image.

3.2.3 Two Labeled Hidden Conditional Random Fields

In this section, we formulate the Two Labeled Hidden CRF (TL-HCRF) model and describe its learning and inference processes. The main idea of TL-HCRF is to use the information regarding the most probable timing for a birth event, which is given by annotation or as the timing of the birth event candidate. By explicitly modeling this information, TL-HCRF has better modeling power than previous models that do not use the information. The graphical representations of TL-HCRF is shown in Figure 3.15.

TL-HCRF formulation: TL-HCRF has two label variables y and z as its name infers; given a sequence $\mathbf{x}$, y indicates whether $\mathbf{x}$ contains an event and z indicates which patch is the most
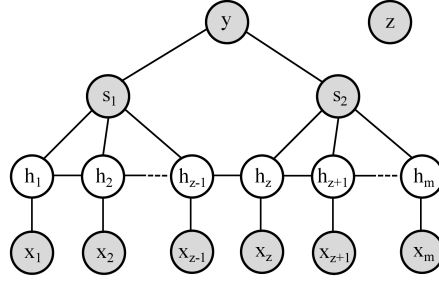
Two Labeled Hidden CRF

Figure 3.15: Graphical representation of Two Labeled Hidden CRF (TL-HCRF) model. Label y is a binary variable that indicates birth event occurrence. The other label z represents the most probable birth event timing and determines the model connectivity. s_1 and s_2 are sublabels that represent stages of cell division relative to the birth event. x_i represents the i-th observation, i.e., the i-th patch in a given candidate patch sequence. h_i represents the hidden state assigned on x_i. m denotes the number of patches in the candidate sequence. Gray circles indicate observed variables for training. For testing, y and s are not observed. Note that z is observed as the timing of the birth event candidate for testing.

likely to contain the event. More formally, in the training phase,

$$
y = \begin{cases} 1 & \text{if } \mathbf{x} \text{ contains an event} \\ 0 & \text{otherwise} \end{cases} \tag{3.14}
$$

$$
z = \begin{cases} p & \text{if the } p\text{-th patch of } \mathbf{x} \text{ contains an event} \\ q & \text{if there exists no event in } \mathbf{x} \end{cases} \tag{3.15}
$$

where the q-th patch contains an event candidate.

In the testing phase, y is not observed and thus needs to be inferred, while z is given as the timing of the event candidate, i.e.,

$$
z = q \tag{3.16}
$$

In other words, if an event exists in a given candidate patch sequence and the information is known by annotation, z is given as its timing. On the other hand, if an event does not occur or the information is not known, z is set as the timing of the event candidate in the patch sequence.

Note that p is not necessarily equal to q.

Suppose that observation $\mathbf{x}$ consists of m patches; i.e., $\mathbf{x} = (x_1, x_2, \cdots, x_m)$ where x_j denotes the j-th patch. We assume hidden variables $\mathbf{h} = (h_1, h_2, \cdots, h_m)$ where $h_j \in \mathcal{H}$ and $\mathcal{H}$ is a set of hidden states in the model. h_j corresponds to x_j for $j = 1, \cdots, m$. We also assume two sublabels s_1 and s_2. Given z, s_1 is connected with $h_1, h_2, \cdots, h_{z-1}$ while s_2 with $h_z, h_{z+1}, \cdots, h_m$ as shown in Figure 3.15. According to y, the sublabels s_1 and s_2 are set as

$$
\begin{cases}
s_1 = N, \ s_2 = N & \text{if } y = 0 \\
s_1 = B, \ s_2 = A & \text{if } y = 1
\end{cases}
\tag{3.17}
$$

where label N, B, and A represent *No event*, *Before the event*, and *After the event (including the event)*, respectively. In other words, if there exists an event in a given candidate sequence, the patches and hidden variables before the event are associated with a sublabel B while those after the event (including the event) with a sublabel A. Otherwise, all the patches and hidden variables are associated with a sublabel N.

TL-HCRF uses the information on the timing of the event candidate. In the testing phase, as the label z is set to be the timing of the candidate, the event timing is fixed rather than being inferred. Therefore, the inference is performed on only y to determine whether a birth event occurs in the frame where the candidate is placed. This restriction does not degrade the flexibility of the decision on event timing because the decision is performed in the postprocessing step among the neighboring event candidates.

Under the definitions, we define a latent conditional model:

$$
P(y|\mathbf{x}, z; \theta) = P(s_1, s_2|\mathbf{x}, z; \theta) = \sum_{\mathbf{h} \in \mathcal{H}^m} P(\mathbf{h}, s_1, s_2|\mathbf{x}, z; \theta)
\tag{3.18}
$$

where θ is a set of parameters of the model.

We define $P(\mathbf{h}, s_1, s_2|\mathbf{x}, z; \theta)$ using a log linear model as follows:

$$
P(\mathbf{h}, s_1, s_2|\mathbf{x}, z; \theta) = \frac{1}{Z} exp\big(\Psi(\mathbf{h}, s_1, s_2, \mathbf{x}, z; \theta)\big)
\tag{3.19}
$$

48

where Z is a partition function which is defined as

$$Z = \sum_{\substack{(s_1,s_2)\in \\ \{(N,N),(B,A)\}}} \sum_{\mathbf{h}\in\mathcal{H}^m} exp\big(\Psi(\mathbf{h}, s_1, s_2, \mathbf{x}, z; \theta)\big) \tag{3.20}$$

We define $\Psi(\mathbf{h}, s_1, s_2, \mathbf{x}, z; \theta)$ by extending the formulations of conditional random field (CRF) [67] and hidden conditional random field (HCRF) [109].

$$\Psi(\mathbf{h}, s_1, s_2, \mathbf{x}, z; \theta) = \sum_{j=1}^{m} f^{(s)}(h_j, \mathbf{x}, j) \cdot \theta^{(s)}(h_j) \tag{3.21}$$

$$+ \sum_{j=2}^{z-1} f^{(t)}(h_{j-1}, h_j, \mathbf{x}, j) \cdot \theta^{(t)}(h_{j-1}, h_j, s_1, s_1) + f^{(t)}(h_{z-1}, h_z, \mathbf{x}, k) \cdot \theta^{(t)}(h_{z-1}, h_z, s_1, s_2)$$

$$+ \sum_{j=z+1}^{m} f^{(t)}(h_{j-1}, h_j, \mathbf{x}, j) \cdot \theta^{(t)}(h_{j-1}, h_j, s_2, s_2) + \sum_{j=1}^{z-1} \theta^{(l)}(h_j, s_1) + \sum_{j=z}^{m} \theta^{(l)}(h_j, s_2)$$

where $f^{(s)}(h_j, \mathbf{x}, j)$ and $f^{(t)}(h_{j-1}, h_j, \mathbf{x}, j)$ are state and transition functions, respectively; $\theta^{(s)}$ and $\theta^{(t)}$ are the parameters of state and transition functions, respectively; and $\theta^{(l)}$ is the parameter associated with sublabels; thus, $\theta = \{\theta^{(s)}, \theta^{(t)}, \theta^{(l)}\}$.

State and transition functions are defined as

$$f^{(s)}(h_j, \mathbf{x}, j) = \phi(x_j), \quad f^{(t)}(h_{j-1}, h_j, \mathbf{x}, j) = 1 \tag{3.22}$$

where $\phi(x_j)$ is a visual feature vector of x_j. We use a HOG [80] vector with a fixed scale from each patch as visual features in our experiments.

Learning model parameters: Suppose that n pairs of candidate patch sequences and corresponding labels $\{(\mathbf{x_1}, (y_1, z_1)), (\mathbf{x_2}, (y_2, z_2)), \cdots, (\mathbf{x_n}, (y_n, z_n))\}$ are given for training. For learning parameters, we maximize the following regularized log-likelihood function [66, 67].

$$L(\theta) = \sum_{i=1}^{n} \log P(y_i|\mathbf{x_i}, z; \theta) - \frac{1}{2\sigma^2}||\theta||^2 \tag{3.23}$$

where σ is the variance of a Gaussian prior.

This optimization problem can be solved by gradient ascent methods. Let $\theta^{(s)}[h]$ be the parameter vector in $\theta^{(s)}$ that corresponds to a certain hidden state h and $\theta_k^{(s)}[h]$ be the k-th element

of $\theta^{(s)}[h]$. Then, the derivative of $\log P(y|\mathbf{x}, z; \theta)$ with respect to $\theta_k^{(s)}[h]$ is computed as

$$\frac{\partial \log P(y|\mathbf{x}, z; \theta)}{\partial \theta_k^{(s)}[h]} = \sum_{j=1}^{m} P(h_j = h|s_1, s_2, \mathbf{x}, z; \theta)\phi_k(x_j)$$

$$- \sum_{\substack{(s_1, s_2) \in \\ \{(N,N),(B,A)\}}} \sum_{j=1}^{m} P(h_j = h, s_1, s_2|\mathbf{x}, z; \theta)\phi_k(x_j) \qquad (3.24)$$

where $\phi_k(x_j)$ is the k-th element of $\phi(x_j)$. $P(h_j = h|s_1, s_2, \mathbf{x}, z; \theta)$ can be computed by belief propagation [102] in $O(m)$ [89].

Let $\theta^{(t)}[h', h'', s', s'']$ be the parameter in $\theta^{(t)}$ that corresponds to two sublabels s' and s'' and two hidden states h' and h'' where h' and h'' are associated with s' and s'', respectively. Then the derivative of $\log P(y|\mathbf{x}, z; \theta)$ with respect to $\theta^{(t)}[h', h'', s', s'']$ is computed as

$$\frac{\partial \log P(y|\mathbf{x}, z; \theta)}{\partial \theta^{(t)}[h', h'', s', s'']} = \sum_{j=2}^{m} P(h_{j-1} = h', h_j = h''|s_1, s_2, \mathbf{x}, z; \theta)g_1(s', s'', j, y, z)$$

$$- \sum_{\substack{(s_1, s_2) \in \\ \{(N,N),(B,A)\}}} \sum_{j=2}^{m} P(h_{j-1} = h', h_j = h'', s_1, s_2|\mathbf{x}, z; \theta) \qquad (3.25)$$

where $g_1(s', s'', j, y, z)$ is defined as

$$g_1(s', s'', j, y, z) = \qquad\qquad\qquad\qquad\qquad\qquad\qquad\qquad\qquad (3.26)$$

$$\begin{cases} 1 & \text{if } y = 0 \text{ and } (s', s'') = (N, N) \\ 0 & \text{if either } y = 0 \text{ and } (s', s'') \neq (N, N) \text{ or } y \neq 0 \text{ and } (s', s'') = (N, N) \\ I(j < z) & \text{if } y \neq 0 \text{ and } (s', s'') = (B, B) \\ I(j = z) & \text{if } y \neq 0 \text{ and } (s', s'') = (B, A) \\ I(j > z) & \text{if } y \neq 0 \text{ and } (s', s'') = (A, A) \end{cases}$$

where $I(x)$ is an indicator function; i.e., $I(x)$ is 1 if x is true, 0 otherwise. Note that when optimizing the parameter for the transition function, we consider four different sublabel transitions, namely, $(s', s'') \in \{(N, N), (B, B), (B, A), (A, A)\}$, which represent *no event*, *before*

the event, *during the event*, and *after the event*, respectively. Similar to the optimization of $\theta^{(s)}$, $P(h_{j-1} = h', h_j = h''|s_1, s_2, \mathbf{x}, z; \theta)$ can also be efficiently computed by belief propagation.

Lastly, let $\theta^{(l)}[h, s]$ be the parameter in $\theta^{(l)}$ that corresponds to a sublabels s and a hidden states h. Then the derivative of $\log P(y|\mathbf{x}, z; \theta)$ with respect to $\theta^{(l)}[h, s]$ is computed as

$$\frac{\partial \log P(y|\mathbf{x}, z; \theta)}{\partial \theta^{(l)}[h, s]} = \sum_{j=1}^{m} P(h_j = h|s_1, s_2, \mathbf{x}, z; \theta) g_2(s, j, y, z) \tag{3.27}$$

$$- \sum_{\substack{(s_1, s_2) \in \\ \{(N,N),(B,A)\}}} \sum_{j=1}^{m} P(h_j = h, s_1, s_2|\mathbf{x}, z; \theta)$$

where $g_2(s, j, y, z)$ is defined as

$$g_2(s, j, y, z) = \begin{cases} 1 & \text{if } y = 0 \text{ and } s = N \\ 0 & \text{if either } y = 0 \text{ and } s \neq N \text{ or } y \neq 0 \text{ and } s = N \\ I(j < z) & \text{if } y \neq 0 \text{ and } s = B \\ I(j \geq z) & \text{if } y \neq 0 \text{ and } s = A \end{cases} \tag{3.28}$$

Using the derivatives in Eqs. (3.24) through (3.28), we can find the optimal parameter θ^* that maximizes the objective in Eq. (3.23).

Inferences: For each candidate patch sequence extracted from test image sequences, the model produces the probability that the event candidate in the patch sequence is indeed an event. Let the candidate patch sequence be $\mathbf{x} = (x_1, x_2, \cdots, x_m)$ where x_j denotes the j-th patch. Aforementioned, z is set as the timing of the birth event candidate, i.e., the z-th patch in the candidate patch sequence contains the birth event candidate. In order to infer y, which is a variable indicating birth event occurrence, we compute $P(y = 1|\mathbf{x}, z; \theta^*)$ where θ^* is the optimal model parameter obtained in the training step. This conditional probability can be calculated using Eqs. (3.18) through (3.21).

(a) birth events in C2C12   (b) birth events in BAEC
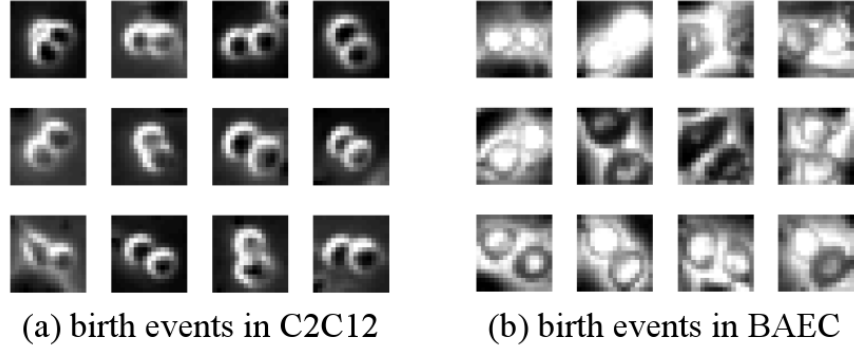
Figure 3.16: Birth events of two types of cells: (a) C2C12 and (b) BAEC.

Based on the conditional probability, the label y is determined to be

$$
y^* = \begin{cases} 1 & \text{if } P(y = 1|\mathbf{x}, z; \theta^*) \geq 0.5 \\ 0 & \text{otherwise} \end{cases} \tag{3.29}
$$

3.2.4   Experiments

In this section we describe the process to acquire datasets and ground truth, and the methodology to evaluate the proposed method against previous methods.

Data and Ground truth: To test the proposed birth event detection algorithm, we produced six time-lapse phase contrast microscopy: one image sequence capturing C2C12 cells (C2C12) under control condition and the other five image sequences capturing bovine aortic endothelial cells (BAEC) under different culture conditions, as shown in Table 3.4. To develop different culture conditions, different amounts of a cell-permeable reagent were added on the cell populations. Note that different cell types and culture conditions often lead to different visual characteristic of birth events. (e.g., see Figure 3.16.) Testing an image processing algorithm on multiple cell types and culture conditions is important because such a test can show how robust the algorithm is and whether it can possibly be used for the analysis of real-world biological data.

For C2C12 and BAEC image sequences, images were acquired every five minutes for 84 and 19 hours, obtaining 1013 and 228 frames, respectively. Each image contains 1040×1392 pixels

Sequence	Culture condition	No. of birth events
C2C12	control (no reagent)	680
BAEC0	control (no reagent)	468
BAEC1	control (no reagent)	401
BAEC2	1nM Latrunculin B	333
BAEC3	10nM Latrunculin B	346
BAEC4	100nM Latrunculin B	266

Table 3.4: Specification of the six image sequences used for the experiments. For the C2C12 sequence, the last 100 frames containing 141 birth events were used for testing and the other frames for training. For the BAEC sequences, an image sequence under control condition (BAEC0) was used for training and the other four sequences (BAEC1-4) under different culture conditions in terms of the amount of reagent Latrunculin B for testing.

(a) Frame 42   Frame 43   Frame 44   Frame 45   Frame 46   Frame 47

(b) Frame 206 Frame 207 Frame 208 Frame 209 Frame 210 Frame 211
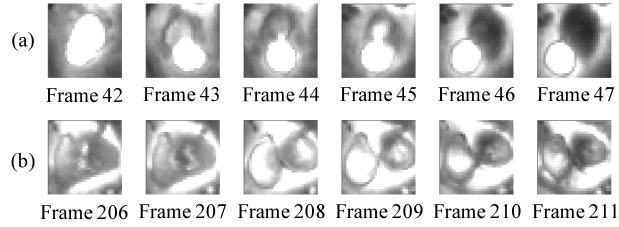
Figure 3.17: Two examples on which annotated birth event timings by different operators were not consistent. (a) A birth event was annotated on one of frames 43, 44, and 46. (b) Either of frames 208 and 209 was annotated to contain a birth event.

with a resolution of 1.3μm/pixel. A few frames in BAEC image sequences were blurred due to out of focus.

Manual annotation of birth events was performed on all the sequences. For each birth event, the contacting point of the two daughter cells was marked when the daughter cells are first separately identified. If the birth event timing is ambiguous (e.g., see Figure 3.17), the most probable birth event timing was guessed and marked. Several people annotated birth events in the sequences and we merged the annotations into one by manually examining inconsistent cases. The total number of birth events in each sequence is reported in Table 3.4.

For C2C12, the last 100 frames were used for testing and the remaining frames for training.

	Precision	Recall	F-measure	AUC of PR-curve	Average timing error (frame)
C2C12	0.977	0.920	0.947	0.943	0.476
BAEC1	0.921	0.939	0.930	0.949	0.437
BAEC2	0.954	0.965	0.959	0.972	0.404
BAEC3	0.932	0.942	0.937	0.941	0.333
BAEC4	0.904	0.949	0.926	0.940	0.456
Average	0.938±0.029	0.943±0.016	0.940±0.013	0.949±0.013	0.421±0.056

Table 3.5: Birth event detection results of the proposed approach on the five test sequences. A timing error is measured for each true positive case as the frame difference between the frames where the birth event is detected and annotated.

For BAEC, the first sequence was used for training, and the other four sequences for testing. The cell confluence of BAEC is much higher than C2C12; in C2C12 sequence, approximately half of the field of view is covered with cells in the last 100 frames while in BAEC sequences, most of the field of view except for the wound area is covered with cells in contact with one another.

For the training data, we additionally annotated the orientation of every birth event, which is the angle that the line connecting the centers of two daughter cells forms with the horizontal axis. The orientation was then discretized into one of 0, π/k, $\cdots$, $(k-1)\pi/k$. In our experiments, k is set to be 8.

Evaluation: To measure the performance of our approach, we compute precision and recall on a condition of birth event location and timing. Specifically, if a detection result is located spatially within th_s pixels and temporally within th_t frames from an annotated birth event, it is considered correctly detected (true positive). In our experiments, th_s is set to be 16 pixels (8 pixels in downsampled images) for both C2C12 and BAEC, which is roughly the diameter of a newborn cell observed from the training sequence; th_t is set to be 5 frames for C2C12 and 2 frames for BAEC, which are the average frame difference between the frames where a birth event occurs and the two daughter cells start to stretch out and become dark. These location and timing errors are allowed because such variations in location and timing are also often observed

in human annotations. A detection that does not satisfy this condition is regarded incorrect (false positive). If more than one detection result are located close to one annotated birth event with satisfying the condition, the detection that is temporally the closest to the annotation is considered correct (true positive) and the others incorrect (false positives).

In addition to precision and recall, in order to compare different approaches and models, we compute F-measure and AUC of the precision-recall curve (PR-curve). F-measure is defined as the harmonic mean of precision and recall. AUC is computed as the area under the PR-curve that is plotted by varying the decision probability in Eq. (3.29) from 0 to 1. We also compute the average timing error by averaging all timing differences between detected results and corresponding human annotations in terms of the number of frames for all true positive cases.

Running time is measured on a desktop with 3GHz CPU and 4GB memory. The algorithm was implemented using Matlab with C mex files.

Comparison with previous methods: We compare the proposed approach with the approach introduced in Section 3.1. We also compare our model TL-HCRF with two previous probabilistic models: HCRF [126] and EDCRF. We refer to Section 3.1.2 for details of these models.

3.2.5   Results and Discussions

In this section, we report the experimental results of the proposed approach and compare them with the previous methods.

Performance of the proposed approach: The proposed approach achieved an average precision of 93.8% and an average recall of 94.3% on the five test sequences containing more than 1000 birth events of C2C12 and BAEC as reported in Table 3.5. The average F-measure and AUC were 94.0% and 94.9%, respectively. The average timing error in terms of the number of frames was 0.333 to 0.476, which means that the majority of birth events are detected at the frame where they are annotated or at its neighboring frames. Figures 3.18 and 3.19 show examples of birth event detection results.

(a) manual annotation

(b) detection results
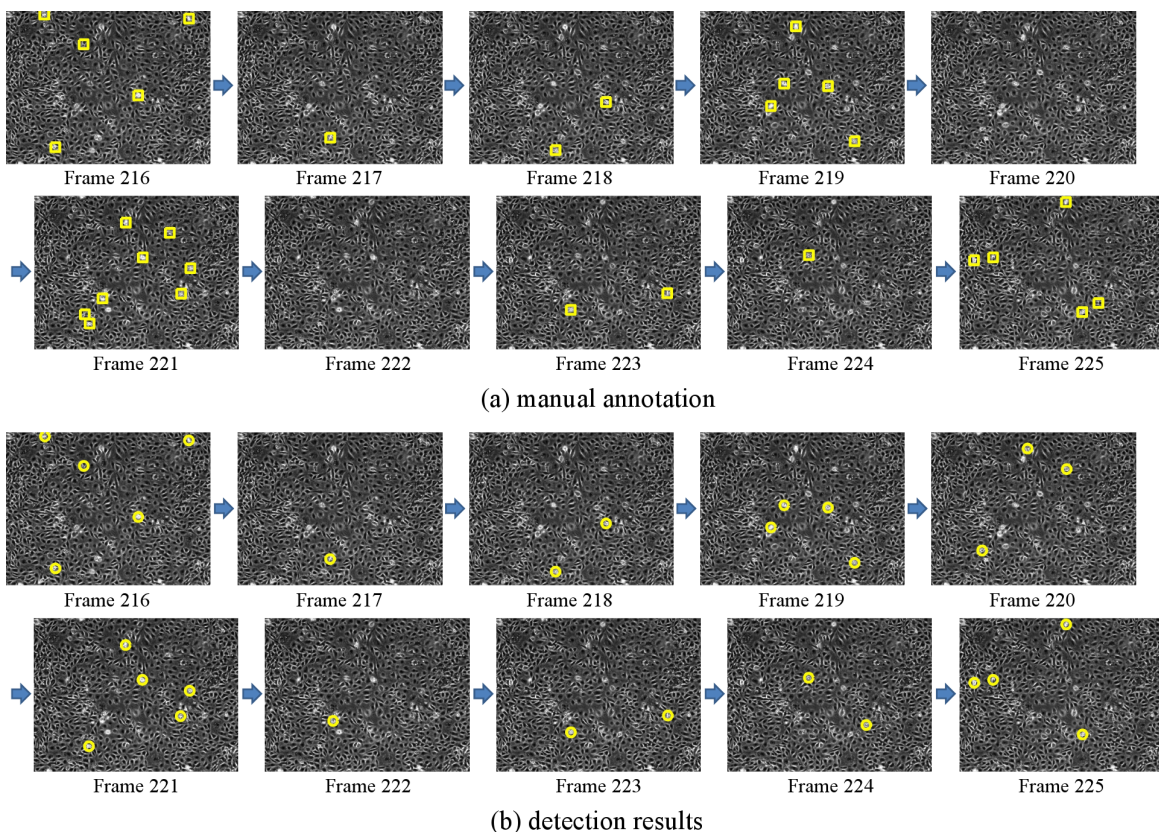
Figure 3.18: Birth event detection results on the last ten frames in BAEC2. (a) A yellow box encloses an annotated birth event. (b) A yellow circle surrounds a birth event detected by the proposed algorithm. All 29 birth events are correctly detected at the frame annotated or its neighboring frames.

The algorithm achieves similar performances on different cell types, even though their birth events show quite different appearance (See Figure 3.16.). This result implies that the proposed algorithm can be applied to various cell types as long as manual annotation is available. As the amount of reagent varies and thus culture condition changes, the algorithm shows stable performance, not significant variation; at the low concentration of the reagent (BAEC2), the performances in terms of F-measure and AUC or PR-curve even increased by 2.9% and 2.3%, respectively, compared to control condition (BAEC1) while at the high concentration (BAEC4), the performances slightly drops by 0.4% and 0.9%. Note that the training samples for BAEC sequences were obtained under control condition. This result proves that the proposed method is robust to the small variation of visual characteristics of birth events due to the culture condition

56
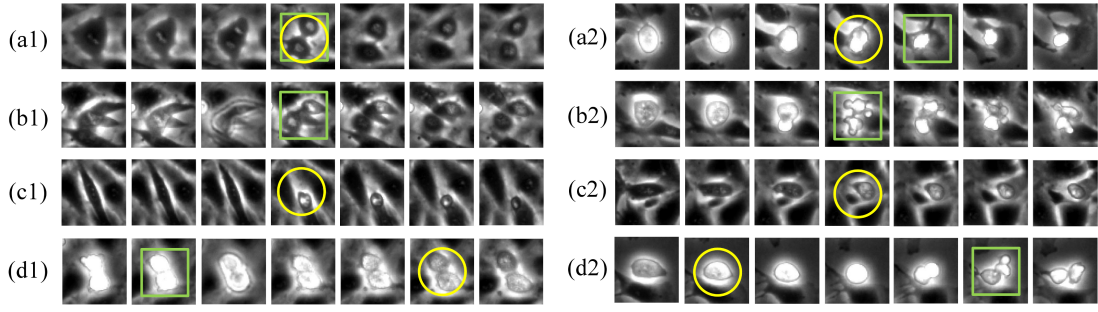
Figure 3.19: Examples of birth event detection results on BAEC sequences: (a1-2) true positives, (b1-2) false negatives, (c1-2) false positives, (d1-2) false negatives and positives due to the timing error. A green box encloses an annotated birth event while a yellow circle surrounds a detected birth event by the proposed algorithm. (a1) A dark birth event is correctly detected. (a2) A birth event where one daughter cell stretches out earlier than the other is correctly detected with one frame timing error. (b1) The frame right before a birth event is blurred due to out of focus. In addition, when the birth event occurs, another cell passes through between the two daughter cells. (b2) The appearance of the birth event is quite different from a typical figure eight shape as cell culture condition changes. (c1) A cell shrinks and becomes bright without involving a birth event. (c2) A cell that becomes circular and slightly bright aligns to its neighboring cell. (d1) A patch during mitosis is blurred due to out of focus. (d2) The birth event shape is uncommon possibly due to culture condition change.

	Proposed approach (F-measure / AUC)	Previous approach (F-measure / AUC)
C2C12	0.947 / 0.943	0.780 / 0.727
BAEC1	0.930 / 0.949	0.342 / 0.220
BAEC2	0.959 / 0.972	0.286 / 0.185
BAEC3	0.937 / 0.941	0.259 / 0.141
BAEC4	0.926 / 0.940	0.151 / 0.080

Table 3.6: Birth event detection performance comparison against the previous approach in Section 3.1 in terms of F-measure and AUC on the C2C12 and BAEC sequences.

change.

In the training phase, TL-HCRF training dominates the other modules in computational cost. In our experimental setting, learning a TL-HCRF model took 15 minutes and we repeated it

20 times with random initialization in order to find a better model because for each run, not the globally optimal model, but a locally optimal model is found. After multiple modeling, the model that has the lowest training error is selected and used for testing. Note that this modeling step can easily be parallelized to reduce the overall execution time. The birth event candidate detection step can also be parallelized since it is separately performed for individual images. In test phase, each image was processed in 30 seconds in our experiments. Since the image acquisition time interval is generally a few minutes (5 minutes in our experiments), birth event detection can be conducted in real-time manner with a short latency, which is necessary to incorporate temporal information.

Comparison with the previous approach: The proposed approach significantly outperforms the previous approach in terms of F-measure and AUC of the PR-curve as reported in Table 3.6. Note that the previous approach reported over 90% accuracy on relatively low confluence data. When approximately half of field of view is occupied by cells (C2C12), this approach shows 70%-80% accuracy. However, as the whole field of view is covered with cells that are in contact with one another (BAEC1-4), its performance dramatically drops into less than 40%. These results clearly reveal that the previous approach is challenged by high cell confluence. Furthermore, as the concentration of the reagent increases, the performance of the approach rapidly decreases, indicating that it is not robust to the change in cell appearances cause by culture condition change.

At high cell confluence, bright halos are often observed among the cells in contact with one another and bright cells are sometimes touching. In such cases, the previous method often fails in precisely locating a birth event candidate because the center of birth event candidate is estimated by the center of a bright patch, which may contain halo or a part of another cell in addition to the cell of interest. In addition, the previous method tends to nominate halo among clustered cells as a birth event candidate based on brightness due to the lack of specified birth event candidate detection. As a result, a lot more birth event candidates are detected, resulting in

58

	F-measure			AUC of PR-curve		
	TL-HCRF	HCRF	EDCRF	TL-HCRF	HCRF	EDCRF
BAEC1	0.930	0.889	0.902	0.949	0.900	0.914
BAEC2	0.959	0.910	0.908	0.972	0.930	0.930
BAEC3	0.937	0.898	0.897	0.941	0.929	0.921
BAEC4	0.926	0.860	0.834	0.940	0.930	0.892
Average	0.938±0.015	0.889±0.021	0.885±0.034	0.951±0.015	0.922±0.015	0.914±0.016

Table 3.7: Birth event detection performance comparison among the three probabilistic models (TL-HCRF, HCRF, and EDCRF) in terms of F-measure and AUC of the PR-curve on BAEC sequences. For this comparison, each model is applied to each candidate patch sequence to determine the birth event candidate is true one.

decreased the overall performance. Moreover, since the orientation of birth events is not taken into account in the previous approach, it is not effective at classifying confusing cases, which are more prevalent at the culture condition with higher concentration of the reagent. On the other hand, in the proposed approach, birth event candidates are detected not only by brightness cue but also by cascaded filtering with considering the orientation of birth events, thereby obtaining fewer quality birth event candidates and subsequently achieving higher birth event detection performance.

Comparison with the previous models: Table 3.7 shows that TL-HCRF outperforms the previous two models, HCRF and EDCRF, in terms of both F-measure and AUC of PR-curve on birth event detection in BAEC sequences. The results on the C2C12 sequence are comparable to one another as birth event candidates in C2C12 do not contain many confusing cases that require temporal investigation due to relatively low cell confluence. To produce these results, we replaced TL-HCRF with HCRF or EDCRF in the proposed approach. Only the parameters on the number of frames tracked before and after each birth event candidate are tuned for each model; the other settings or modules are the same for all models.

TL-HCRF is superior to HCRF on the given task. Since HCRF has only one label variable that represents the occurrence of event, the model is intrinsically not capable of modeling the

Model	TL-HCRF	HCRF	EDCRF
Modeling time (min)	15.52	26.68	83.95

Table 3.8: Modeling time comparison among the three probabilistic models: TL-HCRF, HCRF, and EDCRF. After 20 runs, the average time was reported.

timing of an event. In our approach, this drawback is somewhat compensated in the postprocessing step, which determines the most appropriate timing of a birth event among neighboring candidates. Thanks to the postprocessing step, the performance of HCRF can be comparable to that of EDCRF, but cannot still reach that of TL-HCRF on the given task.

TL-HCRF is also superior to EDCRF on the given task. EDCRF can model event timing, but it assumes that an event can occur at any patch in a candidate patch sequence rather than focusing on the timing of the event candidate. In our framework which involves birth event candidate detection, EDCRF ignores the information on the timing of birth event candidates and exercises excessive modeling power than necessary. In addition, in order to make the inference of all sublabels tractable, EDCRF restricts each sub-class label to be associated only with hidden states in a disjoint set [89] unlike HCRF or TL-HCRF, which may additionally degrade the overall performance.

Table 3.8 shows the running time comparison among the three probabilistic models. We performed the model training 20 times and report the average. TL-HCRF is comparable to HCRF in computational cost. Although TL-HCRF has more parameters than HCRF due to the sublabels, modeling of TL-HCRF generally takes a shorter time than modeling of HCRF because TL-HCRF separately models the stages before and after the event, which show a totally different pattern on visual change. Modeling of such a case together generally takes longer time to converge. TL-HCRF is more efficient than EDCRF in computational cost. EDCRF involves a lot more variables than HCRF due to the restriction on association between sublabels and hidden states, resulting in increased computational cost in modeling.

3.3 Mitosis Detection for Non-adherent Cells

The mitosis detection methods introduced in the previous sections rely on dramatic morphological and brightness changes of mitotic cells, which happen to adherent cells that are attached to the surface of a petri dish. Therefore, the methods may not be effective for non-adherent cells that are free-floating in the culture medium. Due to its non-adherence, such dramatic alterations in cell shape and intensity do not accompany mitosis of non-adherent cells.

In this section, we present an automated birth event method in time-lapse phase contrast images developed particularly for non-adherent cells [54]. We adopt the three-step framework for event detection, which comprises detection of candidates, incorporation of temporal information, and validation of the candidates. Contrary to the previous work that examines cell appearance and intensity changes, birth event candidate detection is performed based on cell region detection and tracking, which is fairly tractable in a non-adherent population due to their limited variation in cell shape and size. For each newly appeared cell during cell tracking, we examine it with its potential mother and sibling cells to determine whether it is a newborn cell as a result of mitosis. We performed experiments on 14 hematopoietic stem cell (HSC) populations, each of which was captured for four days.

3.3.1 Algorithm

In this section, we propose a three-step method for birth event detection: (1) candidate detection by cell region detection and tracking, (2) incorporation of temporal information, and (3) candidate validation using a probabilistic temporal model.

Candidate Detection by Cell Region Detection and Tracking: We first detect cell regions in each image and link them over consecutive frames using a tracking method based on frame-by-frame data association. Non-adherent cells generally appear as round objects surrounded by bright halos in phase contrast microscopy images as shown in Figure 3.20. Hence, the method based on a template matching with ring filters [39] is effective for the detection of non-adherent
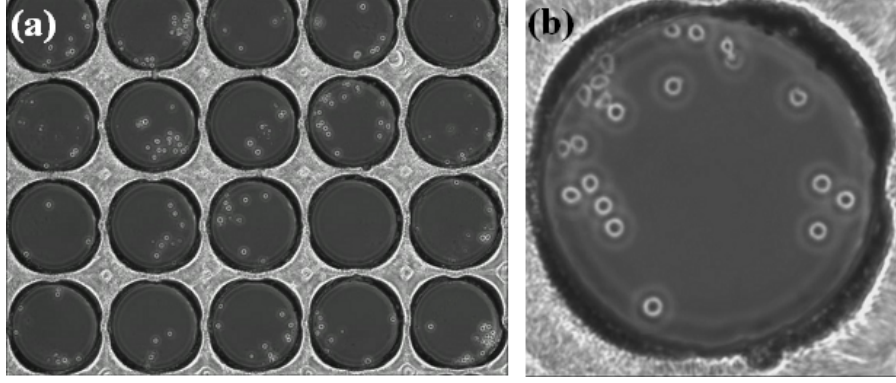
Figure 3.20: Hematopoietic stem cells (HSCs), which are one of the most popularly used non-adherent cells, (a) in a microwell array and (b) in a single microwell, imaged with phase contrast microscopy.
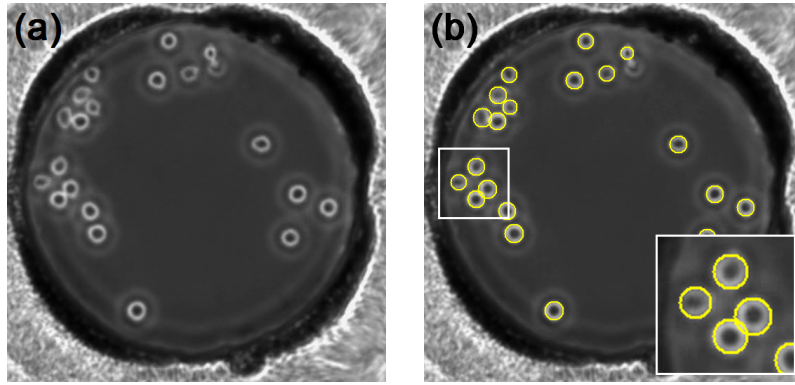
Figure 3.21: (a) Sample input image. (b) Cell regions detected on the sample image.

cells and is known to outperform other methods based on Hough transform [5] and correlation [65]. The brief summary of the method is as follows.

Ring filters with different radii are convolved with a given image. In order to prevent the background regions surrounded by cells from being detected, the roundness of ring pattern is computed and multiplied to the convolved result. After thresholding the weighted filter outputs, local maxima are found among them in the space dimension for each radius. Each local peak is then adjusted with a fitting scheme using a quadratic polynomial surface model. For each adjusted local peak, which is considered the center of a cell, the radius with the maximum filtered output in the radius space is selected as the radius of the cell. Figure 3.21 shows a sample input image and the detected cell regions on the image.

After cell region detection, we linked the cell regions over consecutive frames based on a typical one-to-one frame-by-frame data association method. Specifically, in order to associate a set of tracks up to frame $t-1$, denoted by $\{T_i\}$, with a set of cells at frame t, denoted by $\{C_j\}$, the likelihood that each track is associated with each cell is computed based on the distance between them as follows:

$$\ell(T_i, C_j) = e^{-a \cdot p_i} \max \left(1 - \left(\frac{dist(T_i, C_j)}{d_{max}} \right)^2, 0 \right) \tag{3.30}$$

where a is a constant, p_i is the number of frames for which T_i is unassigned to a cell in a row until reaching frame $t - 1$, and d_{max} is the maximum distance that a cell can move between two successive frames. $e^{-a \cdot p_i}$ is multiplied to penalize the tracks that fail to be associated with a cell. Morphological similarity is not taken into account for the likelihood computation because it is not informative due to the limited variation in shape and size among HSCs.

We find the best set of one-to-one correspondences between tracks $\{T_i\}$ and cells $\{C_j\}$ that maximizes the total likelihood using a typical global nearest neighbor (GNN) scheme based on the Munkres algorithm [15]. After the association, there may be several tracks and cells that are not associated with any cell and track, respectively. Remaining tracks undergo another round of association with cells in the following frame with the penalty $e^{-a \cdot p_i}$ in Eq. (3.30). If a track is not associated with any cell for K frames in a row, the track is determined to be lost and thus no longer considered. Remaining cells are tracked and observed for K following frames. If a remaining cell is detected for at least $\lceil 0.5K \rceil$ frames out of the K frames, it is considered a newly appeared cell and a new track initiates from the cell. Otherwise, the remaining cell is regarded as misdetected and thus ignored.

We examine each of newly appeared cells and it is considered a candidate newborn cell if it satisfies two criteria: (1) it is in contact with another cell, which is its potential sibling cell and (2) its potential mother cell is sufficiently greater than it and its potential sibling cell. Note that, during the cell cycle, newborn daughter cells are smaller in size than the mother cell and
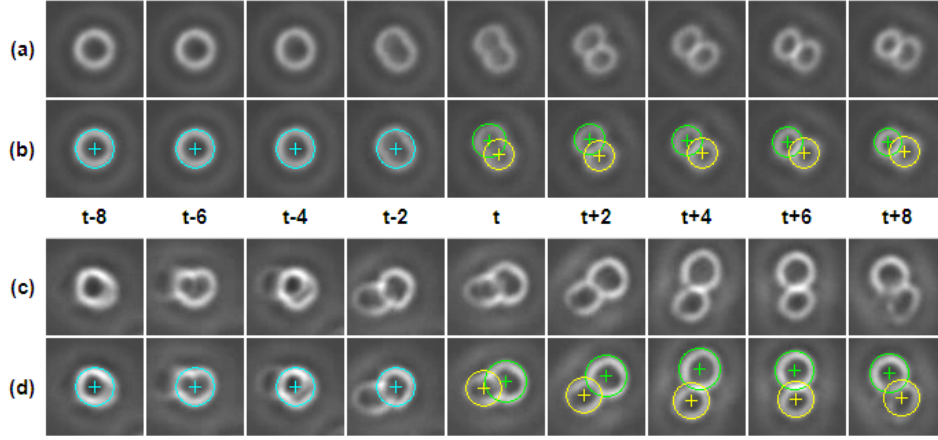
Figure 3.22: (a,c) Patch sequences showing mitosis. (b,d) Detection results of a candidate newborn cell (yellow), and its potential sibling (green) and mother (cyan) cells on (a) and (c), respectively. A circle and a cross in it indicate the boundary and the center of a cell detected, respectively. Newly appeared cells are first detected at frame t. (Best viewed in color.)

eventually grow and reach a similar size to the mother cell. The detailed process to locate a birth event candidate is as follows.

Suppose that a newly appeared cell (C_{extra}) is first detected at frame t. We find the cells in contact with C_{extra} at frame t as candidate sibling cells. If there is no such a cell, the first criterion is violated and thus C_{extra} is not further considered. For each of the possible sibling cells ($C_{sibling}$), we find a cell that is associated with $C_{sibling}$ at frame $t - 1$ and regard the cell as the potential mother cell (C_{mother}) of C_{extra} and $C_{sibling}$. In other words, we set a hypothesis that C_{mother} at frame $t - 1$ divides into C_{extra} and $C_{sibling}$ at frame t. From the tracking results, we obtain the trajectory of C_{mother} for K frames prior to frame t, and the trajectories of C_{extra} and $C_{sibling}$ for K frames at and after frame t. If the average radius of C_{mother} at frames $t - K$ through $t - 1$ is not at least 10% greater than either of the average radii of C_{extra} and $C_{sibling}$ at frames t through $t + K - 1$, the second criterion is not satisfied and thus C_{extra} is disqualified as a candidate newborn cell. Figure 3.22 shows examples of a candidate newborn cell and its potential sibling and mother cells.

Incorporation of Temporal Information: While we detect candidate newborn cells, we
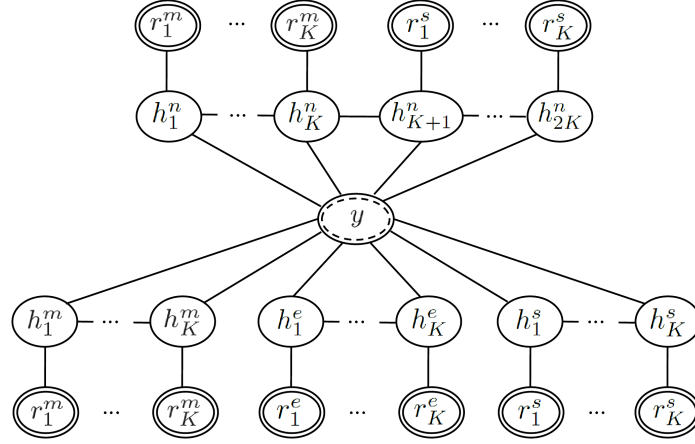
Figure 3.23: Graphical representations of the proposed model used for the validation of a birth event candidate. This model combines four Hidden Conditional Random Fields (HCRFs) that model cell size change of (1) a non-mitotic cell for the case that mitosis does not occur, (2) a newborn cell, (3) its mother cell, and (4) its sibling cell for the case that mitosis occurs. y is a binary variable that indicates the occurrence of mitosis. This label is only observed for training and needs to be inferred for testing. h^n, h^e, h^m, and h^s are hidden variables for the aforementioned four cases, and r^n, r^e, r^m, and r^s are radii of the cells in the cases. Features from the mother and daughter cells are extracted from K consecutive frames before and after a candidate birth event, respectively.

locate their potential sibling and mother cells. From the tracks of each candidate newborn cell and its potential sibling and mother cells, we incorporate temporal information on how the cell size changes over time. More formally, from the tracks of C_{extra}, $C_{sibling}$, and C_{mother}, we extract the following properties:

- At each of frames $t - K$ through $t - 1$

    - the radius of C_{mother} ($r^m_{1:K}$)

- At each of frames t through $t + K - 1$

    - the radii of C_{extra} and $C_{sibling}$ ($r^e_{1:K}$ and $r^s_{1:K}$)

We set K to be 20 in our experiments because 10 min, which is equivalent to 20 frames in our setting, is sufficient for investigating the change of mother or daughter cells due to mitosis. This parameter should be determined based on the image acquisition interval and mitosis duration.

Validation of Mitosis Candidates: We identify true mitosis among the candidates by statis-

tically modeling changes in cell size over time. We formulate a probabilistic model that combines four Hidden CRFs (HCRF) [109] together, as shown in Figure 3.23. In this model, binary label variable y indicates the occurrence of mitosis. The first HCRF component with hidden variables $h_{1:2K}^n$, which are connected with the cell sizes of both potential mother and sibling cells, models non-mitotic events; if there occurs no mitosis, the potential mother and sibling cells, which are extracted from the same trajectory, are turned to be one non-mitotic cell and thus the sequentially combined features capture cell size change of a non-mitotic cell over time. On the other hand, the other three HCRF components model cell size change of a mother and two daughter cells separately when mitosis occurs. Combining these four HCRF components together, the proposed model can effectively distinguish mitotic events from non-mitotic ones.

More formally, we define an exponential model for the conditional probability $P(y|x, \theta)$, where x is a set of features and θ is a set of parameters, using the CRF formulation as follows:

$$P(y|\mathbf{x}, \theta) = \sum_{\mathbf{h}} P(y, \mathbf{h}|\mathbf{x}, \theta) \tag{3.31}$$

$$= \sum_{\mathbf{h}} \frac{1}{Z} exp\Big(\sum_{j=1}^{K} \big(r_j^m \theta^n(h_j^n) + r_j^s \theta^n(h_{K+j}^n) \big) + \sum_{j=1}^{K} r_j^m \theta^m(h_j^m)$$

$$+ \sum_{j=1}^{K} r_j^e \theta^e(h_j^e) + \sum_{j=1}^{K} r_j^s \theta^s(h_j^s) + \sum_{j=2}^{2K} \theta^{nn}(y, h_{j-1}^n, h_j^n)$$

$$+ \sum_{j=2}^{K} \theta^{mm}(y, h_{j-1}^m, h_j^m) + \sum_{j=2}^{K} \theta^{ee}(y, h_{j-1}^e, h_j^e) + \sum_{j=2}^{K} \theta^{ss}(y, h_{j-1}^s, h_j^s)$$

$$+ \sum_{j=1}^{2K} \theta^{ny}(y, h_j^n) + \sum_{j=1}^{K} \theta^{my}(y, h_j^m) + \sum_{j=1}^{K} \theta^{ey}(y, h_j^e) + \sum_{j=1}^{K} \theta^{sy}(y, h_j^s) \Big)$$

where Z is a partition function. In this formulation, we define the state function as the radius of a cell and the transition function as the identity function.

In training phase, we maximize the regularized log-likelihood of the entire training samples $\{(\mathbf{x_i}, y_i)\}$ to find the best parameter θ. More formally,

$$\theta^* = \arg\max_{\theta} L(\theta) = \sum_{i=1}^{n} \log P(y_i|\mathbf{x_i}, \theta) - \frac{1}{2\sigma^2}||\theta||^2 \tag{3.32}$$

where σ is the variance of a Gaussian prior.

In testing phase, for each mitosis candidate sequence $\mathbf{x}$, we first compute $P(y = 1|\mathbf{x}, \theta^*)$. If this is greater than 0.5, then we regard that a birth event occurs at the frame when the newborn cell is first detected. Otherwise, we regard that a birth event does not occur. We refer to the related previous work[109] and Sections 3.1.2 and 3.2.3 for detailed learning and inference processes.

3.3.2 Experiments

Cell Type: Hematopoietic stem cells (HSCs) are blood-forming stem cells and give rise to all blood cell types in the body for cell replacement therapy. In the last decades, the regenerative capacity of HSCs has been utilized to treat bone marrow failure as well as rescue blood function for hematopoietic disorders (e.g., sickle cell anemia, leukemia, lymphoma, immune deficiency disorders, and autoimmune diseases) by transplantation of HSCs into patients [83, 88]. However, HSC therapy is limited by the low cell dose available for transplantation as well as the lack of knowledge on how to expand HSCs *ex vivo* without loss of its regenerative capacity [62, 111]. As such, it is essential to establish the lineage relationships between HSCs and their progeny within a population of HSCs. The lineage relationships can provide information on how mechanisms controlling self-renewal and proliferation can be altered in response to the addition of exogenous biochemical signals during *in vitro* culture to facilitate the study and *ex vivo* expansion of HSCs.

Cell Culture and Imaging: Bone marrow CD34+ HSCs (Stem Cell Technologies, Vancouver, BC, Canada) were cultured in serum-free expansion media with Stem Span Cocktail CC100 (Stem Cell Technologies, Vancouver, BC, Canada) at 37°C, 5% CO_2. The cells were seeded in microwells at a density of 1-5 cells/well. HSCs were imaged every 30 seconds over the course of 4 days using a Carl Zeiss Axiovert 200M equipped with a EC-Plan Neofluar 5X phase objective (Carl Zeiss Microimaging, Thornwood, NY), resulting in 11520 images. Each image contains 1388×1040 pixels, capturing 14 HSC populations in 3×5 array of microwells as no cell was seeded in one of the wells.

Ground Truth Acquisition: We manually annotated the time and location that mitosis is completed. More specifically, when the boundary between two newborn cells clearly appear, we marked the contacting point of the two cells, observing 117 mitotic events in total.

Evaluation: We consider a detection a true positive if a contacting point of two newborn cells is detected within spatially 5 pixels and temporally 10 frames (5 min) from a manually annotated mitosis. If the same mitosis is detected more than once, only one detection is considered true positive, the others false positives.

3.3.3   Results and Discussions

In the candidate detection step, 234 mitosis candidates were detected. Among the 117 mitosis annotated, 114 mitosis were captured by the candidates but the other three mitosis were missed. One mitosis was not captured because the mitotic cell overlaps another cell during the mitosis process (Figure 3.24(a)). The other two were detected, but temporally beyond the threshold (10 frames), and thus considered missed. In these cases, one of the newborn cells stick to the boundary of the well where a cell often does not show bright and circular appearance, and thus it was not detected as a new born until the cell becomes circular and bright (Figure 3.24(b)).

In the candidate validation step, 116 candidates were determined to be mitosis. Among them, 113 cases were true positives. Therefore, overall 97.4% precision and 96.6% recall were achieved for mitosis detection. F-measure and AUC (Area under PR-curve) were 97.0% and 98.9%, respectively. PR-curve was plotted by varying the decision probability for the conditional probability $P(y|x, \theta)$, which is originally 0.5, from 0 to 1. Figure 3.24 demonstrates some true positive, false positive, and false negative cases. Detected birth events tend to precede their corresponding manual annotation by a few frames since a newly appeared cell is detected before the cell boundary is clearly shown.
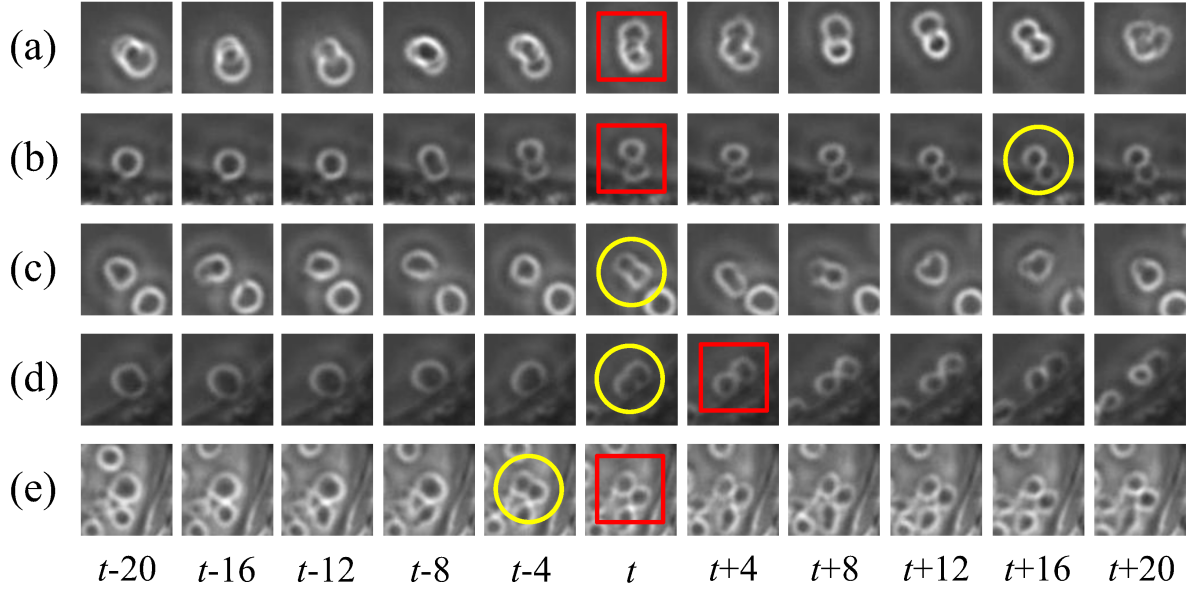
Figure 3.24: Examples of mitosis detection results in non-adherent cell populations. Yellow circles enclose detected birth events, while red boxes surround manually labeled birth events. (a) False negative case: as the mitotic cell overlaps another cell, new born cells were not detected. (b) Another false negative case: since one newborn cell in contact with the well boundary does not look like a cell right after mitosis, mitosis was detected more than 10 frames later when the cell is detected as a newly appeared cell, and thus the mitosis was consdered missed. (c) False positive case: as the cell elongates, it looks like two daughter cells, and was thus misdetected as a mitotic cell. (d) True positive case: though the mitosis occurs in contact with the well boundary, it was correctly detected. (e) Another true positive case: the mitosis was correctly detected although it was surrounded by several other cells.

3.4   Summary of Mitosis Detection

We have proposed methods that can detect birth events, the time and location at which cell division is completed, in both adherent and non-adherent cell populations. To detect birth events, we came up with a framework that consists of three steps: candidate detection, temporal information incorporation, and candidate validation. For adherent cells, we modeled morphological and brightness changes during mitosis process for the candidate validation, while for non-adherent cells, we examined size change of potential mother and daughter cells over time along with their trajectories.

Our contribution to mitosis detection can be summarized as follows:

69

- Mitosis detection accuracy was significantly enhanced compared to previous work by developing efficient candidate extraction schemes and probabilistic models for event detection, namely Event Detection CRF (EDCRF) and Two-Labeled HCRF (TL-HCRF).

- Mitosis detection speed was also considerably improved compared to previous work by bypassing the use of time consuming modules, such as preconditioning [71], and adopting a cascade scheme for mitosis candidate detection. We empirically showed that mitosis detection can be performed in real-time manner with our methods.

- Mitosis detection was performed on wound healing assays with high cell confluence and different culture conditions, which shows the potential use of the method for real biological or biomedical applications in near future.

Chapter 4

Apoptosis Detection

In this chapter, we present automated apoptosis detection methods in time-lapse phase contrast microscopy. Along with mitosis detection, apoptosis detection enables a monitoring of cell growth and is thus important to find the optimal condition for cell proliferation or cell growth inhibition.

One may think that apoptosis detection can be performed by the same methods for mitosis detection, such as the methods we introduced in the previous chapter. However, such methods are not effective because mitosis detection depends on a unique visual presentation lasting only a short time, namely a figure eight shape, while apoptosis does not involve such a distinctive visual hallmark. In addition, after a cell dies through apoptosis, the dead cell often forms a cluster with other cells or the apoptotic bodies stick together into a cell shape, which makes apoptosis detection more difficult than mitosis detection.

We define *death event* as the time and location at which an apoptosis process is the most noticeable. Specifically, for adherent cells, death event is defined as the initiation of apoptosis, which shows the most prominent visual change due to size shrinkage and brightness increase. On the other hand, for non-adherent cells, death event is defined as the completion of apoptosis. Since non-adherent cells do not show change in size or brightness during apoptosis, the station-ary state of a (dead) cell, which indicates apoptosis completion, is the most distinctive cue for

71
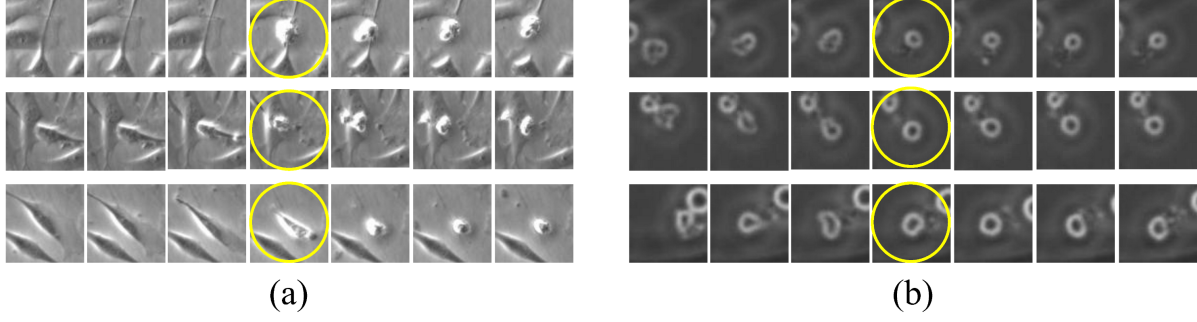
Figure 4.1: Examples of death events in phase contrast microscopy. Yellow circles enclose death events, the location and time in which apoptosis initiates for adherent cells and apoptosis is completed for non-adherent cells. A typical death event of adherent cells begins with cell shrinkage and increased brightness, while a common death event of non-adherent cells ends with a stationary state of a cell.

apoptosis detection. Figure 4.1 demonstrates typical death events in adherent cell populations (Figure 4.1(a)) and non-adherent cell populations (Figure 4.1(b)).

The objective of apoptosis detection is to know when (in which frame) and where (at which x and y positions) death events occur. In order to achieve this goal, we propose two different methods, one for adherent cells and the other for non-adherent cells. For adherent cells, we adopt the same framework that was proposed for mitosis detection, which consists of three steps: detection of candidates, incorporation of temporal information, and validation of the candidates. For the candidate detection, we come up with a phase contrast microscopy image formulation model, based on which the change from a stretched dark cell to a shrunken bright cell is detected as candidates. For non-adherent cells, we first construct cell tracklets, which are fragments of cell trajectory. Then, each tracklet is examined whether it shows a transition from a living cell to a dead cell using a semi-supervised learning framework.

In Sections 4.1 and 4.2, we present apoptosis detection methods for adherent cell populations and non-adherent cell populations, respectively. We summarize this chapter in Section 4.3.

72
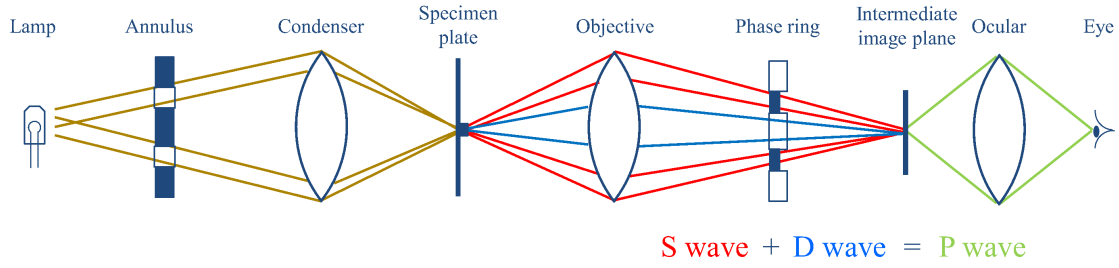
S wave + D wave = P wave

Figure 4.2: Image formulation process in a phase contrast microscope. The surround wave (S wave), which does not interact with the specimen, and the diffracted wave (D wave), which is scattered by the specimen, undergo interference, resulting in a resultant particle wave (P wave).

4.1 Apoptosis Detection for Adherent Cells

In this section, we present a method to detect death events in time-lapse phase contrast microscopy, particularly for adherent cells, which involves changes in cell morphology and image intensity during apoptosis [55]. The method first detects the cells that shrink and become bright as candidates for apoptotic cells in order to reduce the search space. For this candidate detection, we propose a computational model of phase contrast microscopy that can be used to detect both bright and dark cells. Each candidate is examined to determine if apoptosis indeed occurs based on changes in image intensity and texture over the neighboring frames. The proposed method was tested on three time-lapse microscopy image sequences of C2C12 myoblastic stem cells, which consist of more than 1500 image frames and contain more than 1000 apoptotic events in total.

4.1.1 Phase Contrast Image Formulation Model

To detect death event candidates, we first detect both bright and dark cell areas using a computational model for the optical principle of phase contrast microscopy. In this section, we introduce a phase contrast image formulation model and generalize it for bright and dark cell area detection.

Recently, Yin et al. [133] proposed a method that models the image formation process of

phase contrast microscope to restore phase retardation caused by cells. The phase contrast micro-scope converts the phase difference in light passing through the transparent specimen to bright-ness changes in the image [91]. As shown in Figure 4.2, the wavefront of the illuminating beam is divided into two components after passing through the specimen. The primary component is the surround wave (S wave) that passes through or around the specimen without interacting with it. The other component is the diffracted wave (D wave) that is scattered by the specimen. These two waves undergo interference and produce a resultant particle wave (P wave). The phase con-trast microscopy technique advances S wave by a quarter wavelength as well as attenuates it in order to maximize the affect of D wave on P wave. As a result, even a transparent specimen is visible in phase contrast microscopy since D wave scattered by the specimen noticeably change the resultant P wave.

In [133], the surround wave l_S and the diffracted wave l_D are derived as

$$l_S = i\zeta_p A e^{i\beta} \tag{4.1}$$

$$l_D = \zeta_c A e^{i(\beta+\theta(x))} + (i\zeta_p - 1)\zeta_c A e^{i(\beta+\theta(x))} * airy(r) \tag{4.2}$$

where $i^2 = -1$; A and β are the illuminating wave's amplitude and phase before hitting the specimen plate, respectively; ζ_p and ζ_c are the amplitude attenuation factors by the phase ring and the specimen, respectively; $\theta(x)$ is the phase shift caused by the specimen at location x; and, $airy(r)$ is an obscured Airy pattern (diffraction pattern with a bright region in the center surrounded by a series of concentric dark and bright rings). The particle wave l_P is calculated as

$$l_P = l_S + l_D. \tag{4.3}$$

74

The intensity of the final observed image g is then computed as

$$g = |l_P|^2 \tag{4.4}$$

$$= |l_S + l_D|^2 \tag{4.5}$$

$$= |i\zeta_p A e^{i\beta} + \zeta_c A e^{i(\beta+\theta(x))} + (i\zeta_p - 1)\zeta_c A e^{i(\beta+\theta(x))} * airy(r)|^2 \tag{4.6}$$

$$\approx 2\zeta_c\zeta_p(1+\zeta_c)A^2\left(\frac{\zeta_p(1+\zeta_c)}{2\zeta_c} + \theta(x) - \theta(x) * airy(r)\right) \tag{4.7}$$

$$\propto \theta(x) * (\delta(r) - airy(r)) + C \tag{4.8}$$

where $C = \frac{\zeta_p(1+\zeta_c)}{2\zeta_c}$ is a constant. Based on this approximate linear relation between $\theta(x)$ and g in Eq. (4.8), $\theta(x)$ can be reconstructed from g. Since $\theta(x)$ is the phase shift caused by the specimen, thresholding $\theta(x)$ results in the detection of cell areas [133].

Note that in order to obtain Eq. (4.7) from Eq. (4.6), it is assumed that $\theta(x)$ is close to zero, based on which following three approximations are applied:

$$e^{i\theta(x)} \approx 1 + i\theta(x), \quad \theta(x)^2 \approx 0, \quad (\theta(x) * airy(r))^2 \approx 0. \tag{4.9}$$

However, these approximations are not valid particularly for bright cells, which are thicker and thus cause greater phase retardations than dark cells.[1] Even for the detection of dark cells, the assumption $\theta(x) \approx 0$ may not be valid because the diffracted wave is retarded in phase by approximately 90 degrees through interaction with the specimen [92]. As a result, the method has difficulty in detecting mitotic or apoptotic cells, which appear bright due to their increased thickness.

To detect bright cells (and also dark cells more properly), we generalize the model by assuming that $\theta(x)$ is close to a certain phase ϕ, which is not necessarily zero. More formally, $\theta(x)$ is

[1] the phase retardation θ cause by a cell is known proportional to the thickness of the cell. More formally, the phase retardation ϕ is calculated as

$$\theta = \frac{2\pi}{\lambda}(n_1 - n_2)t, \tag{4.10}$$

where λ denotes the wavelength of the incident light; t is the thickness of the cell; and n_1 and n_2 denote the refractive indices of the cell and medium, respectively.

replaced with $\phi + \tilde{\theta}(x)$, where ϕ is a constant and $\tilde{\theta}(x)$ is close to zero. Based on this relaxed assumption, g is computed as

$$g = |l_S + l_D|^2 \tag{4.11}$$

$$= |i\zeta_p A e^{i\beta} + \zeta_c A e^{i(\beta+\phi+\tilde{\theta}(x))} + (i\zeta_p - 1)\zeta_c A e^{i(\beta+\phi+\tilde{\theta}(x))} * airy(r)|^2$$

to which we apply the following approximations

$$e^{i\tilde{\theta}(x)} \approx 1 + i\tilde{\theta}(x), \quad \tilde{\theta}(x)^2 \approx 0, \quad (\tilde{\theta}(x) * airy(r))^2 \approx 0, \tag{4.12}$$

resulting in

$$g \approx 2\zeta_c\zeta_p(\cos\phi + \zeta_c)A^2$$

$$\times \left(\frac{\zeta_p(1 + \zeta_c^2 + 2\zeta_c \cos\phi)}{2\zeta_c(\cos\phi + \zeta_c)} + \tilde{\theta}(x) - \frac{\cos\phi + \zeta_c + \zeta_p \sin\phi}{\cos\phi + \zeta_c}\tilde{\theta}(x) * airy(r) \right) \tag{4.13}$$

$$\propto \tilde{\theta}(x) * (\delta(r) - B \cdot airy(r)) + C' \tag{4.14}$$

where $B = \frac{\cos\phi + \zeta_c + \zeta_p \sin\phi}{\cos\phi + \zeta_c}$ and $C' = \frac{\zeta_p(1+\zeta_c^2+2\zeta_c \cos\phi)}{2\zeta_c(\cos\phi+\zeta_c)}$. Note that, if $\phi = 0$, then $\tilde{\theta}(x) = \theta(x)$, $B = 1$, and $C' = C$; thus, Eq (4.14) reduces to Eq (4.8). Since this is also a linear relation between $\tilde{\theta}(x)$ and g, $\tilde{\theta}(x)$ can be reconstructed from g and cell areas can be detected by thresholding $\tilde{\theta}(x)$.

4.1.2 Algorithm

To narrow down the locations where apoptosis begins, we first locate bright cells whose formation is followed by size shrinkage and brightness increase. Each bright cell is then validated based on temporal changes in brightness and texture to find death event candidates.

Death event candidate detection: Using the model introduced in the previous section, we detect bright and dark cell areas, separately with two different parameters: ϕ_b and ϕ_d. For the parameter setting, we tested several values $(0, \pi/6, \cdots, 11\pi/6)$ and selected the best ones based on death event detection accuracy on the training set. (This can also be conducted by visual examination on a first few images.) The proposed model can detect bright cells as well as dark
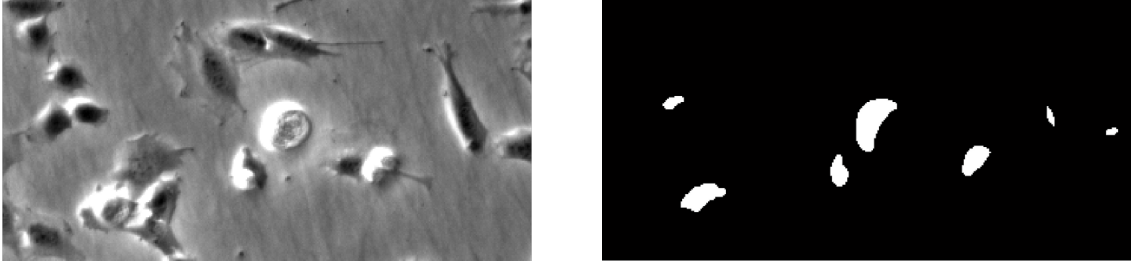
Figure 4.3: A sample image and bright cell areas on it detected by the proposed model.
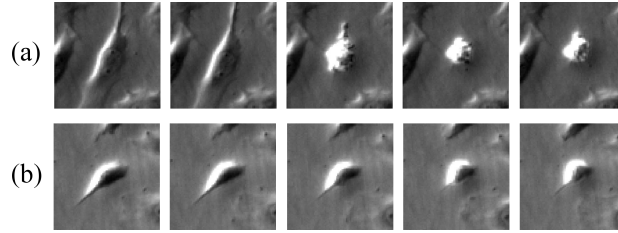
Figure 4.4: Apoptosis examples in consecutive frames. An apoptotic cell shrinks and its brightness increases (a) abruptly for a short time period (less than five minutes) or (b) gradually for a long time period (tens of minutes or a few hours).

cells, unlike the previous model. Figure 4.3 shows bright cell areas detected by our model, where bright halos are undetected or weakly detected.

To detect the cells that undergo the beginning of an apoptotic process, we examine each bright cell area to determine if its formation is followed by the decrease of dark area and/or the increase of bright area, which represent cell shrinkage and brightness increase, respectively. If the change is not trivial, the bright cell area is considered a candidate for an apoptotic cell; otherwise, it is regarded an already dead cell or a bright halo, and thus is not further taken into account.

More formally, for each bright cell area at frame t, we examine its neighboring region over consecutive frames prior to the frame t. If the proportion of the bright area expanded or dark area shrunk in the region to the region's area is greater than a certain threshold, then the bright cell area is considered a candidate for an apoptotic cell. As the duration of cell shrinking and brightness change varies (See Figure 4.4.) and the image acquisition interval can also be different among experiments, we investigate different numbers of frames (up to K frames) prior to frame
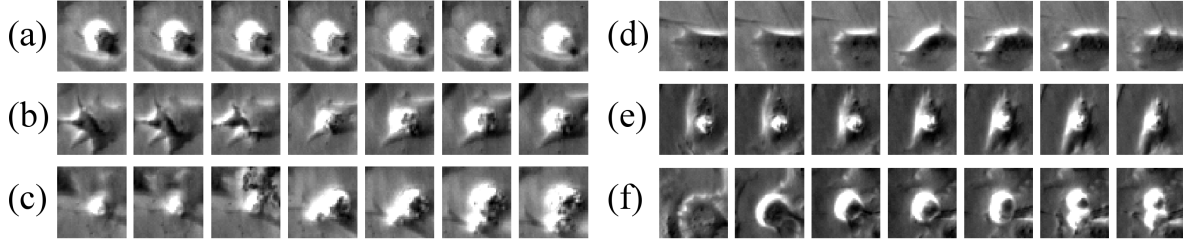
Figure 4.5: Candidate patch sequences containing apoptosis (left) and non-apoptosis (right): (a-c) apoptotic cells in contact with none, a living cell, and a (or a group of) dead cell(s); (d-f) a change of halo, a (or a group of) dead cell(s), and mitosis.

t. More specifically, if the change between every two consecutive frames among the $k + 1$ preceding frames is greater than the reduced threshold th/k for any $k \in \{1, \cdots, K\}$, then the bright cell area is considered a candidate for an apoptotic cell. The detailed procedure of death event candidate detection is described in Algorithm 1.

The neighboring region is set to be a circle with radius R. Hence, this scheme involves three parameters: K, R, and th. We set these parameters to achieve at least a certain high level of recall (e.g., 99%) and as high a precision as possible in candidate detection among the training data (Note that as th decreases, recall increases while precision decreases.). K and R can also be determined based on the observation of apoptosis duration and cell size/movement, respectively. In our experiments, K, R, and th were set to be 5, 10, and 0.25, respectively.

Incorporation of Temporal information by Tracking: Each candidate is tracked in the neighboring frames in order to incorporate temporal information by using a standard correlation tracking method, resulting in candidate patch sequences as shown in Figure 4.5. Investigating temporal information helps to avoid detecting mitosis, which shows similar visual change to apoptosis at the beginning, as well as bright halos and dead cells. This step involves two parameters, the size of patch and the number of frames tracked on one side (preceding or following a candidate), which can be set by a typical validation scheme. In our experiments, they were set to be 50 pixels and 3 patches. From each patch in a patch sequence, we extract the following features:

Algorithm 1 Apoptosis candidate detection at frame t

Input: $\{B^{(s)}, D^{(s)}$: binary images indicating bright/dark cell areas at frame $s\}$,

K: maximum number of frames investigated prior to the frame t,

R: radius of the neighboring region, th: threshold for bright/dark area change.

Output: $\{(cx, cy)\}$: a set of (x,y) positions of candidate apoptotic cells.

1: // Compute dark/bright area change over consecutive frames prior to frame t

2: **for** $k = 1 \rightarrow K$ **do**

3:    $\Delta B_k \leftarrow (B^{(t-k+1)} - B^{(t-k)})$ filtered by the average disk filter with radius R.

4:    $\Delta D_k \leftarrow (D^{(t-k)} - D^{(t-k+1)})$ filtered by the average disk filter with radius R.

5: **end for**

6: // Examine bright/dark area change.

7: $\{C_i\} \leftarrow$ a set of bright cell areas (lists of positions) at frame t, obtained from $B^{(t)}$.

8: **for** each $C_i = \{(x_j, y_j)\}$ **do**

9:    $found \leftarrow false, k \leftarrow 0$

10:    **while** not $found$ and $k < K$ **do**

11:       $k \leftarrow k + 1$

12:       **if** $\exists (x, y) \in C_i$ s.t. $\forall j \in \{1, \cdots, k\}, \Delta B_j(x, y) > th/k$ or $\Delta D_j(x, y) > th/k$ **then**

13:          $found \leftarrow true$

14:       **end if**

15:    **end while**

16:    **if** $found$ **then**

17:       // Keep the point that shows the most brightness change over the k frames.

18:       $\{(cx, cy)\} \leftarrow \{(cx, cy)\} \cup \arg\max_{(x,y) \in C_i} \sum_{k'=1}^{k} \Delta B_{k'}(x, y)$

19:    **end if**

20: **end for**
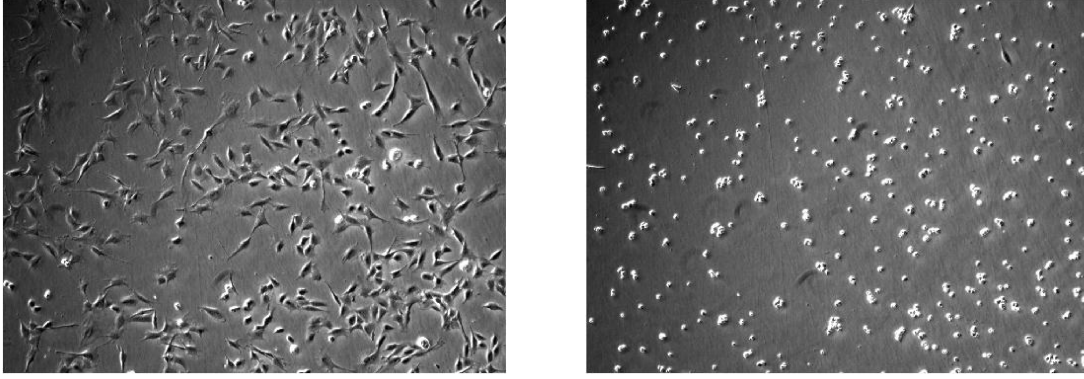
Figure 4.6: The first (left) and last (right) frames of the data.

- Brightness change histogram binning to 16 bins,

- Rotation invariant uniform local binary pattern (LBP^{riu2}) [97].

The former, which is computed on the difference between a patch and its previous patch, captures brightness change over time, the major cue for apoptosis detection, more precisely and in more detail than the candidate detection step. The latter captures the texture property of apoptotic cells, which is quite different from that of non-apoptotic cells as apoptosis involves membrane blebbing and the formation of apoptotic bodies. It is worth mentioning that these features are robust to global illumination change due to experimental setting.

Candidate Validation: We applied a linear Support Vector Machine (SVM) to classify candidate patch sequences. We tested several other classifiers used for temporal modeling, particularly models used for mitosis detection, namely HCRF [109], EDCRF, and TL-HCRF. All these classifiers as well as an RBF kernel SVM did not outperform a linear SVM despite their higher computational cost, presumably because visual features of apoptosis are less informative and more noisy in the sense that apoptosis does not involve distinctive morphological features, such as a figure eight shape during mitosis. Under such a circumstance, a max-margin classifier with a simple decision boundary might be more effective to eliminate outliers or meaningless patterns. After classification, the post-processing in [52] is conducted to prevent one apoptosis from being detected multiple times.
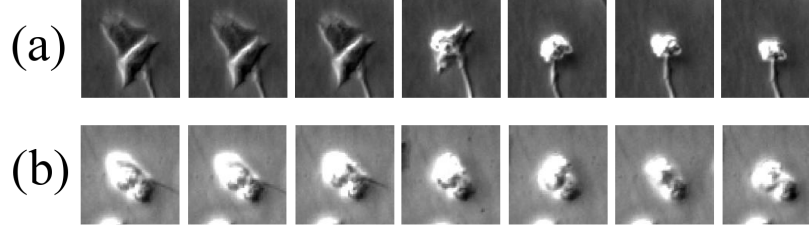
Figure 4.7: Examples of undetected apoptosis after candidate validation. (a) As two cells in contact with each other undergo apoptosis simultaneously, only one apoptosis is detected. (b) An apoptotic cell is barely observable as it is covered with two dead cells.

4.1.3 Experiments

We introduce the experimental setup and results with discussions.

Image and Ground Truth Acquisition: After C2C12 myoblastic stem cells were cultured for one day, Mitomycin C was added to induce apoptosis. Afterward, three populations were imaged every 5 minutes over 45 hours, resulting in three sets of 540 image frames. As shown in Figure 4.6, most of cells were dead at the last frame. We manually annotated apoptosis by marking the center of each apoptotic cell after it shrinks and becomes bright, obtaining 1154 cases in total. The image sequences and ground truths are available on the author's web page (www.cs.cmu.edu/∼seungilh).

Evaluation: A detection is considered a true positive if an apoptotic cell is detected within spatially 30 pixels and temporally 3 frames from an annotated location. If an apoptotic cell is detected more than once, the only one that temporally the closest to the ground truth was considered true positive, the others false positives. The apoptosis closely located to the image boundary (within 25 pixels, which is the half of the patch size) were not taken into account for evaluation.

We used one sequence as a training set and another one as a test set, testing all six training-testing set pairs. We set all the parameters including the SVM parameter through a four-fold cross validation on the training set.
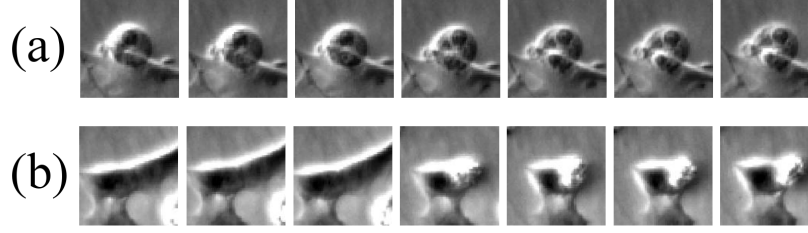
Figure 4.8: Examples of undetected apoptosis at the candidate detection step. (a) Apoptosis occurs without brightness change. (b) As a small apoptotic cell is located in contact with a compact and dark cell, the bright apoptotic cell is considered the bright halo of the dark cell and thus not detected at the bright cell area detection step.

4.1.4   Results and Discussions

Our method achieved an average precision of 93.0%±1.1% and an average recall of 89.8%±1.4% for apoptosis detection. False positives mostly happened due to rapidly changing halos and moving dead cells attached to living cells. Duplicate detection sometimes occurred as apoptotic cells abruptly and considerably move while they shrink or when cell internal contents spill out. False negatives mostly happened when cells form a cluster in which multiple apoptosis simultaneously occur or apoptotic cells are occluded by other cells, as shown in Figure 4.7.

In the candidate detection step, our method detected almost all apoptosis except a few cases (See Figure 4.8.). The number of candidates were approximately three times as many as the number of apoptosis.

Our model-based cell area detection is effective, particularly when cell density is high and thus cells are in contact with one another and halos appear among them. The scheme outperformed a cell area detection scheme based on intensity thresholding by 3.3% and 10.3% in terms of average apoptosis detection precision and recall, respectively, on the last 100 frames of the three sequences.

4.2   Apoptosis Detection for Non-adherent Cells

In this section, we propose a method for detecting apoptosis in a population of non-adherent cells, which float or are suspended freely in the culture medium, in contrast to adherent cells, which are attached to a petri dish. The method first detects cell regions and tracks them over time, resulting in the construction of cell tracklets. For each of the tracklets, we compute visual properties of the cell and examine whether they show a transition from a live cell to a dead cell in order to determine the occurrence and timing of death events. For the validation, we adopt a transductive learning framework to utilize unlabeled data in addition to labeled data. We evaluate our method on hematopoietic stem cell (HSC) populations, which are currently in clinical use for rescuing hematopoietic function during bone marrow transplants.

4.2.1   Death event of non-adherent cells

Apoptosis of non-adherent cells do not involve neither distinctive visual hall marks, such as a figure eight shape shown in the mitotic process, nor evident cell shrinking and brightness change shown in the apoptotic process of adherent cells. In this section, we describe visual characteristics of apoptosis of non-adherent cells to provide a better understanding of the given task.

The process of apoptosis includes cell shrinking, membrane blebbing, DNA degradation, and the formation of apoptotic bodies. Therefore, it is often visually characterized by irregular cell shape and outline, as shown in Figure 4.9(a,b), as blebs are formed and the contents of the cell spill out. Sometimes, cell is dying with its boundary becoming weaker without cell shape change, as shown in Figure 4.9(c,d). Since there are a number of apoptotic stimulus sources, the cell dying process is not uniquely characterized, but shows various visual presentations and takes different amount time from a few minutes to several hours. After a death event, cell fragments often get sticky and form a cluster, becoming a circular shape again, the size of which is commonly smaller than it was alive, as shown in Figure 4.9(b). In addition to cell appearance, cell
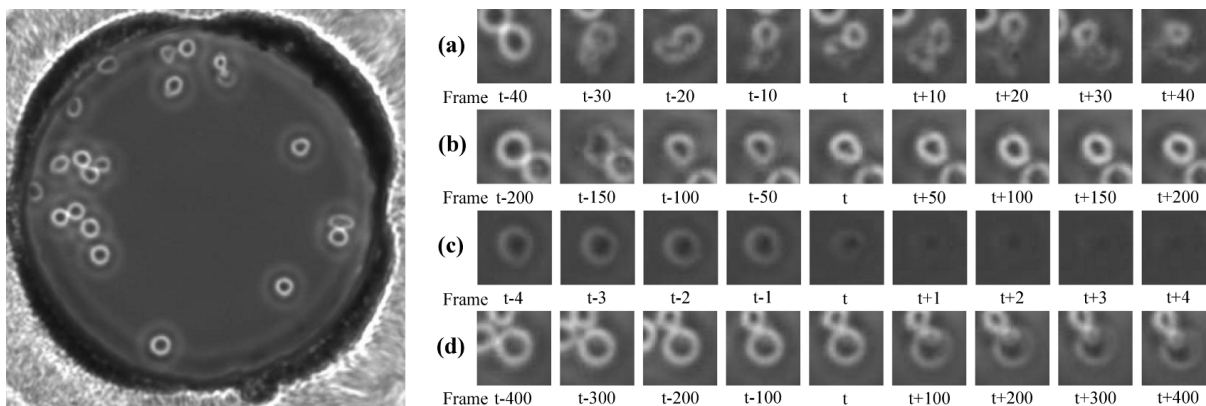
Figure 4.9: Sample image frame from the data (left) and patch sequences containing a death event (right). (a,b) Apoptosis, programmed cell dying process, begins with a death event. During apoptosis, the contents of a dying cell leak out and the plasma membrane of the cell becomes irregular and non-circular as cell blebbing occurs. After a cell dies, cell debris often sticks to one another, forming a circular shape which is generally smaller than it was alive. (c,d) Cells are dying without shape change. The cell boundaries get fainter for several to hundreds frames until they finally disappear. For these candidate sequences, death events are manually marked at frame t with the assistance of a biologist.

movement plays a key role for identifying apoptosis as dead cells do not move without external force.

A major difficulty of cell death event detection is that apoptotic process is not quite visually distinctive. Live cells occasionally show irregular shape and outline, and thus are often confused with dying cells. In addition, live and dead cells are sometimes not distinghishable based on short-term observation due to their similar appearance and behavior. Live cells sometimes appear dark looking like dead cells as they elogate or are in contact with the microwell boundary, and do not move for a long time like dead cells. On the other hand, dead cells often show a circular shape and bright boundary after apoptotic bodies stick together, being confused as if they are alive, and occasionally move along with the culture medium or as being pushed by their neighboring live cells.
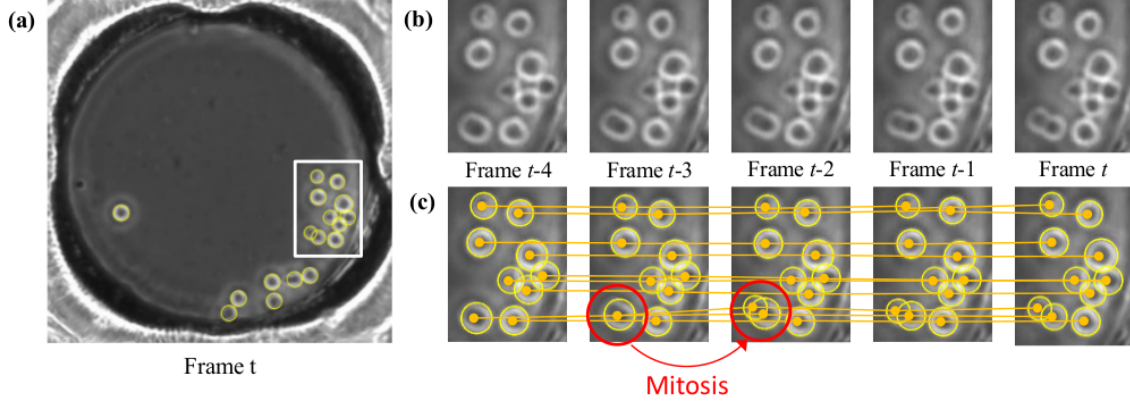
Figure 4.10: Tracklet generation for apoptosis detection. (a) A sample image frame where cells are detected using a set of ring filters. (b) Original image sequence of the boxed area extracted from a series of consecutive frames. (c) Cell tracking results generated by frame-by-frame association. During tracking, mitosis is also detected as marked by red circles.

4.2.2 Algorithm

Since apoptosis of non-adherent cells is not visually distinctive, we detect a death event for non-adherent cells by tracing the change of the visual property of a cell in a long-time period. Note that, on the other hand, mitosis detection for adherent/non-adherent cells and apoptosis detection for adherent cells are performed by recognizing the mitotic or apoptosis process, which lasts for a relatively short-time period. More specifically, we model tracklets of a live cell and a dead cell and search for a transition from a live cell to a dead cell to find a death event. Another distinctive feature of the proposed apoptosis detection algorithm is to use unlabeled information in addition to labeled information. This semi-supervised learning approach improves the detection accuracy as well as reduces efforts of manual labeling. Based on these main ideas, we propose a method consisting of three steps: tracklet generation, feature extraction, and validation.

Tracklet generation: We first track cells based on frame-by-frame association and detect mitosis by examining cell size change over time, using the method introduced in Section 3.3.1, as illustrated in Figure 4.10. The goal of this step is to obtain tracklets, each of which is a fragment of a cell trajectory and less likely to be prone to error as an existing tracket terminates and a new
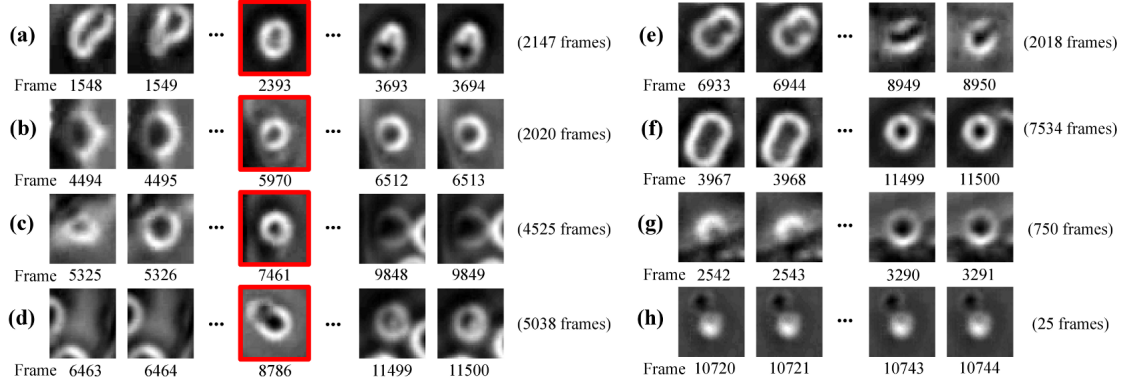
Figure 4.11: Sample trackets (a-d) that contain a death event and (e-h) that do not contain a death event. The center patches in sequences (a)-(d) enclosed by a red box include a death event annotated by human. Trackets consist of a varying number of patches, from tens to thousands.

tracket is initiated whenever the confidence of frame-by-frame assocication is low. Fig. 4.11 shows examples of cell trackets.

It is worth mentioning that candidate patch sequences may not perfectly capture the entire history of individual cells, from birth or the initial frame to disappearance or the last frame, due to the errors of cell region detection and tracking. For example, patches sometimes include non-cell objects, such as bright background as can be seen in the initial frames in Fig. 4.11(d). In addition, candidate sequences often begin with the cells that are not in the first frame nor newborn cells as shown in Fig. 4.11(a-d) and (g-h); as a cell is lost during tracking for not a short time period, a new track initiates for the cell when it is found later. These errors can be compensated for to some extent as we more concern about the overall pattern change than the details of a small number of patches.

Feature extraction: Visual characteristics of death events aforementioned lead to a conclusion that observing cell property change over a long time period is required to effectively identify a death event. In order to capture a long-time cell property change, we extract high-level properties on cell appearance and movement based on the visual characteristics of death events and dead cells as follows:

- cell radius

- cell roundness

- displacement from the previous position

- whether being in contact with another cell

The first two features are computed based on the cell region detection result and the other features based on the cell tracking result. The last feature is used to measure the possibility of a cell's shape or movement being affected by neighboring cells.

As a result of feature extraction from each tracklet, we obtain a time series of feature vectors where the length of the time series is the same as the number of patches in the tracklet and each feature vector consists of the four cell properties. To obtain the same size of features from all tracklets, we resize each time series into a certain length S by averaging features from consecutive patches or interpolating features of between-patches. The feature vectors of each resized time series are then concatenated into a feature vector. In our experiments, S was selected among $\{10, 30, 50, 100, 200, 300\}$ to maximize F-measure in a validation set.

Tracket validation: We adopt a learning-based method for the validation of tracklets; in other words, given the manual labeling on death events on a set of trainging image sequences, we model a statistical model to determine the occurrence and timing of death events in a set of testing image sequences.

For the validation of trackets, instead of modeling death events in trackets, we model trackets of a live cell and a dead cell. To do so, we need to convert labels on death events into labels on tracklets, since the manual annotation is given on a death event, a specified time and location, rather than a tracket. The procesure of the labeling conversion is as follow. First, since a death event by definition means a transition from a live cell to a dead cell, we divide the tracklets containing a manually annotated death event into two tracklets and label the first and second pieces as tracklets of a live and a dead cell, respectively. Second, because a dead cell cannot undergo mitosis nor divide into two daughter cells, we label a tracklet of a mother cell as a tracklet of a live cell. The remaining tracklets are assigned as tracklets of a cell that is unknown

(a) .... (b) ....

$\times$ Annotated death event $\bigcirc$ Detected mitosis $--$ Live cell tracklet $\cdots\cdots$ Dead cell tracklet $—$ Unknown tracklet
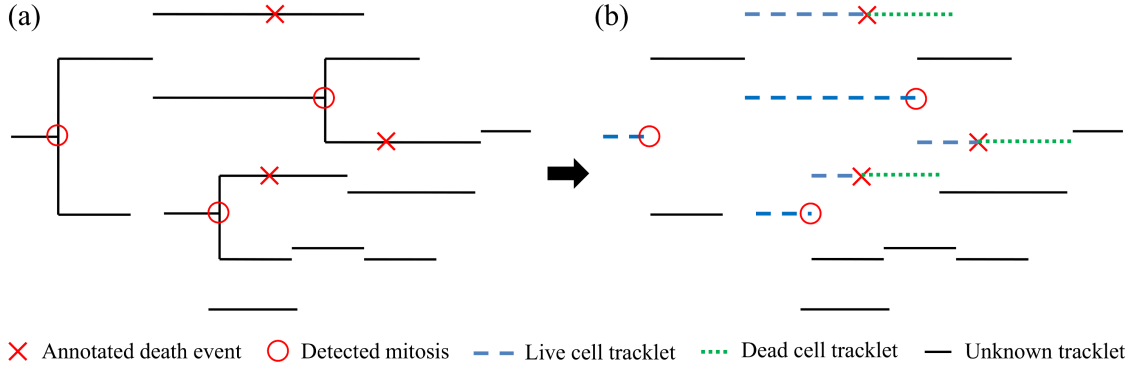
Figure 4.12: Conversion from labels on death events to labels on tracklets (a) tracking results with manually annotated death events and automatically detected mitosis (b) tracklets categorized into three types: tracklet of a live cell, tracklet of a dead cell, and tracklet of a cell unknown whether live or dead. The tracklet containing a death event is divided into two tracklets and the first and second pieces are labeled as tracklets of a live and a dead cell, respectively. The tracklet of a mother cell is labeled as a tracklet of a live cell.

whether live or dead. Figure 4.12 shows an example of the label conversion.

In order to utilize the unlabeled information in addition to the labeled information, we adopt a transductive support vector machine (TSVM) [59]. TSVMs additionally consider unlabeled data; while learning a maximum margin classifier with labeled samples like (inductive) SVMs, TSVMs simultaneously force the margin to be as much far away as possible from unlabeled samples. More formally, the optimization problem of TSVM is as follows: given a set of L labeled samples $\mathcal{L} = \{(\mathbf{x}_1, y_1), \cdots, (\mathbf{x}_L, y_L)\}, \mathbf{x} \in \mathbb{R}^{4S}, y \in \{1, -1\}$ and a set of U unlabeled samples $\mathcal{U} = \{\mathbf{x}_{L+1}, \cdots, \mathbf{x}_{L+U}\}$, TSVM minimizes

$$\frac{1}{2}||\omega||^2 + C^{(L)} \sum_{i=1}^{L} \xi_i + C^{(U)} \sum_{i=L+1}^{L+U} \xi_i \tag{4.15}$$

subject to

88

$$y_i(\omega \cdot \mathbf{x}_i + b) \geq 1 - \xi_i, \quad i = 1, \cdots, L$$

$$|\omega \cdot \mathbf{x}_i + b| \geq 1 - \xi_i, \quad i = L + 1, \cdots, L + U$$

$$\xi_i > 0, \quad i = 1, \cdots, L + U \tag{4.16}$$

where $C^{(L)}$ and $C^{(U)}$ are SVM parameters for labeled and unlabeled samples, respectively, and $\{\xi\}$ is a set of slack variables for soft margin SVM. This is a combinatorial optimization problem and thus finding the optimal solution is intractable for a large dataset. Instead, to obtain an approximate solution, we adopt a local search-based method that begins with an inductive SVM solution and keeps updating the solution by increasing the infuence of the test examples. We refer to [59] for more detailed procedure of the TSVM optimization.

In testing phase, given a time series of features of a new tracklet, we divide the time series into two pieces in every possible way and examine whether the first piece is a tracklet of a live cell and the second piece is a tracklet of a dead cell using the trained transductive SVM. If there is such a case, the tracklet is detemined to contain a death event and the death event timing is set corresponding to the best partition. Otherwise, the tracklet is considered not to contain apoptosis.

4.2.3 Experiments

After describing the experimental setup, we empirically show the effectiveness of the proposed method against other methods with discussions.

Data and Annotation: The proposed method was tested on 14 time-lapse phase contrast microscopy images, each of which consists of 11520 frames. For more detailed information on image acquisition, we refer to Section 3.3.2.

On the time-lapse images, we manually annotated death events with the assistance of a biologist. For the annotation, we first detected dead cells and investigated their tracks in reverse direction to identify the timing of the apoptosis completion based on cell appearance change and

movement. For each death event, we marked the center of the dead cell. As a result, we annotated 51 death events in total in the 14 time-lapse microscopy images.

Evaluation and Comparison: We defined a true positive as the case that a tracklet containing a death event is correctly identified, and counted the cases of true positives, false positives, and false negatives. To minimize the sampling bias, we performed a leave-one-sequence-out test; i.e., we used one sequence as a test set in turn and the others as a training set. Summing up all the results, we computed precision, recall, and F-measure, which is the harmonic mean of precision and recall. If one tracklet contains more than one death event due to erroneous tracking, all the death events except one in the tracklet were considered undetected, or false negatives.

We compared the proposed approach against a typical sliding window scheme as a baseline method, which examines a fixed length of consecutive patches in every possible location to determine whether it contains a death event. Positive samples were extracted from every tracklet containing a death event, particularly from the window, at the center of which the death event is located. Negative samples were extracted from the windows randomly located in the tracklets not containing a death event. Note that a sliding window scheme models death events, not tracklets of a live and a dead cell. For the validation of each sample, we applied (inductive) SVM since there is no unlabled data.

We also compared our transductive SVM model with inductive SVM and Hidden Conditional Random Field (HCRF) [109], which have popularly been used for event detection in time-lapse images. For these comparison, features were extracted as the same as the proposed method, i.e., from a whole tracklet rather than a slinding window, and only the staticial model was replaced.

4.2.4 Results and Discussions

In the candidate detection step, total 1056 tracklets were constructed. This number is much larger than the number of branches in the actual lineage trees because a new tracklet is initiated whenever the confidence of the association between cell regions over consecutive frames is low

Frame 9800   Frame 9900   Frame 9954   Frame 10100   Frame 11260
(missed)   (death event)
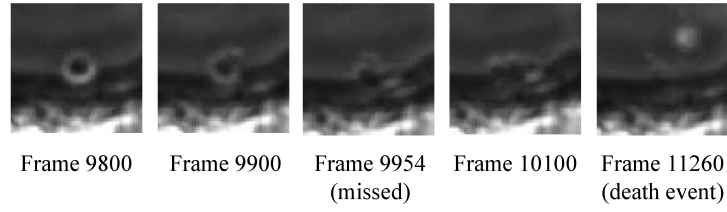
Figure 4.13: Death event undetected in cell region detection step. The dying cell was not captured because it is not bright due to the vicinity to the well boundary.

Where features are extracted from	Statistical model	Precision	Recall	F-measure
Whole tracklet	TSVM	0.792	0.731	**0.760**
Sliding window	SVM	0.824	0.528	0.644
Whole tracklet	SVM	0.805	0.635	0.710
Whole tracklet	HCRF	0.449	0.585	0.508

Table 4.1: Death event detection accuracy of the proposed method (Whole tracklet+TSVM) against other methods. Our method outperforms the methods adopting the same features with a different statistical model as well as a typical sliding window method.

for some reason, such as due to fast cell movement or undetected/misdetected cell regions. These tracklets captured 48 out of 51 death events. Two death events were missed because the dying cells were not localized in the cell region detection step as they stick to the microwell and thus do not show a bright boundary as shown in Figure 4.13. The other death event was considered missed as the tracklet containing it also contains another death event.

The proposed method achieved 79.2% precision and 73.1% recall. In terms of F-measure, it achieved 76.0% accuracy. The proposed method outperforms a typical sliding window method, which is the baseline method, by 11.6% in terms of F-measure as reported in Table 4.1. While the proposed method captures a long-term transition from a live cell to a dead cell, a sliding window method refers to only local information in the window, and thus it is not effective to detect a death event, which does not involve a short-term visual hallmark nor evident visual change between prior to and after the event.

The semi-supervised approach with TSVM outperformes (inductive) SVM or HCRF as demon-

strated in Table 4.1. Unlike SVM or HCRF, TSVM takes into account the distribution of unlabeled data, the use of which is not only helpful to improve the accuracy, but also desiable because manual labeling is time-comsuming and labor-intensive in bioimage analysis.

4.3 Summary of Apoptosis Detection

We have proposed apoptosis detection methods for adherent and non-adherent cells. For adherent cells, apoptosis candidates are detected by exploring the phase contrast microscopy image formulation process and then validated with a statistical model. For non-adherent cells, since they do not show distinctive visual hallmarks during apoptosis, we first constructed cell tracklets, which are fragments of cell trajectories, and examined each tracklet to determine whether it shows a transition from a living cell to a dead cell. For the validation, we proposed a semi-supervised framework that utilizes unlabeled information as well as labeled information.

Our contribution to apoptosis detection can be summarized as follows:

- To the best of our knowledge, apoptosis detection has not been explicitly performed with non-fluorescent microscopy. This work is the first work that develops vision-based methods for apoptosis detection in non-fluorescent microscopy.

- We generalized a phase contrast microscopy image formulation model for both bright and dark cell region detection. In addition to apoptosis candidate detection in our task, the model has great potential to be applied to other tasks, such as cell segmentation or other event detection, in phase contrast microscopy.

- We suggested a way to maximize the usage of all given information by proposing a semi-supervised learning framework for apoptosis detection. This approach is desirable for microscopy image analysis for which labeled information is often costly and cumbersome to obtain.

Chapter 5

Differentiation Detection

In this chapter, we present a supervised learning framework for differentiation detection in phase contrast microscopy [56]. Differentiaion detection helps understand the mechanism of differentiation and find the optimal condition for proliferating cells with minimizing differentiation (and thus keeping self-renewal capability) or inducing cells into a specific type of cells.

We formulate our problem as a differentiated cell region detection problem. In other words, given a series of images, we would like to locate differentiated cell area on each image. Detection is performed in a pixel-wise manner, which means that each pixel in the given image is determined whether to belong to a differentiated cell or not.

We propose a supervised learning framework for differentiation detection because cell differentiation processes vary from cell to cell. Given a training dataset of pairs of a phase contrast image and the corresponding labeled image that indicates differentiated cell regions on the phase contrast image, we learn a statistical model over the training samples, based on which differentiated cell regions are detected on a set of phase contrast images, the labels of which are not given. As the first step, we enhance the quality of phase contrast microscopy images by modeling the image formation process of a phase contrast microscope. On the improved images, we learn visual characteristics of differentiated cell regions to identify which pixels belong to differentiated cells. This framework can be applied to any type of differentiation detection as long as sample

data where differentiated cell regions are located is given. We apply the framework to muscle myotube detection and empirically show its effectiveness.

The remainder of this chapter is organized as follows. In Section 5.1, we present a phase contrast microscopy modeling and a restoration method based on the model. In Section 5.2, we revisit the microscopy model and propose diffraction pattern filtering (DPF), which shares the same idea with the restoration method, but is orders of magnitude more efficient. Using the filtering, we propose a supervised learning framework for differentiation detection and apply it to differentiation detection in C2C12 myoblastic stem cell populations. We summarize this chapter in Section 5.3.

5.1 Phase Contrast Microscopy Image Restoration

In this section, we analyze the image formation process of the phase contrast microscopy and propose an image restoration method based on the dictionary representation of diffraction patterns [121]. A major difficulty of the analysis of phase contrast microscopy images lies in properties of the images; cells under the microscopy often lack distinctive textures; and artifacts, such as bright halos, often appear when cells form a cluster or undergo a certain process. Under this circumstance, our method helps make the image analysis more reliable.

5.1.1 Phase Contrast Microscopy Image Formation Model

We revisit the previous work [133] for phase contrast microscopy modeling and briefly reintroduce the model and its notation. [1]

Phase contrast imaging can be modeled by two waves: the unaltered surround wave l_S and

[1]In Section 4.1, we reviewed this model in more detail and generalized it to detect bright cells in addition to dark cells for apoptosis candidate detection. In this section, we briefly restate its formulation and limitation in order to propose a more generalized model for general phase contrast microscopy image analysis.

the diffracted wave l_D, computed as

$$l_S = i\zeta_p A e^{i\beta} \tag{5.1}$$

$$l_D = \zeta_c A e^{i(\beta+\theta(x))} + (i\zeta_p - 1)\zeta_c A e^{i(\beta+\theta(x))} * airy(r) \tag{5.2}$$

where $i^2 = -1$; A and β are the amplitude and phase of the incident light, respectively; ζ_c and ζ_p are the amplitude attenuation factors caused by cells and phase ring, respectively; $\theta(x)$ is the phase retardation caused by the specimen at location x; and $airy(r)$ is an obscured Airy pattern, which is illustrated in Figure 5.1.1(a)).

The phase contrast microscopy image g is then formulated as the intensity of the interference of the two waves:

$$
\begin{aligned}
g &= |l_S + l_D|^2 \\
&= |i\zeta_p A e^{i\beta} + \zeta_c A e^{i(\beta+\theta(x))} + (i\zeta_p - 1)\zeta_c A e^{i(\beta+\theta(x))} \cdot airy(r)|^2 \\
&\approx 2\zeta_c\zeta_p(1+\zeta_c)A^2 \Big(\frac{\zeta_p(1+\zeta_c)}{2\zeta_c} + \theta(x) - \theta(x) * airy(r) \Big) \\
&\propto \theta(x) * (\delta(r) - airy(r)) + C
\end{aligned}
\tag{5.3}
$$

In the previous work, to obtain this linear relation between the phase contrast microscopy image and the phase retardation, the exponential term is approximated as

$$e^{i\theta(x)} \approx 1 + i\theta(x). \tag{5.4}$$

As we pointed out in Section 4.1, this approximation is valid only when the phase retardation $\theta(x)$ is close to zero. This assumption is apparently not applicable to general cases since the retardation phase $\theta(x)$, which is proportional to the thickness of cells, often vary along with different cell types and stages.

95
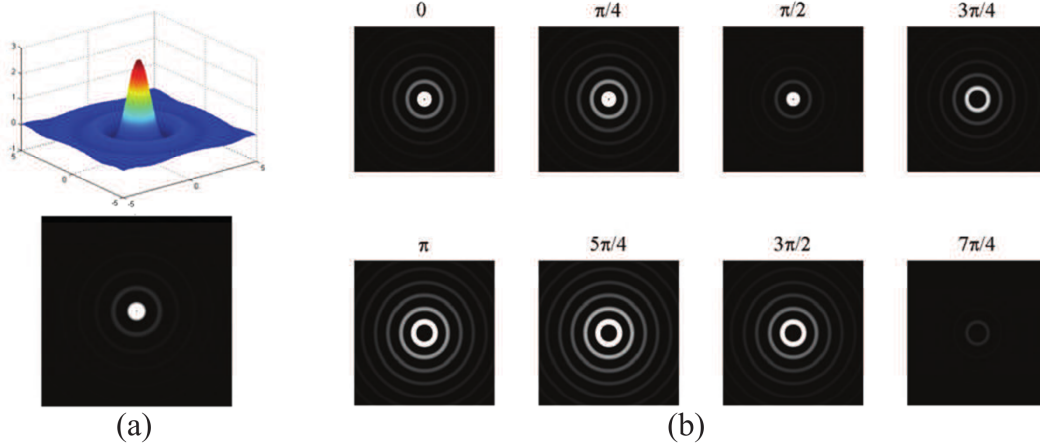
Figure 5.1: Diffraction patterns: (a) obscured Airy pattern with 3D surface view and 2D top-view; (b) diffraction patterns with different phase retardations.

5.1.2 Phase Contrast Image Model with Dictionary Representation

To address this drawback, we propose a generalized imaging model by approximating the term $e^{i\theta(x)}$ using a linear combination of $\{e^{i\theta_m}\}$:

$$e^{i\theta(x)} \approx \sum_{m=1}^{M} \psi_m(x)e^{i\theta_m}, \quad s.t. \sum_{m=1}^{M} \psi_m(x) = 1 \ \ and \ \ \psi_m(x) \geqslant 0. \tag{5.5}$$

where $\{\theta_m\} = \{0, \frac{2\pi}{M}, \cdots, \frac{2m\pi}{M}, \cdots, \frac{2(M-1)\pi}{M}\}$. We impose the nonnegative constraint because the solution would not be unique without it as $\psi_m(x)e^{i\theta_m} = -\psi_m(x)e^{i(\theta_m+\pi)}$. Moreover, the non-negative constraint removes the absolute operator of ℓ_1 norm, allowing our optimization problem to be solved in a standard manner.

The intensity of the observed image g is calculated as

$$g = |l_S + l_D|^2$$
$$= (l_S + l_D) \cdot (l_S + l_D)^*$$
$$= A^2 \left\{ \begin{array}{l} \zeta_p^2 + \zeta_c^2 - 2\zeta_c^2 * airy(r) + (\zeta_p^2 + 1)\zeta_c^2 * (airy(r) \otimes airy(r)) + \\ \zeta_p\zeta_c\big((\zeta_p - i)e^{-i\theta(x)} + (\zeta_p + i)e^{i\theta(x)}\big) * airy(r) + i\zeta_p\zeta_c(e^{-i\theta(x)} - e^{i\theta(x)}) \end{array} \right\}. \tag{5.6}$$

where $(l_S + l_D)^*$ is the conjugate of $l_S + l_D$ and $\otimes$ is element-wise matrix multiplication.

Substituting the exponential terms in Eq. (5.6) with Eq. (5.5) yields a linear representation of the observed image:

$$
g = A^2 \left\{ \begin{array}{l} \zeta_p{}^2 + \zeta_c{}^2 - 2\zeta_c^2 * airy(r) + (\zeta_p^2 + 1)\zeta_c^2 * (airy(r) \otimes airy(r)) + \\ \sum_{m=0}^{M-1} \psi_m(x)\Big((2\zeta_p\zeta_c \sin\theta_m \cdot \delta(r) + 2\zeta_p\zeta_c(\zeta_p \cos\theta_m - \sin\theta_m) * airy(r) \Big) \end{array} \right\} .
$$

$$
= C + D \sum_{m=0}^{M-1} \psi_m(x)\Big(\sin\theta_m \cdot \delta(r) + (\zeta_p \cos\theta_m - \sin\theta_m) * airy(r)\Big) \tag{5.7}
$$

where $\delta(\cdot)$ is a Dirac delta function, C is a constant that indicates the items unrelated to the feature vector $\psi_m(x)$, and D is also a constant. C can be eliminated by flat-field correction [91, 133] and thus we ignore it for simplicity. Hence,

$$
g \propto \sum_{m=1}^{M} \psi_m(x)\Big(\sin\theta_m \cdot \delta(r) + (\zeta_p \cos\theta_m - \sin\theta_m) * airy(r)\Big)
$$

$$
\triangleq \sum_{m=1}^{M} \psi_m(x) PSF(\theta_m) \tag{5.8}
$$

where PSF denotes the point spread function; i.e., $PSF(\theta_m)$ represents the diffraction pattern with phase retardation θ_m. ζ_p is a microscope information that can be provided by the manufacturer. In our experiments, ζ_p was set to be 0.5. Figure 5.1.1 shows a sample Airy pattern and diffraction patterns with different phase retardations.

We discretize $PSF(\theta_m)$ into a $(2T+1) \times (2T+1)$ kernel, (u, v) element of which is denoted by $\widehat{PSF}(\theta_m, u, v)$. Then, from Eq. (5.8), the imaging model of (i, j) pixel of g is also discretized as

$$
g(i, j) = \sum_{m=1}^{M} \sum_{u=1}^{2T+1} \sum_{v=1}^{2T+1} \psi_m(i+u-T-1, j+v-T-1)\widehat{PSF}(\theta_m, u, v). \tag{5.9}
$$

We define Ψ_m as the vectorized representation of the matrix $\{\psi_m(i, j)\}$ and $h_m(i, j)$ as the vector obtained by vectorizing the sparse matrix whose $(i-T:i+T, j-T:j+T)$ submatrix is $\{\widehat{PSF}(\theta_m, u, v)\}$ and the other elements are zero. Then, Eq. (5.9) is simplified into

$$
g(i, j) = \sum_{m=1}^{M} h_m(i, j)^T \Psi_m, \tag{5.10}
$$

97

and thus the vectorized form of the phase contrast microscopy image $\{g(i,j)\}$ can be modeled as

$$g = \sum_{m=1}^{M} H_m \Psi_m, \ \ s.t. \ \Psi_m \geqslant 0 \tag{5.11}$$

where H_m is the matrix obtained by stacking up row vectors $\{h_m(i,j)^T\}$ in order. Note that when g consists of P pixels in total, H_m is a sparse $P \times P$ matrix, each row of which contains at most $(2T+1) \times (2T+1)$ non-zero elements.

5.1.3   The Restoration of the Phase Contrast Images

Based on the theory of sparse representation [94], we formulate the following optimization problem to restore the feature vectors $\{\Psi_m\}$ from Eq. (5.11):

$$min \sum_{k=1}^{K} \left(\|\Psi_{m_k}\|_1 + w_s \Psi_{m_k}^T \mathbf{L} \Psi_{m_k} \right) \ s.t. \ \begin{cases} \|g - \sum_{k=1}^{K} H_{m_k} \Psi_{m_k}\|_2 < \varepsilon \\ \\ \Psi_{m_k} \geqslant 0 \end{cases} \tag{5.12}$$

where $\mathbf{L}$ is a Laplacian matrix defining the similarity between spatial pixel neighbors [133]; w_s is the weight determining the spatial smoothness, which was set between 0.2 to 0.4 in our experiments; and, K is the number of representative retardations, the optimal value of which can vary with the cell type and property.

We propose an iterative optimization algorithm to solve this L1-norm minimization problem since it is known that there is no closed-form solution for such a problem. We iteratively search the best-matching basis in the dictionary $\{H_m\}$ with the matching pursuit algorithm [94], and then utilize a non-negative multiplicative updating method [118] to obtain the nonnegative feature vectors $\{\Psi_{m_k}\}$. The detailed procedure is described in Algorithm 2.

Solving Eq. (5.12) yields a set of K coefficient vectors, $\{\Psi_{m_1}, \cdots, \Psi_{m_K}\}$. Based on the result, each pixel's phase retardation caused by cells can be represented as a linear combination of K representative phase retardations where the coefficients are the corresponding elements of $\{\Psi_{m_1}, \cdots, \Psi_{m_K}\}$.

Algorithm 2 Optimization Algorithm for the Image Restoration

Input g: vectorized image, $\{H_m\}$ dictionary matrices, K: number of representative retardations,

Output $\{\Psi_{m_k}\}$: feature representation vectors.

Initialization $R_g^1 \leftarrow g$, $P \leftarrow$ size of g.

  for $k = 1 \rightarrow K$ **do**

    // *Search for the best matching basis H_{m_k} using matching pursuit method* [94]

    for $m = 1 \rightarrow M$ **do**

      Compute inner product: $\vec{\rho}_{m,i} = \langle H_m(:,i), R_g^k \rangle, \forall i \in \{1,\cdots,P\}$

    end for

    $m_k \leftarrow \arg\max_m \|\vec{\rho_m}\|$

    // *Calculate the feature vector Ψ_{m_k} using non-negative multiplicative updating* [118]

    Formulate a subproblem from Eq. (5.12):

      $min\|\Psi_{m_k}\|_1 + w_s\Psi_{m_k}{}^T\mathbf{L}\Psi_{m_k} \quad s.t. \ \|R_g^k - H_{m_k}\Psi_{m_k}\|_2 < \varepsilon_k \ and \ \Psi_{m_k} \geqslant 0.$

    Obtain the feature vector Ψ_{m_k} by applying non-negative multiplicative updating

    // *Update the residual error*

    $R_g^{k+1} \leftarrow R_g^k - H_{m_k}\Psi_{m_k}$

  end for

5.1.4   Qualitative Evaluation of the Restoration Method

In order to empirically demonstrate that the proposed image restoration method results in more effective microscopy image analysis, we applied our restoration method for cell region detection and compared the result with the previous restoration method's.

After image restoration, each pixel x was clustered into one of K groups $(1 \cdots K)$ or back-

ground (0) as follows.

$$group(x) = \begin{cases} \arg\max_k \Psi_{m_k}(x) & if \ \max \Psi_{m_k}(x) > th \\ 0 & otherwise \end{cases} \quad (5.13)$$

where th is a threshold for foreground selection. In other words, each location's phase retardation is determined as the most like phase retardation among the K representative phase retardations unless the corresponding coefficient is too small. In our experiment, we set the dictionary size M and the number of representative phase retardations K to be 20 and 3, respectively.

The experiments were performed on three phase contrast microscopy images that capture bovine aortic endothelial cells, muscle-derived stem cells, and C2C12 myoblastic stem cells. Each image contains 1040×1392 pixels. (For quantitative results on time-lapse images, we refer to [121].)

Figure 5.1.4 demonstrates that our dictionary-based approach achieved high quality cell detection. In addition to dark cells, bright cells that undergo mitosis/apoptosis or are dead were also well detected (Figure 5.1.4(b),(c)). These results show that image restoration is a way to improve the microscopy image quality and analysis. On the other hand, the previous method [133] failed to detect bright cells (Figure 5.1.4(d)). These results clearly demonstrate that the assumption of the previous method on the phase retardation being close to zero is not valid for bright cells.

5.2 Differentiation Detection for C2C12 myoblastic stem cells

In this section, we propose a supervised learning framework for differentiation detection in phase contrast microscopy. As the first step, we propose diffraction pattern filtering (DPF) to enhance the quality of phase contrast microscopy images. DFP shares the same idea with the image restoration algorithm introduced in the previous section; thus, it shows the same good performance and discriminative power. In addition, DPF is orders of magnitude more efficient. We validate the proposed framework on muscle myotube detection, obtaining convincing results on
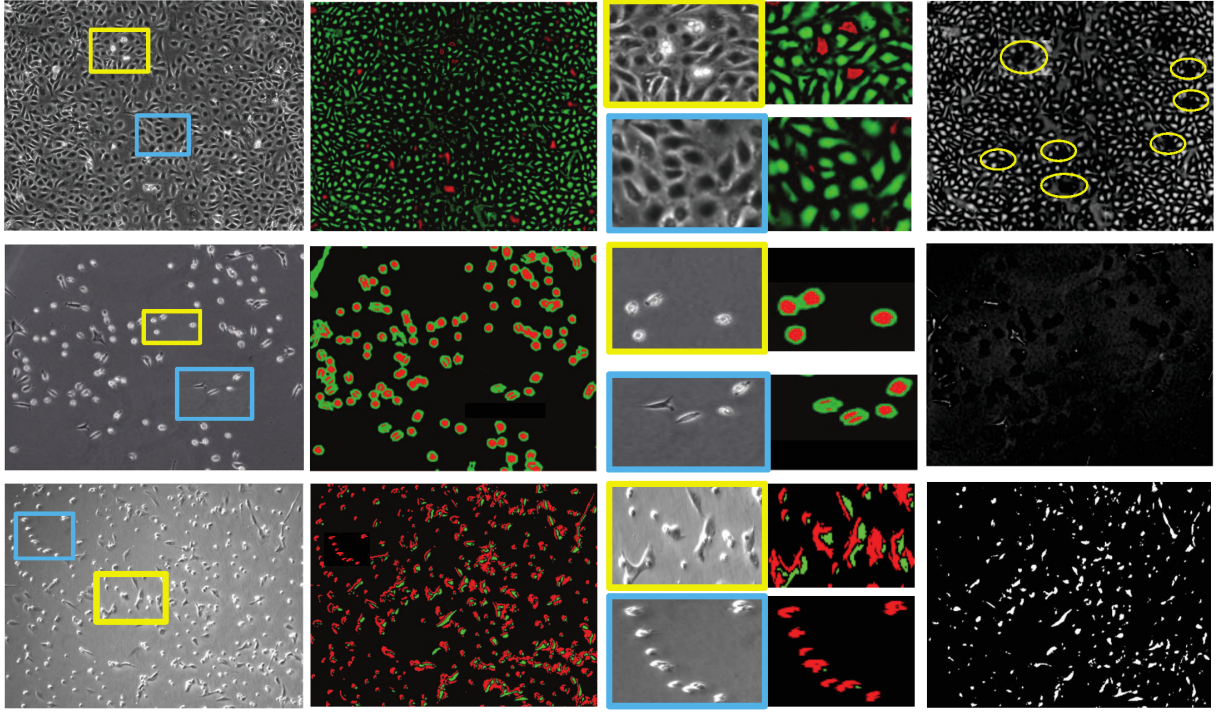
Figure 5.2: Cell detection results on images capturing bovine aortic endothelial cells (top), muscle-derived stem cells (middle), and C2C12 myoblastic stem cells (bottom). (a) Original phase-contrast images, (b) cell region detection results of the proposed method, (c) zoom-in images of the proposed method's results, and (d) cell region detection results of the previous method [7]. Different colors indicate different phase retardations. Mostly dark cells and bright cells correspond to two different phase retardations marked with green and red colors, respectively. Yellow ellipses in the first row indicate undetected group of cells. In the second and third rows, it is obvious that the previous method fails to detect most of mitotic, apoptotic, and dead cells.

a dataset of 300 images compared to detection results using staining image.

5.2.1 Diffraction Pattern Filtering

We propose a diffraction pattern filtering (DPF) algorithm that can enhance the quality of phase contrast microscopy images in a far more efficient way than the restoration method. As demonstrated in the previous section, the image restoration method modeling the phase contrast microscopy image formulation process is effective to improve image analysis. However, it requires

$\theta_1 = 0 \quad\quad \theta_2 = \pi/4 \quad\quad \theta_3 = \pi/2 \quad\quad \theta_4 = 3\pi/4 \quad\quad \theta_5 = \pi \quad\quad \theta_6 = 5\pi/4 \quad\quad \theta_7 = 3\pi/2 \quad\quad \theta_8 = 7\pi/4$
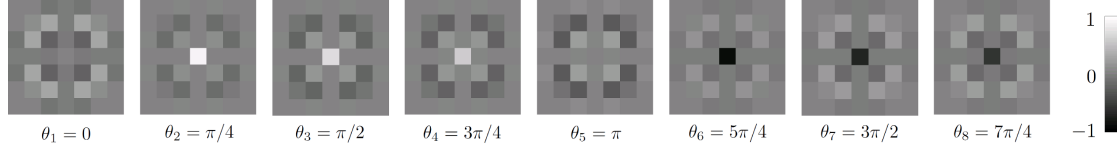
Figure 5.3: Diffraction pattern filter bank with parameters $M = 8$, $r = 3$, $\zeta_p = 0.5$, $R = 10$, and $W = 2$. This filter bank was used in our experiments.

a considerable amount of computation since it solves a deconvolution problem. Instead of solving such a computationally costly problem, we filter a phase contrast image with the basis diffraction patterns introduced by the phase contrast image formation model. This filtering method demonstrates almost identical discriminative power to the restoration method on differentiation detection, likely because they share the same theoretical foundation.

Based on the dictionary representation, a phase contrast microscopy image g can be modeled as a linear combination of M diffraction patterns as follows:

$$g = \sum_{m=1}^{M} \Psi_m * \Big(\sin\theta_m \delta(r) + (\zeta_p \cos\theta_m - \sin\theta_m) \cdot airy(r) \Big) \tag{5.14}$$

where θ_m is the m-th phase retardation among M equally distributed phases within 2π, i.e., $\theta_m = 2\pi \frac{m-1}{M}$; ζ_p is the amplitude attenuation factors caused by the phase ring; $\delta(\cdot)$ is a Dirac delta function; and $airy(r)$ is an obscured Airy pattern with radius r, which is a diffraction pattern with a bright region in the center surrounded by a series of concentric dark and bright rings:

$$airy(r) = R\frac{J_1\big(2\pi Rr\big)}{r} - (R - W)\frac{J_1\big(2\pi(R - W)r\big)}{r} \tag{5.15}$$

where R and W are the outer radius and width of the phase ring, respectively, and $J_1(\cdot)$ is the first order Bessel function of the first kind.

From Eq (5.14), we define a diffraction pattern filter bank as follows:

$$DPF(m; M, r, \zeta_p, R, W) \equiv \tag{5.16}$$

$$\sin\theta_m \delta(r) + (\zeta_p \cos\theta_m - \sin\theta_m) \cdot airy(r)$$

for $m = 1, \cdots, M$, where M is the size of the filter bank and r is the radius of the filters. The parameters ζ_p, R, and W can be obtained from the microscope manufacturer or, if not, they can be learned from labeled data or manual inspection of results. Each filter is normalized to have unit L2 norm. Fig. 5.3 shows a set of diffraction patterns when $M = 8$.

Given a phase contrast image g, after flat-field correction, these filters are applied to g:

$$\Phi_m = g * DPF(m). \tag{5.17}$$

As a result, M filtered images $(\Phi_1, \cdots, \Phi_M)$ are obtained. After filtering, the negative values in the filtered images are replaced with 0, i.e.,

$$\Phi_m^+ = max(\Phi_m, 0). \tag{5.18}$$

Negative values are excluded because we have both a filter and its inverse in the filter bank (i.e., $DPF(m + M/2) = -DPF(m)$) and these two cases with two different retardation phases need to be separately handled. Fig. 5.4 shows an example of a phase contrast image (g) and its filtered outputs $(\Phi_1^+, \cdots, \Phi_M^+)$. Similar to the restoration results reported in the previous section, filtered outputs with different phase retardations respond to different entities, largely among bright cells, dark cells, and bright halos.

Since each basis pattern filter is normalized, the response to the filtering is the length of the projection of g onto the direction of the pattern. When an input is a normalized image whose pixel values are between 0 and 1, the values of filtered outputs are also between 0 and 1. Therefore, filtered outputs can also be considered images as they are, and any feature extraction scheme that can be applied to the original image can also be applied to each of the filtered output images. Furthermore, visualization of the outputs is straightforward.

The filtered outputs $\{\Phi_m^+\}$ are not the same as the restored images $\{\Psi_m\}$ in Eq. (5.14) since the bases are not orthogonal to each other, and thus cannot be used for restoration; however, in terms of discriminative power both the images show almost the same capability on detection or classification tasks as we will empirically show in Section 5.2.3, because they share the same theoretical foundation and thus similarly informative.
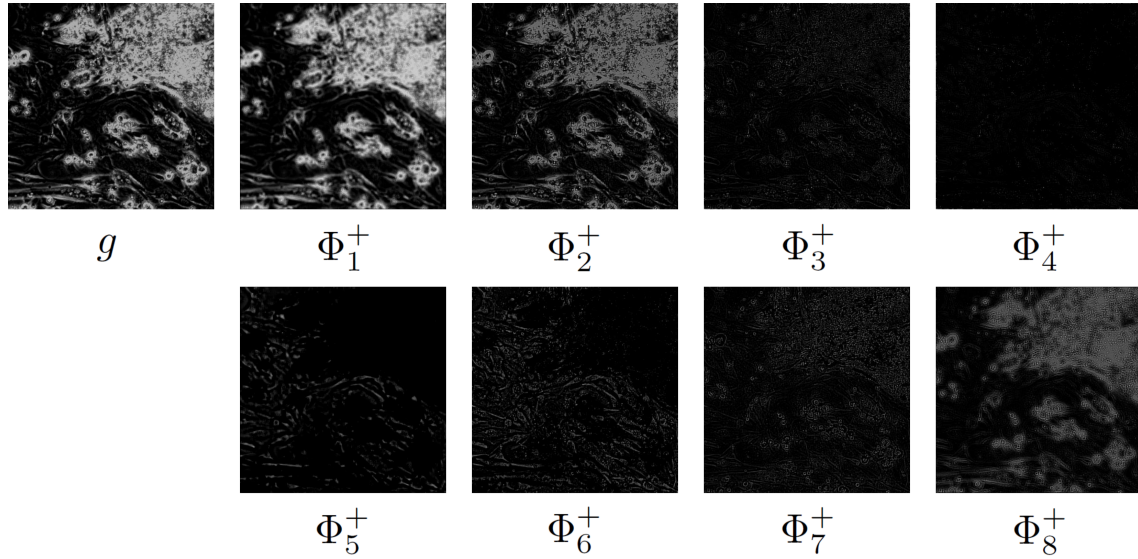
Figure 5.4: Phase contrast image (g) and its diffraction pattern filtered outputs ($\Phi_1^+, \cdots, \Phi_8^+$).

Our DPF method has advantages over the restoration method in several aspects.

First, our filtering method is far more efficient than the restoration method in terms of computation time (less than one second vs. a few minutes for processing one image in a typical setting). The restoration method needs to solve a deconvolution problem, which does not have a closed-form solution, but involves an iterative optimization process. This inefficiency can be an issue not only in a real-time system, but also sometimes in a batch system because parameter setting of M and r (and also ζ_p, R, and W unless the information is available.) requires multiple executions.

Second, our filtering method is significantly more economical in terms of memory use. The restoration method involves a large kernel matrix, the size of which is $P \times P$, where P is the number of pixels in the phase contrast image. Although the kernel matrix is sparse, it still requires a lot of memory since P is often greater than a million in a typical setting. One may suggest dividing the image into several subimages to apply the restoration method, but what would be an appropriate size for the subimages and how to stitch the restoration results are still an open question.
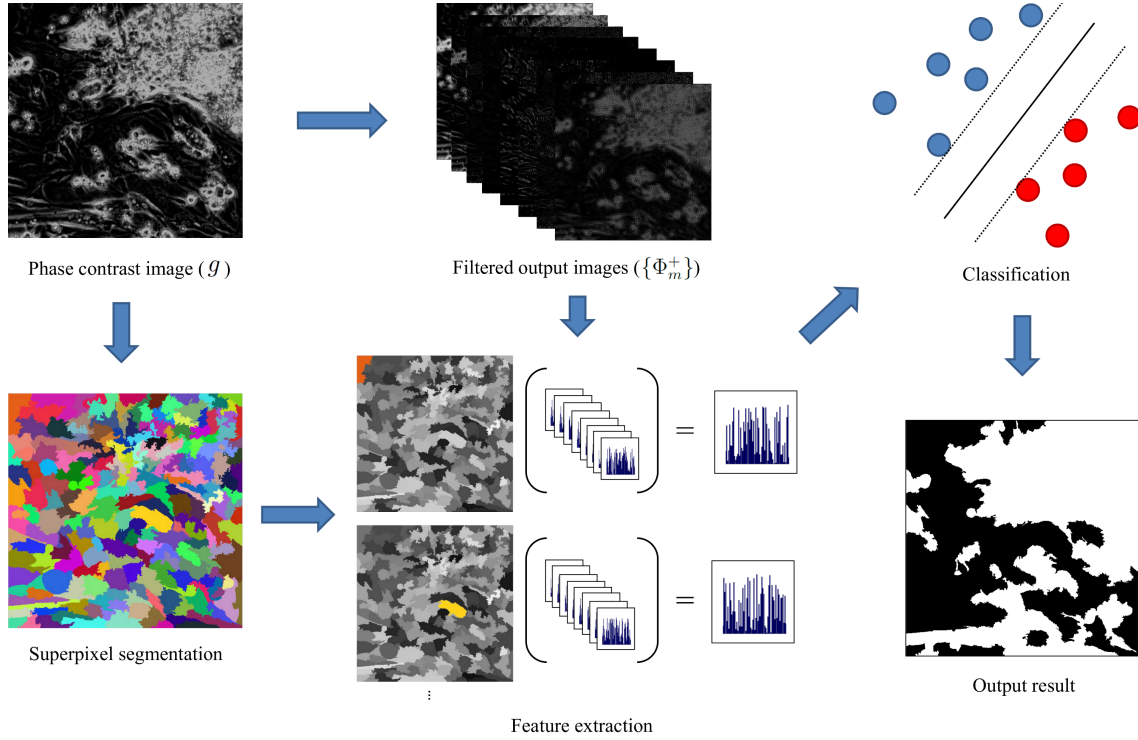
Figure 5.5: Overview of the framework for differentiation detection.

Third, the results of our method is stable in that it uses each of M bases once and the order of filtering does not affect the results. Whereas the restoration method does not show such stability since it often selects different sets of bases in a different order (with repetition) for different images when they do not show similar levels of cell density and matureness. In addition, the restoration method converges to a local optimum; thus, the results can vary depending on optimization schemes.

Lastly, the implementation of our method is much simpler.

The restoration method selects K representative phase retardations among M phases using a greedy method. On the other hand, our method uses all M phase at the filtering step; the number of features can be reduced after feature extraction using some statistical method, such as singular value decomposition (SVD) [104].

5.2.2 Framework for Differentiation Detection in Phase Contrast Microscopy

We propose a supervised learning framework for differentiation detection in phase contrast images that comprises four steps: diffraction pattern filtering, superpixel segmentation, feature extraction, and classification, as overviewed in Fig. 5.5.

Step 1. Diffraction pattern filtering: given a phase contrast image, we first locate the foreground area by dilating the edge map of the image since the background generally has uniform texture without edges. We compute the median pixel value of the background area, which is the inverse of the foreground area, and subtract it from the entire image for flat-field correction. We apply DPF to the corrected image in order to obtain the filtered images.

Step 2. Superpixel segmentation: we divide the phase contrast image into segments, or superpixels, based on pixel intensity similarity. Superpixel segmentation not only lowers the computational cost by reducing the number of samples to be examined, but also enhances the detection accuracy by incorporating neighborhood information. Among various superpixel methods, we chose the entropy rate superpixel segmentation method that can explicitly control the size balance, with the reported parameter setting [79].

Step 3. Feature extraction: Over each superpixel area, we quantify the texture pattern of every pixel and then measure the distribution of the pattern labels as a feature vector for each filtered image. After feature vectors are computed for all filtered images, the vectors for the same superpixel area are concatenated into one as the feature vector of the superpixel. In our experiment, we extract rotation invariant uniform local binary pattern (LBP^{riu2}) [97], which is one of the most effective texture features. We reduce the number of features by applying SVD.

Step 4. Classification: using the extracted features, we train a linear support vector machine over superpixels. The superpixels that contain more positive pixels than negative ones are used as positive samples and the opposite cases as negative samples. Testing is also conducted over superpixels; as a result, the pixels belonging to the same superpixel are determined to have the same label.

5.2.3 Muscle Myotube Detection

We apply the proposed framework using diffraction pattern filtering for muscle myotube detection and present the results.

To the best of our knowledge, there is no previous image processing algorithm for muscle myotube detection in phase contrast microscopy images. The closest work would be segmentation of myofibers in muscle biopsy samples, where multiple myofibers in similar shape and size cover the whole field of view, using fluorescence images [17, 123]. Our work is quite different from these works: first, we use phase contrast microscopy images, which are not guided by fluorescent staining; second, we detect myotubes among different stages of cells (myoblasts, nascent myotubes, and mature myotubes), which show various size and shape, and are arbitrary located in the field of view.

Problem Definition: During development of muscle fibers, muscle myotubes are formed by the fusion of mononucleated progenitor cells known as myoblasts. More specifically, single-nucleated myoblasts first fuse to form a nascent myotube; thereafter, additional myoblasts fuse with the nascent myotube to form a thick and mature myotube that may contain as many as 30 nuclei within a single cell [57] (See Fig 5.6.).

Given a phase contrast image containing both myoblasts and myotubes, the goal of muscle myotube detection is to locate myotubes. In other words, the task is to determine whether or not each pixel of the image belongs to myotubes.

Data and Comparison: Three sets of phase contrast images of mouse C2C12 myoblasts were acquired under three different culture conditions with different amount (100ng/ml, 500ng/ml, and 1000ng/ml) of IGF2, which accelerates differentiation. Each set contains 100 images; thus, 300 images were obtained in total. Each image contains 640×640 pixels with a resolution of 1.3μm. Figure 5.7 show examples of images with different amount of IGF2.

For comparision, immunofluorescence staining images capturing myotubes were acquired. Each staining image was reduced to a binary image by intensity thresholding.

(a) **(b)** **(c)**
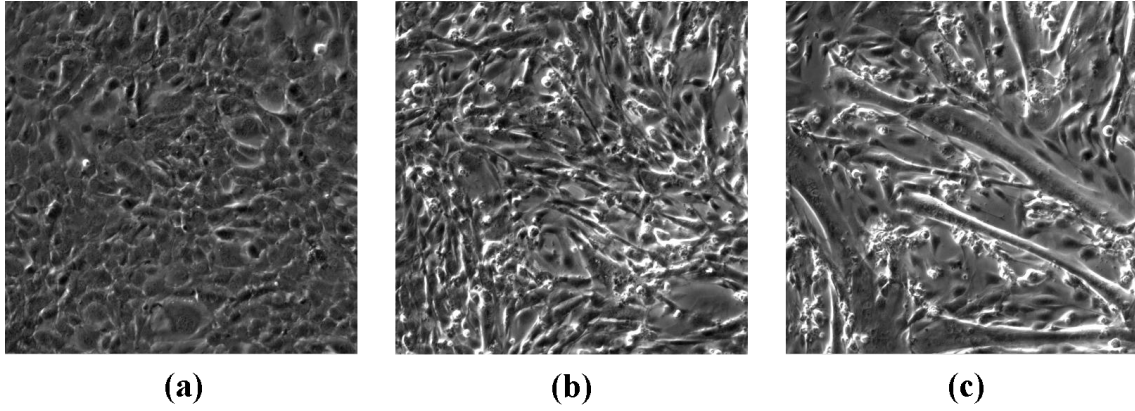
Figure 5.6: Process of myotube formation: (a) single-nucleated myoblasts; (b) nascent myotubes formed by the fusion of myoblasts; (c) mature myotubes formed by the additional fusion of myoblasts with nascent myotubes.

(a) (b) (c)
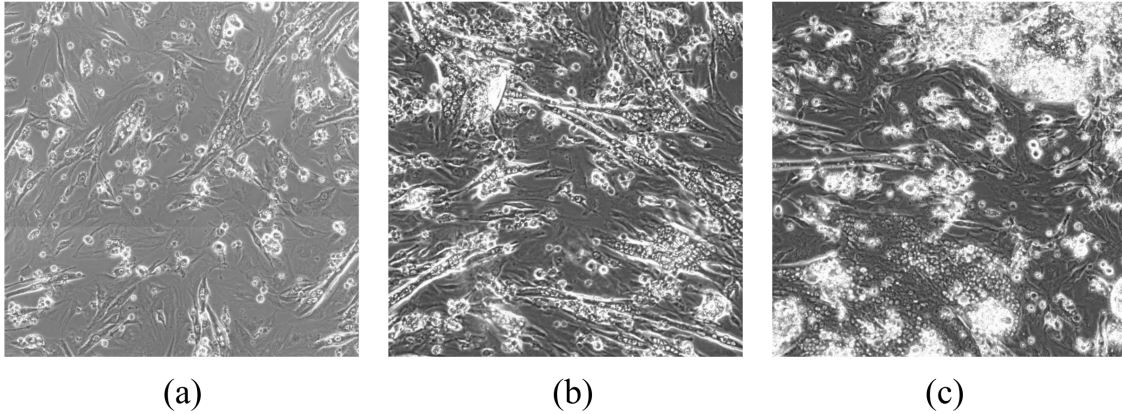
Figure 5.7: Image data with different amount of IGF2: (a) 100ng/ml, (b) 500ng/ml, and (c) 1000ng/ml.

The images and the data used for comparision, which are differentiation detection results based on staining images, are available on the author's web page (www.cs.cmu.edu/~seungilh).

Experiments and Results: We compare our myotube detection method with the method that does not adopt either DPF or superpixel segmentation. In this baseline method, feature extraction was performed on a phase contrast image, not filtered images, and features were computed for each pixel within its circular neighborhood (the radius was determined using a validation scheme.). We also compare our method with the method that adopts DPF, but not superpixel segmentation, to distinguish the contribution of DPF and superpixel segmentation. We perform

Table 5.1: Myotube detection accuracies in terms of F-measure. Diffraction pattern filtering (DPF) and superpixel segmentation (SS) considerably enhance detection accuracy.

	IGF2-100	IGF2-500	IGF2-1000
Baseline	0.32±0.06	0.53±0.11	0.67±0.10
+DPF	0.44±0.08	0.68±0.09	0.79±0.07
+DPF & SS	0.64±0.06	0.77±0.05	0.86±0.06

Table 5.2: Performance comparison between our diffraction pattern filtering (DPF) and the restoration (RES) methods.

	IGF2-100	IGF2-500	IGF2-1000	Time
DPF	0.64±0.06	0.77±0.05	0.86±0.06	< 1 sec
RES	0.63±0.08	0.76±0.07	0.86±0.06	262 sec

10-fold evaluation; for each set of images, we used 90 images for training in turn and the rest for test. For each image, we compare the detection result with the result based on the statining image, computing F-measure, which is the harmonic mean of precision and recall.

As shown in Table 5.1, the proposed method achieves 64% to 86% accuracy in terms of F-measure, the harmonic mean of precision and recall when compared to the result based on the staining image (It is worth mentioned that we compare our result with the result based on the staining image not because it is not perfect, but because it is the method currently used. The result based on the staining image often shows not a few false positives as the staining reagents happen to be attached to undifferentiated cells.). Myotube detection is more accurate under the condition with more amount of IGF2 because additional IGF2 leads to more mature myotubes the texture of which is more distinctive from that of myoblasts. Applying DPF results in 12% to 15% gain in accuracy compared to the baseline method; and superpixel segmentation leads to additional 7% to 20% performance gain. These results validate that the proposed framework adopting both DPF and superpixel segmentation are effective for myotube detection. Fig. 5.8
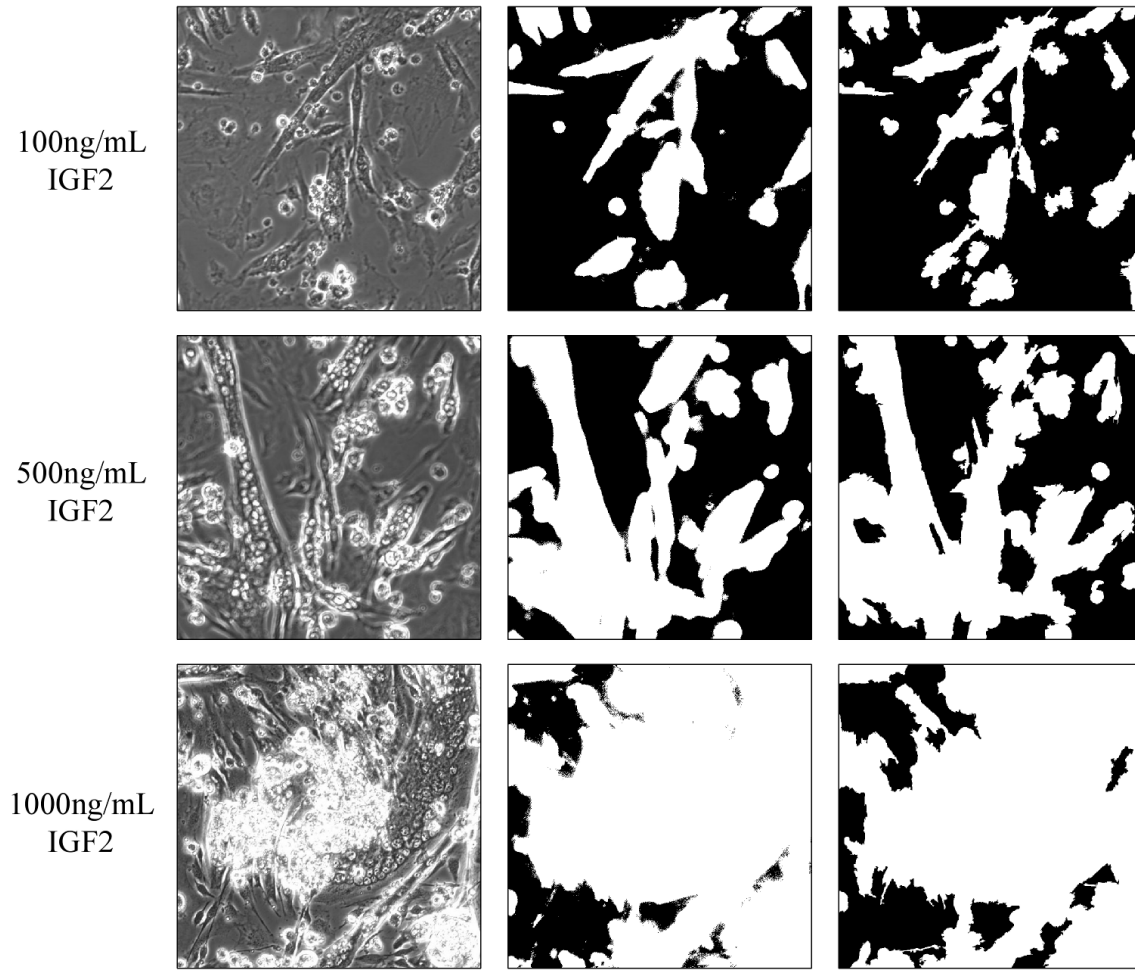
Figure 5.8: Phase contrast images (left), myotube detection results based on staining image (center), and myotube detection results using the proposed method (right). In the binary images, white pixels indicate where myotubes are detected. Images at each row are obtained from different culture conditions in terms of the amount of IFG2: 100ng/ml (top), 500ng/ml (middle), and 1000ng/ml (bottom). As more amount of IFG2 is added, more and thicker myotubes are formed.

shows examples of the results.

Table 5.2 demonstrates that DPF and the restoration method have almost the same discriminative power; the average accuracy difference was less than 1%. In terms of running time, DPF is hundreds times faster than the restoration method. Superpixel-wise classification is also hundreds times faster than pixel-wise classification.

5.3   Summary of Differentiation Detection

We have proposed a supervised framework for differentiation detection and applied it to C2C12 myoblastic cell differentiation detection. To make the image analsysis more reliable, we proposed a phase contrast image restoration method based on the dictionary representation with diffraction patterns. This method restores phase retardation caused by cells, over which cell region detection can be more effectively performed, albeit with a considerable amount of computation. In order to reduce the computation complexity, we proposed diffraction pattern filtering (DPF) based on the same theoretical foundation as the restoration method; as a result, DPF is as effective as the restoration method in accuracy and far more efficient in computation. With the DPF filtering and superpixel representation, we built up a framework for differentiation detection and tested it on myotube detection, achiving good accuracy compared with results generated by a staining method.

Our contribution to differentiation detection can be summarized as follows:

- To the best of our knowledge, differentiation detection has not been performed without a staining method. This work is the first work that develops a vision-based method for differentiation detection in non-fluorescent microscopy.

- We proposed a phase contrast microscopy image formulation model based on dictionary representation, which provides a deeper understanding on phase contrast microscopy. The dictionary-based approach can be applied to another type of non-fluorescent microscopy, such as differential interference contrast (DIC) microscopy.

- We proposed a diffraction pattern filtering, an efficient way to improve the quality of phase contrast microscopy. The filtering method can be adopted for various types of tasks, such as cell segmentaion and nucleus detection, in phase contrast microscopy analysis.

Chapter 6

Cell Tracking

In this chapter, we present a cell tracking system as a comprehensive tool for cell behavior analysis and analyze wound healing assays using the system. An automated cell tracking system adopting phase contrast microscopy monitors live and intact cells in a long time period, which is cumbersome or often intractible by manual operation. Given time-lapse microscopy, the system produces various quantitative biological measurements, e.g., the number of cells, cell confluence, cell lineage, cell migration speed and direction, etc. The information can be used for research in biology or biomedical engineering, such as the discovery of optimal condition for cell culturing and quality assurance or control.

We propose a cell tracking system that integrates the functionality of mitosis detection that is performed independently of cell tracking. In other words, our tracking system includes a mitosis detection module, which provides the information on when and where mitotic events occur. In fact, mitosis detection is critical for tracking performance because cell divisions, which lead to the branching of tracking trajectories, are a major cause of tracking failure. The changes in cell shape, size, and brightness during mitosis encumber automated tracking due to difficulty in cell region segmentation as well. Mitosis detection is also important for cell lineage construction since correctly detected mitosis reveals the relation between mother and daughter cells. We empirically demonstrate that the mitosis detection functionality significantly improves the accuracy

of cell tracking and the quality of cell lineage construction, through extensive experiments performed on 48 sequences capturing C2C12 myoblastic stem cells. We also show that our tracking method outperforms the state-of-the-art method.

We apply our cell tracking system for the analysis of wound healing assay. The wound healing assay *in vitro* is widely used for research and discovery in biology and medicine. This assay allows for observing the healing process *in vitro* in which the cells on the edges of the artificial wound migrate toward the wound area. The influence of different culture conditions can be measured by observing the change in the size of the wound area. For further investigation, more detailed measurements of the cell behaviors are required. Our cell tracking system tracks cells during the healing process and provides detailed spatio-temporal measurements of cell behavior. This application demonstrates the effectiveness of our cell tracking system.

Figure 6.1 shows the summary of our cell tracking system capabilities. Our cell tracking system detects and tracks each of tens to hundreds of cells for a few days, monitoring individual cell movement and generating cell lineage.

The remainder of this chapter is organized as follows. In Section 6.1, we present a cell tracking system that integrates the mitosis detection functionality with cell segmentation, cell tracking by association, and biological statistics computation modules. In Section 6.2, we introduce an application of our cell tracking system to the analysis of wound healing process. We summarize this chapter in Section 6.3.

6.1   Cell Tracking System

In this section, we present a cell tracking system based on detection and association approach that incorporates the functionality of mitosis detection introduced in Section 3.1, which is performed independently of cell tracking [52]. Through the extensive experiments on 48 C2C12 myoblastic stem cell populations under four different conditions, we show that cell birth information provided by precise mitosis detection can significantly improve the performance of cell
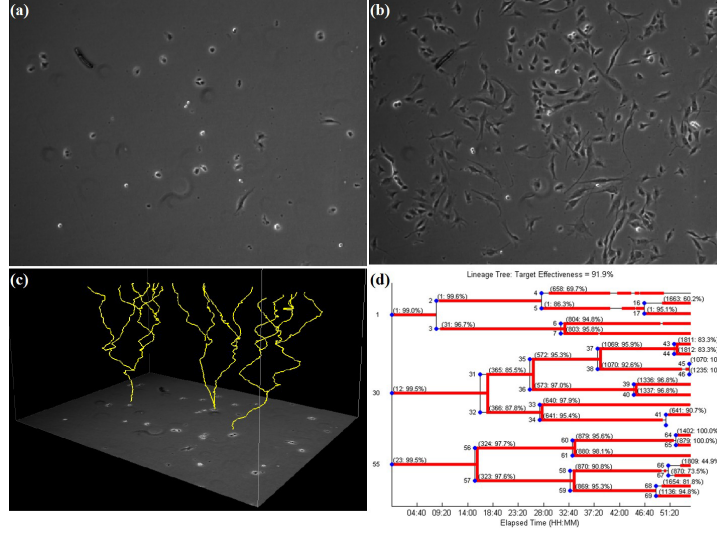
Figure 6.1: The data and results of our cell tracking systems. Our systems detect and track individual cells in time-lapse phase contrast microscopy images until the number of cells becomes a few hundreds, generating cell trajectories and lineages. (a) The first frame of a time-lapse microscopy image sequence (containing around 20-30 cells). (b) The last frame of the same sequence (containing around 200-300 cells) (c) Trajectories of three cells and their prodigy cells shown in 3d space - (x,y) position and time. (d) Cell lineages of three cells and their quality evaluation. The cell lineages generated by our system (red thick lines) overlay the cell lineages by manual annotation (black thin lines).

tracking, resulting in more quality cell lineage construction. We also compare our cell tracking system with a state-of-the-art cell tracking system [74] to show the effectiveness of our system.

6.1.1 Approach

Our tracking system consists of four modules: modules for cell segmentation, mitosis detection, cell tracking, and cell behavior quantification, as shown in Figure 6.2. The cell tracking module performs frame-by-frame association based on the cell regions and mitosis detected by the first two modules. The last module processes cell tracking results, yielding various metrics that qualify cell behavior. In this section, we present how to segment cells and associate them over consecutive frames along with incorporating mitosis detection results. We use the mitosis detection algorithm introduced in Section 3.1. We will present the result of cell behavior quantification
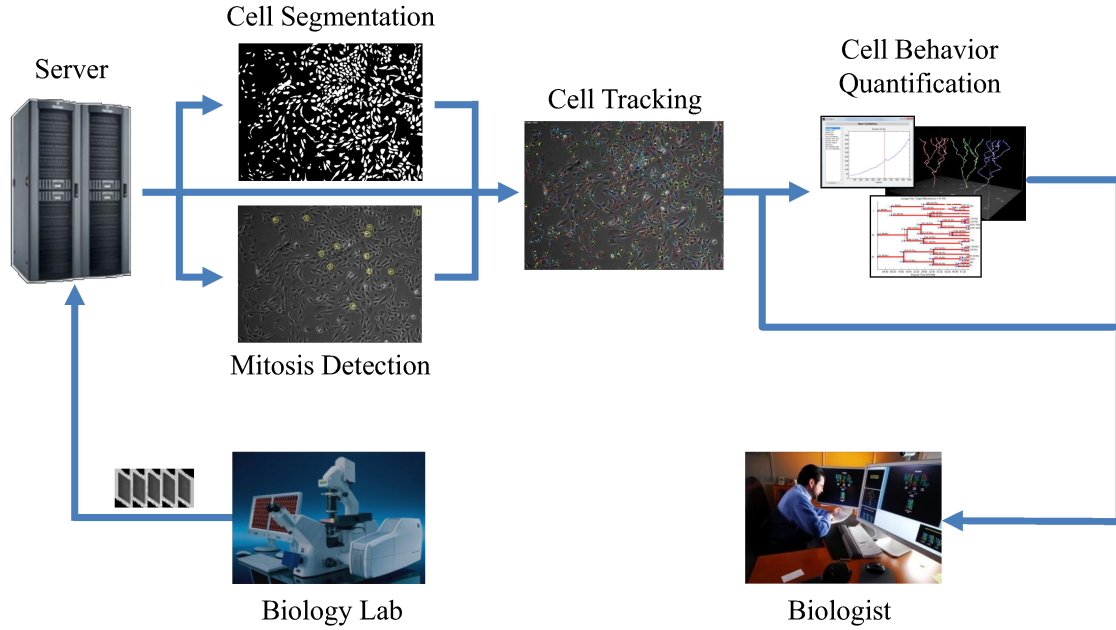
Figure 6.2: Work-flow of our cell tracking system. The system first detects cell regions and mitosis, based on which cell tracking is performed by frame-by-frame association. Cell tracking results are used for cell behavior quantification.

(a)   (b)
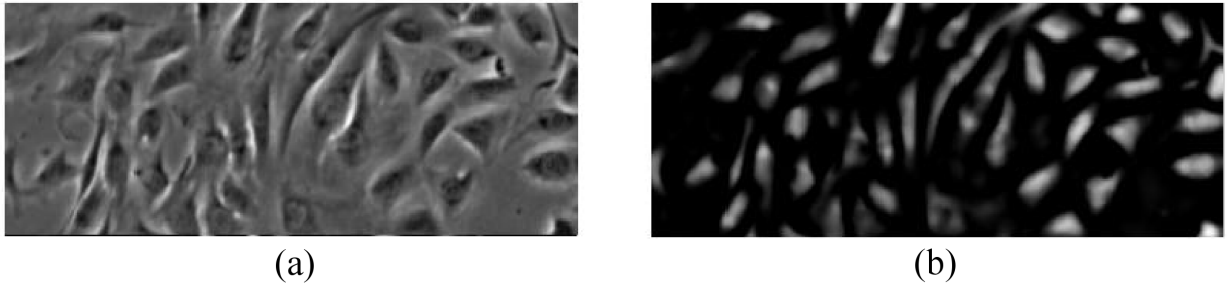
Figure 6.3: Microscopy image restoration result: (a) phase contrast microscopy image and (b) its restored image.

in Section 6.2.

Cell Segmentation: Figure 6.3(a) shows a typical phase contrast image where cells are surrounded by bright halos, some subcellular structures such as nucleus are shown dark, and cytoplasm often has similar intensity to the background. Due to these properties, traditional image segmentation techniques have difficulty in segmenting cells in phase contrast microscopy. Thus, we instead adopt a microscopy imaging model [133] that models the phase contrast mi-

116

croscopy image formation process and formulate a regularized quadratic cost function to restore the artifact-free image from a phase contrast image:

$$\mathbf{f}^* = \arg\min_{\mathbf{f}} ||\mathbf{Hf} - \mathbf{g}||_2 + \omega_l \mathbf{f}^T \mathbf{Lf} + \omega_s ||\Lambda_s \mathbf{f}||_1 + \omega_t (\mathbf{f} - \mathbf{f}_t)^T \Lambda_t (\mathbf{f} - \mathbf{f}_t) \qquad (6.1)$$

where $\mathbf{f}^*$ is the vectorized image to be restored, $\mathbf{H}$ is the imaging model in a matrix format from [133], and $\mathbf{g}$ is the vectorized observed image, or the given phase contrast image.

The first regularization term in Eq. (6.1) is spatial smoothness where $\mathbf{L}$ is a Laplacian matrix defining the spatial intensity similarity between neighboring pixels such as the one used in [70]. The second regularization term is an L1-sparsity term where Λ_s is a diagonal matrix penalizing large $\mathbf{f}$ values. The last regularization term is to maintain the temporal consistency between consecutive images where Λ_t is a diagonal matrix defining the intensity similarity between neighboring pixels in the temporal domain and $\mathbf{f}_t$ is the restored image in the previous frame. The optimal weights for the three regularization terms $\{\omega_l, \omega_s, \omega_t\}$ are learned from training images by grid-search. The regularized objective function can be minimized using a nonnegative updating scheme [118]. After obtain $\mathbf{f}^*$ as shown in Figure 6.3(b), a simple thresholding method is applied to separate cell regions from the background.

Cell Tracking by Frame-by-frame Association: Based on the segmented blobs, each of which can be one of an individual cell, a cell clusters, and a false positive, we perform frame-by-frame data association between the cells in the previous frame and the blobs segmented in the current frame. For the association, we consider five hypotheses reflecting cell behaviors, namely migration, exit, entrance, clustering, and mitosis, as shown in Figure 6.4.

More formally, let a_i be the i-th detected cell in the previous frame and b_j be the j-th blob in the current frame. Then, likelihoods of the five cases are computed as follows:

(1) one-to-one: a cell migrates in the field of view.

$$\ell_{1 \to 1}(a_i, b_j) = e^{-\frac{||f(a_i) - f(b_j)||}{\sigma}} \qquad (6.2)$$

where $f(a)$ is a feature vector from cell or blob a, which consists of the center position of the blob, the Fourier descriptors of the blob contour, and the intensity histogram of the blob region;

117
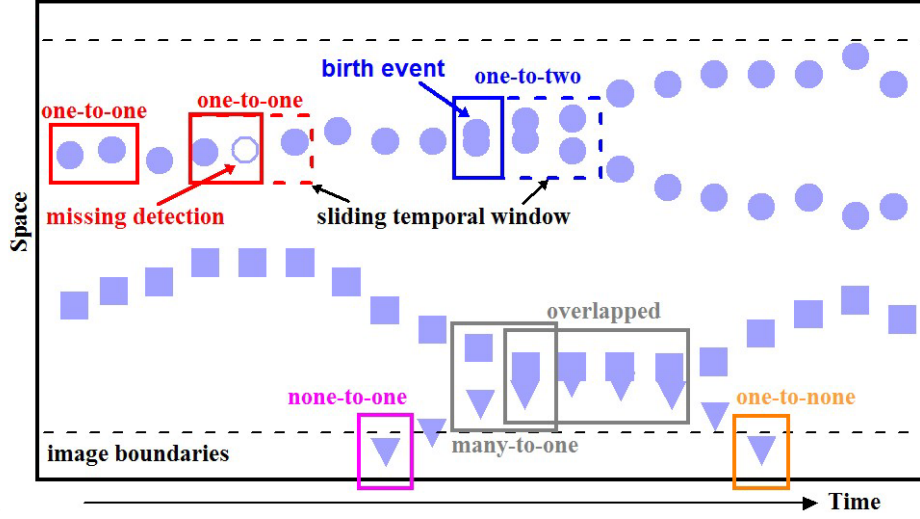
Figure 6.4: Five hypotheses of cell behavior: migration, exit, entrance, clustering, and mitosis.

σ is a free parameter to adjust the distribution. The likelihood of a one-to-one hypothesis is computed based on the distance between two feature vectors. In order to reduce the number of hypotheses considered in frame-by-frame data association, we consider the pairs of a cell and a blob the distance between which is less than a certain threshold. If there is no blob in the current frame that can correspond to a cell in the previous frame, either an existing blob is not detected in the current frame or the cell is incorrectly detected in the previous frames; thus, we examine the following several frames to find out which is the case and either associate the cell with a blob or discard the cell as false positive.

(2) one-to-none: a cell exits from the field of view.

$$\ell_{1\to 0}(a_i) = e^{-\frac{d(a_i)}{\lambda}} \tag{6.3}$$

where $d(a_i)$ computes the spatial distance between the centroid of cell a_i and the image boundary. λ is a free parameter to adjust the distribution. For only cells near the image boundary, we consider this one-to-none hypothesis.

(3) none-to-one: a cell enters the field of view.

$$\ell_{0\to 1}(b_j) = e^{-\frac{d(b_j)}{\lambda}} \tag{6.4}$$

118

Similar to one-to-none hypothesis, only for blobs near the image boundary, we consider this none-to-one hypothesis.

(4) many-to-one: multiple cells overlap.

$$\ell_{K \to 1}(a_{i_1}, \cdots, a_{i_K}, b_j) = e^{-\frac{||f(\bigcup_{k=1}^{K} a_{i_k}) - f(b_j)||}{\sigma}} \tag{6.5}$$

When several cells are close to each other in the previous frame and at the same location a large blob is detected in the current frame, we consider a many-to-one hypothesis. We shift the multiple cells in the previous frame to merge them into a unified cell region and compute its feature vector. We apply a contour-matching method [11] to keep each cell's identity in the cluster.

(5) one-to-two: a cell divides into two cells.

$$\ell_{1 \to 2}(a_i, b_{j_1}, b_{j_2}) = e^{-\frac{||f(a_i) - f(b_{j_1} \cup b_{j_2})||}{\sigma}} \tag{6.6}$$

To compute the feature vector of two potential daughter cell blobs, we translate b_{j_1} and b_{j_2} towards each other until they overlap, and then extract the feature vector of the unified region.

The birth event information detected by the mitosis detection algorithm is used to establish hypotheses as follows. The last hypothesis regarding mitosis often produces a high likelihood of cell division although no mitosis occurs, e.g., when a lost cell from cell detection/tracking appears closely to another cell or more than one blob region are detected within one cell during segmentation. On the other hand, the likelihood may sometimes be too low even though mitosis occurs, e.g., when cell region segmentation fails during mitosis due to the changes in cell shape, size, and brightness and detects daughter cell regions after the cells move away from the birth event location. To resolve these confusions, we first explicitly detect birth events using the mitosis detection algorithm. For each birth event, we then find the nearest cell from the birth location and change its status as *potentially mitotic* in several following frames. The mitosis hypothesis is considered only for these potentially mitotic cells. The several frame delay is allowed because daughter cells are often attached to each other in several frames right after the

Hypotheses	p	C								X
9 → 0	0.1	0	0	0	1	0	0	0	1	0 or 1
9 → 6	0.3	0	0	0	1	0	0	1	0	0 or 1
9,8→6	0.8	0	0	1	1	0	0	1	0	0 or 1
8 → 6	0.5	0	0	1	0	0	0	1	0	0 or 1
7 → 4	0.3	0	1	0	0	1	0	0	0	0 or 1
7 → 5	0.3	0	1	0	0	0	1	0	0	0 or 1
7→ 4,5	0.9	0	1	0	0	1	1	0	0	0 or 1
0 → 4	0.2	1	0	0	0	1	0	0	0	0 or 1
Object ID:		in	7	8	9	4	5	6	out	
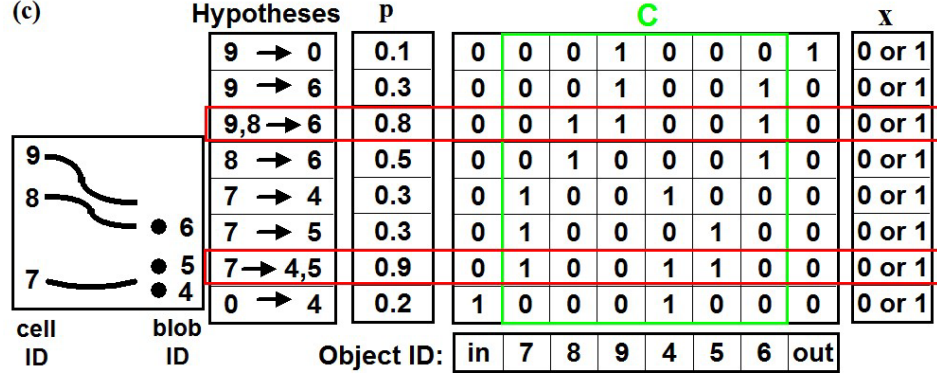
Figure 6.5: Example of our association problem and solution, where the optimal solution is highlighted by red boxes.

birth event; automated detection and segmentation methods can hardly separate individual cells in such a case.

After obtaining all hypotheses between two consecutive frames, we find the best combination of hypotheses as follows. Suppose that there are N_1 cells and N_2 blobs in the previous and current frames, respectively, and M hypotheses are established between the two frames. We build a matrix $C = [C_{ij}]$, which is an $M \times (N_1 + N_2)$ binary matrix where $C_{ij} = 1$ if and only if the i-th hypothesis is involved with the j-th element of the union of N_1 cells and N_2 blobs. We then solve the following integer programming problem.

$$\arg \max_{\mathbf{x}} \mathbf{p}^T \mathbf{x} \tag{6.7}$$

$$s.t. \ (C^T\mathbf{x})_i \leq 1 \quad \text{for} \quad i = 1, \cdots, N_1 + N_2$$

$$x_j \in \{0, 1\} \quad \text{for} \quad j = 1, \cdots, M$$

where $\mathbf{p}$ is an $M \times 1$ vector containing all the likelihoods and $(C^T\mathbf{x})_i$ is the i-th element of $C^T\mathbf{x}$. Solving this optimization problem yields an $M \times 1$ binary vector $\mathbf{x}$ where $x_i = 1$ indicates that the i-th hypothesis is selected as an element of the best combination. Note that each cell or blob can be selected at most once due to the constraint $(C^T\mathbf{x})_i \leq 1$.

Figure 6.5 shows a simple example of the integer programming problem with $M = 8$, $N_1 = 3$, and $N_2 = 3$. In this example, based on the optimal solution, blobs 4 and 5 are determined to

be newborn daughter cells and we assign new cell ids 4 and 5 with keeping the mother cell's id, which is 7, for lineage construction. In addition, blob 6 is determined to be a cluster with two cells with ids 8 and 9.

After the best association is found, if there are remaining cells in the previous frame, the cells are considered again for the association between the next two frames. In other words, the cells are assumed to be undetected in the current frame and expected to be detected in the following frame. If a track is continuously not linked with a cell for 10 frames, the track is eliminated. As to each of the remaining cells in the current frame, we investigate its neighboring cells. If there is a potentially mitotic cell nearby, the remaining cell is linked with the potentially mitotic cell as a daughter cell; otherwise, a temporary track initiates from the remaining cell. Each temporary track is confirmed as a real track after 10 frames if the track is linked with cells in most of the 10 frames.

6.1.2 Experiments

We evaluate our cell tracking method on 48 C2C12 myoblastic cell populations under four different culture conditions. We empirically show that our method significantly outperforms the method without having an explicit mitosis detection functionality as well as a state-of-the-art cell tracking method [74].

Data and Ground truth: During the growth of stem cells, phase contrast microscopy cell images were acquired every 5min using a Zeiss Axiovert T135V microscope (Carl Zeiss Microimaging, Thornwood, NY) equipped with a 5X, 0.15 N.A. phase contrast objective, a custom-stage incubator, and the InVitro software (Media Cybernetics Inc., Bethesda, MD). For training samples of birth events, one phase contrast microscopy image sequence of C2C12 cells consisting of 1013 images (approx. 84.4hrs) was acquired under control condition. For evaluation of tracking performance, twelve image sequences of C2C12 cells were acquired under each of four different conditions: control, FGF2, BMP2, and FGF2+BMP2; as a result, total 48 image
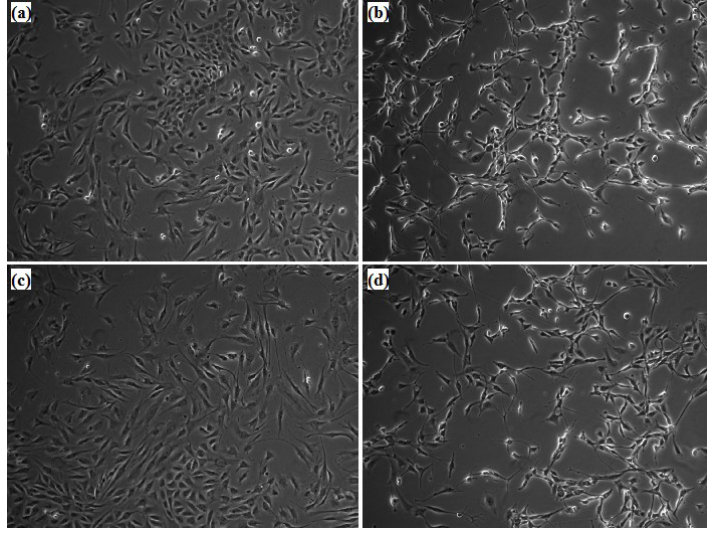
Figure 6.6: Sample images under four cell culture conditions. (a) Control, (b) FGF2, (c) BMP2, and (d) FGF2+BMP2.

sequences, each of which consists of 600 images (50hrs), were acquired. Each of these images contains 1392×1040 pixels with a resolution of 1.3μm/pixel. Figure 6.6 shows sample images from the four different cell culture conditions.

A model for birth event detection was trained with 673 birth events manually located in the first long C2C12 image sequence. In order to evaluate tracking performance, particularly precision, for each of 48 sequences, three cells were randomly selected in the initial frame and the cells and their progeny cells were manually tracked. For manual tracking, the center of each cell was marked. To measure recall, we fully annotated one sequence under BMP2 condition.

Evaluation: To measure the contribution of the mitosis detection to cell tracking, we compare the performances of two tracking systems: tracking systems without and with the mitosis detection. For the tracking system without mitosis detection, the hypothesis regarding mitosis is considered for every cell and a temporary track initiates from every remaining cell in the current frame after association due to the absence of information on mitosis occurrence and location.

For this comparison, we measure how much effort is required to obtain the perfect cell lineage tree from the lineage tree constructed by tracking algorithms; lineage tree construction is one of
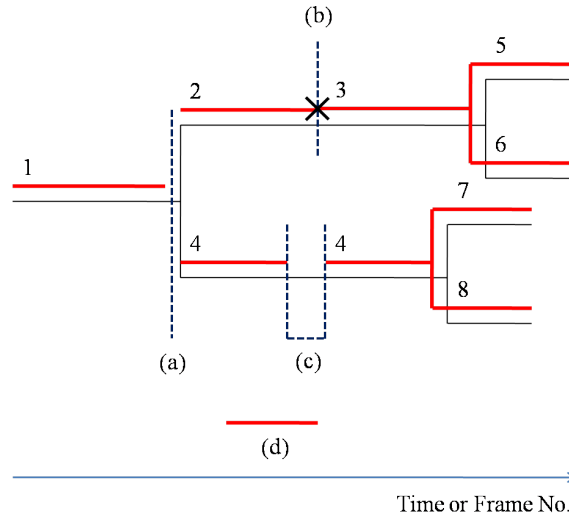
Figure 6.7: Illustration of four types of errors that need to be fixed to obtain the perfect lineage tree from tracking results: (a) missed mother-daughter relations (1-2 and 1-4), (b) switched track (from 2 to 3), (c) untracked frames (between two 4s), and (d) mistracked frames. The lineage tree consisting of black thin lines represents ground truth. The red thick lines above the ground truth lineage tree represent tracking results. The numbers above tracks indicate track ids. Among these errors, the errors (a) and (b) are related to mitosis detection.

the most important goals of cell tracking. To quantitatively calculate this effort, we consider four types of errors: missed mother-daughter relations, switched tracks, untracked frames, and mistracked frames. Figure 6.7 illustrates these four types of errors. To obtain the perfect cell lineage from tracking results, all of these errors are required to be fixed.

Among these errors, we count the occurrences of the first two errors, missed mother-daughter relations and switched tracks, since they are related to mitosis detection. If actual mitosis is not detected, the trajectory of the mother cell does not branch and thus the relation between mother-daughter cells is not captured. On the other hand, if mitosis is incorrectly detected when no mitosis occurs, the trajectory of the cell wrongly branches and thus the track of the cell is switched. When considering mother-daughter relations, we allow ten frame delay because the regions of two daughter cells are hard to be separately identified right after cell division. In other words, mother-daughter relations are considered to be missed if they are not discovered within ten frames after the daughter cells are born. The other two errors, untracked frames

123

and mistracked frames, are not relevant to mitosis detection, but to cell region detection and segmentation; thus, these errors remain regardless of mitosis detection. Since the objective of this comparison is to show the contribution of mitosis detection to cell tracking systems, we do not report these errors.

For the comparison against a state-of-the-art cell tracking method, we adopt more holistic criteria from radar tracking literature [13]: *target effectiveness* and *track purity*. Target effectiveness measures how effectively targets (cells) are followed by tracks; in other words, it penalizes undetected targets like recall. More formally, we first assign each cell i to its best track j that follows the cell for the longest time. Target effectiveness is then defined as

$$\text{Target Effectiveness} = \frac{\sum_i \text{ number of frames where cell } i \text{ is followed by track } j}{\sum_i \text{ number of frames where cell } i \text{ appears}} \quad (6.8)$$

In contrast, track purity measures how purely tracks follow targets; in other words, it penalizes false detection like precision. To compute track purity, we first assign each track j to its best target i that is followed by the track for the longest time (the roles of track and target are changed compared to the case of track effectiveness.). Track purity is then defined as

$$\text{Track Purity} = \frac{\sum_j \text{ number of frames where track } j \text{ follows cell } i}{\sum_j \text{ number of frames where track } j \text{ appears}} \quad (6.9)$$

Note that track purity can be measured only when the entire cells are manually tracked. Thus, we compute track purity on the fully annotated sequence; target effectiveness are computed on 16 sequences among 48 sequences, where three cells and their prodigy cells are manually tracked. For each of four culture conditions, the first four sequences are used for the experiments.

6.1.3   Results and Discussions

Comparison against the cell tracking method without having an explicit mitosis detection functionality: Cell tracking accuracy significantly increased after incorporating the birth event information provided by the mitosis detection algorithm; the numbers of missed mother-daughter

124
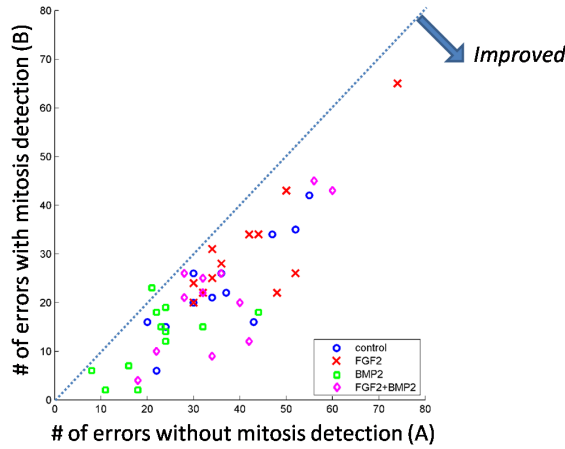
Figure 6.8: Tracking performance comparison between tracking systems without (x-axis) and with (y-axis) mitosis detection in terms of the numbers of missed mother-daughter relations (left) and switched tracks (right). The points below the diagonal lines indicate that tracking is improved through the mitosis detection. After the mitosis detection is incorporated, missed mother-daughter cell relations and switched tracks were reduced in 47 out of 48 sequences and in 37 out of 48 sequences, respectively.

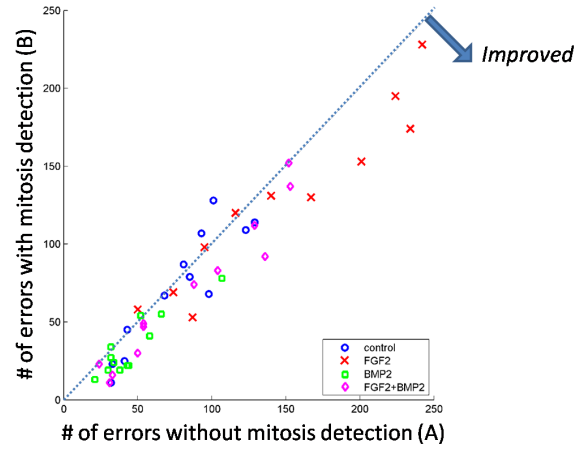relations and switched tracks were considerably reduced as shown in Figure 6.8 and Table 6.1. Compared to the tracking system without mitosis detection, the system with mitosis detection achieved on average 39%, 28%, 51%, and 46% improvements in detecting mother-daughter cell relations and 16%, 11%, 30%, and 26% improvements in reducing switched tracks for control, FGF2, BMB2, and FGF2+BMP2 conditions, respectively. In total, 42% and 21% improvements were achieved in terms of these two measures. The p-values obtained by ratio paired t-tests confirm that these improvements are statistically significant. The performance improvement in terms of missed mother-daughter relations is greater than that of switched tracks because tracking switching is only partially related to mitosis detection in that it can occur in other situations, such as cell overlapping.

The advantages of precise mitosis detection in cell tracking systems can be summarized as follows. First, precise mitosis detection reduces the numbers of undetected mitosis as well as mitosis candidates. Without mitosis detection, much more hypotheses regarding mitosis may

| Error (a): missed mother-daughter relation					
	Control	FGF2	BMP2	FGF2+BMP2	Total
Geometric mean of error ratios (B/A)	0.61	0.72	0.49	0.54	0.58
Geometric STD of error ratios (B/A)	1.37	1.23	1.87	1.60	1.58
p-value	0.0002	0.0001	0.0014	0.0006	<0.0000
Error (b): switched track					
	Control	FGF2	BMP2	FGF2+BMP2	Total
Geometric mean of error ratios (B/A)	0.84	0.89	0.70	0.74	0.79
Geometric STD of error ratios (B/A)	1.41	1.19	1.28	1.35	1.33
p-value	0.0560	0.0209	0.0003	0.0035	<0.0000

A: number of errors without mitosis detection, B: number of errors with mitosis detection

Table 6.1: Tracking performance comparison between tracking systems without and with mitosis detection in terms of the geometric mean and standard deviation(STD) of the error ratios. When the mitosis detection is incorporated, the number of missed mother-daughter relations was reduced on average by 39%, 28%, 51%, and 46%; the number of switched tracks by 16%, 11%, 30%, and 26% in control, FGF2, BMP2, and FGF2+BMP2 conditions, respectively; in total, 42% and 21% performance improvements were achieved in terms of the numbers of errors (a) and (b), respectively. The p-values obtained by ratio paired t-tests show that these performance improvements due to the mitosis detection is statistically significant.

be established, which degrades the efficiency of cell tracking systems, particularly when cells are clustered together. In addition, mitosis which is not captured by the association with the mitosis hypothesis can be detected in the track maintenance step if mitosis detection is involved. Second, mitosis detection is helpful to correctly identify a mitotic cell and the mother-daughter relations. Without mitosis detection, a neighboring cell is often determined as a mother cell particularly when the cell is in contact with one of the daughter cells; on the other hand, precise information on birth location identifies a real mitotic cell. Lastly, mitosis detection makes cell tracking more robust to incorrect segmentation. In segmentation, artifacts or parts of background are often detected as cell regions; in addition, one cell is sometimes detected by more than one cell region. If either case lasts for several frames, a mitosis hypothesis is generally considered
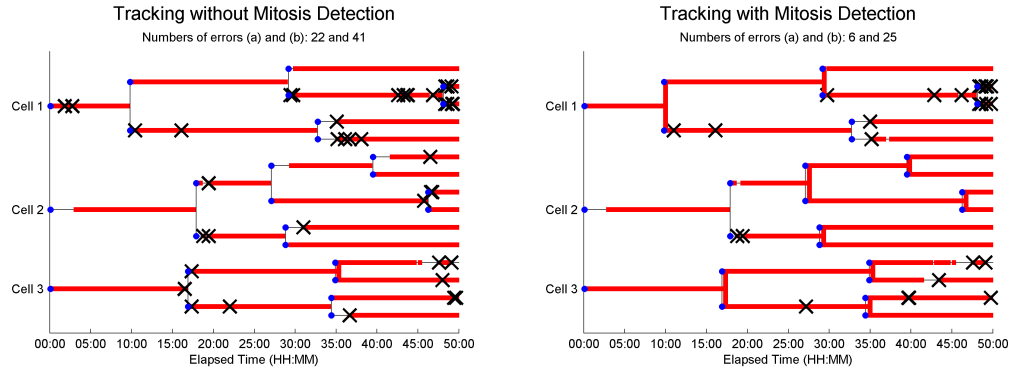
Figure 6.9: Lineage tree comparison between the tracking systems without (left) and with (right) the mitosis detection on the first C2C12 sequence under control condition. The thin black lineage trees are constructed by manual annotation. The red thick lines covering the ground truth lineage trees represent tracking results. Two types of errors were counted: (a) missed mother-daughter relation, a pair of which are shown as a vertical black line not covered with a red line, and (b) switched track, which is indicated by an X mark. These examples clearly show that the mitosis detection significantly reduces these two types of errors in cell tracking and lineage construction.
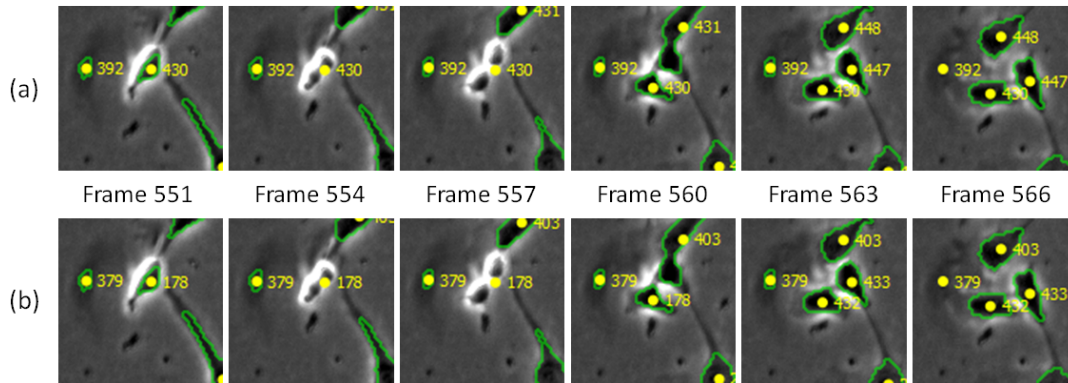
Figure 6.10: Example images illustrating cell tracking results of the tracking systems (a) without and (b) with mitosis detection. A birth event occurs at frame 557. After the birth event, the system without the mitosis detection incorrectly detects mother-daughter relations; between frames 560 and 563, cell 431 is detected as a mother cell and cells 447 and 448 as its daughter cells due to the incorrect segmentation at frame 560. Despite such a situation, the system with the mitosis detection correctly reveals the mother-daughter relation (cell 178 as a mother cell and cells 432 and 433 as its daughter cells) since the time and location of the birth event detected by the mitosis detection method are incorporated into the system.

with a high likelihood to handle additional cell regions. Mitosis detection avoids track switching by excluding the mitosis hypothesis in such situations.

	Target effectiveness	Track purity
Ours	0.82	0.93
Li et al. [73]	0.70	0.65

Table 6.2: Comparison of our system against a state-of-the-art cell tracking system [73] on a sequence with all cells manually tracked.

Culture condition	Algorithm	Exp1	Exp2	Exp3	Exp4	Average
Control	Ours	0.84	0.85	0.82	0.81	0.83
	[73]	0.69	0.70	0.76	0.65	0.70
FGF2	Ours	0.62	0.66	0.67	0.60	0.64
	[73]	0.56	0.67	0.57	0.48	0.57
BMP2	Ours	0.82	0.88	0.72	0.77	0.80
	[73]	0.70	0.71	0.61	0.55	0.63
FGF2+BMP2	Ours	0.80	0.76	0.78	0.82	0.79
	[73]	0.68	0.68	0.70	0.78	0.71

Table 6.3: The target effectiveness comparison between our method and a state-of-the-art method [73] on 16 cell populations under four different culture conditions.

The lineage tree in Figure 6.9(a) clearly demonstrates that undetected and incorrectly detected mitosis are major causes of tracking failure. The precise birth event detection reduces missed mother-daughter relations due to undetected mitosis as well as false branching due to incorrectly detected mitosis, resulting in more accurate tracking and lineage construction as shown in Figure 6.9(b). Figure 6.10 shows sample images illustrating the tracking results of the systems without and with mitosis detection. As shown in the figure, the tracking system with mitosis detection correctly reveals mother-daughter relations when another cell is located nearby and cell segmentation is incorrectly performed while the tracking system without mitosis detection fails.

When compared with a state-of-the-art cell tracking system, our system achieves higher track purity and target effectiveness on the fully annotated sequence and higher target effectiveness on the 16 sequences, as shown in Tables 6.2 and 6.3. These results again clearly show that
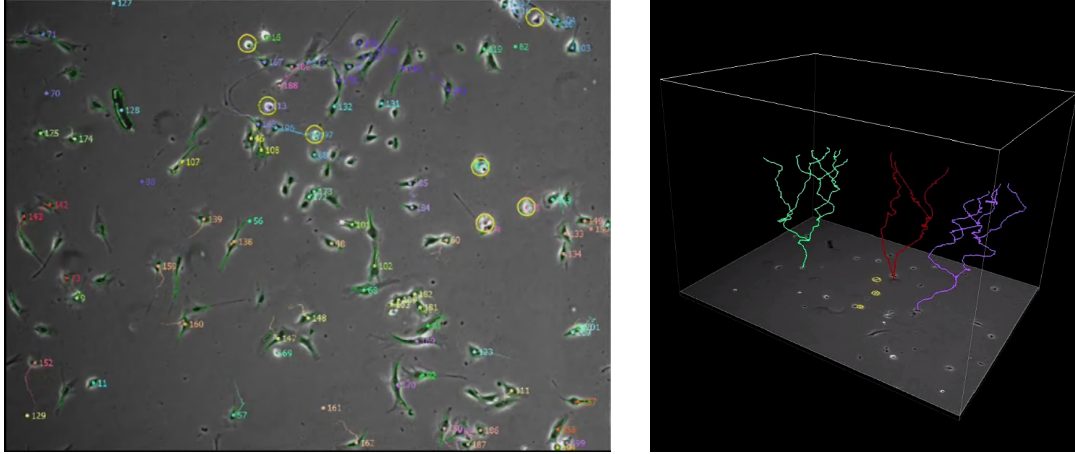
Figure 6.11: Cell tracking results shown in 2D (left) and 3D (left) space. Yellow circles enclose mitosis detected by our mitosis detection algorithm. Different colors and numbers represent different tracks.

mitosis detection is critical for cell tracking accuracy. Precisely detected mitosis can enhance both precision and recall by avoiding false branching and track switching. Figure 6.11 shows 2D and 3D view of cell tracking results generated by our cell tracking system.

6.2 Automated Analysis of Wound Healing Assays

In this section, we apply our cell tracking system introduced in the last section to an application of cell behavior analysis in wound healing assays in order to show the usefulness and effectiveness of our cell tracking system for biological research [12].

6.2.1 Wound Healing Assay

The wound healing assay is an easy and low-cost method to allow for observing cell migration *in vitro* [75]. In this assay, cells are first grown to form a confluent monolayer *in vitro*. An artificial wound is generated by scratching and displacing a group of cells at the center as shown in Figure 6.12, and then the healing process is monitored while neighboring cells fill in the wound area as shown in Figure 6.13. This healing process takes 3 to 24 hours, depending on cell types and culture conditions. The healing process is captured into time-lapse microscopy images for

129
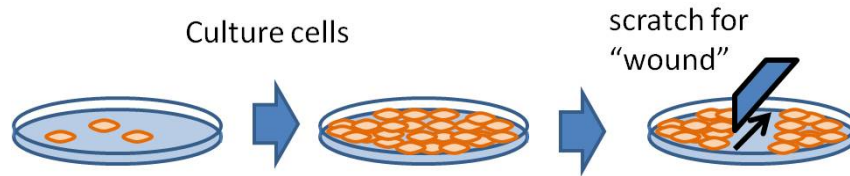
Figure 6.12: The process of making wound.
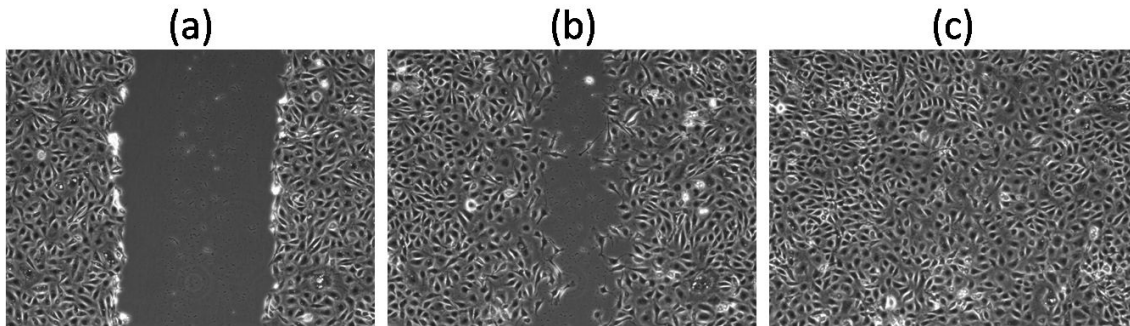
Figure 6.13: Example images of a wound healing process: (a) the initial image on the healing process. (b) an image at which cells move to the wound area. (c) an image at which cells fill the wound area.

the analysis of cell behavior during the process.

Analysis of wound healing assays is a popular research topic in biology. For example, Liang et al. [75] compared several migration assays *in vitro* to find out which wound healing assay best mimics cell migration *in vivo*. Yarrow et al. [132] measured the healing speed by observing the size change of the wound area in order to analyze the wound healing capability of different culture conditions. Abbi et al. [1] analyzed cell migration paths to assess the effects of expression of exogenous genes on the migration of individual cells. Nikolić et al. [96] manually tracked cell migration in wound healing assay in order to understand how multiple cells execute highly dynamic and coordinated movements during the healing process. For further analysis, more detailed measurements of the cell behaviors are required; however, often manual tracking or labeling is too cumbersome or even intractable, so there are high needs for automated cell tracking systems.
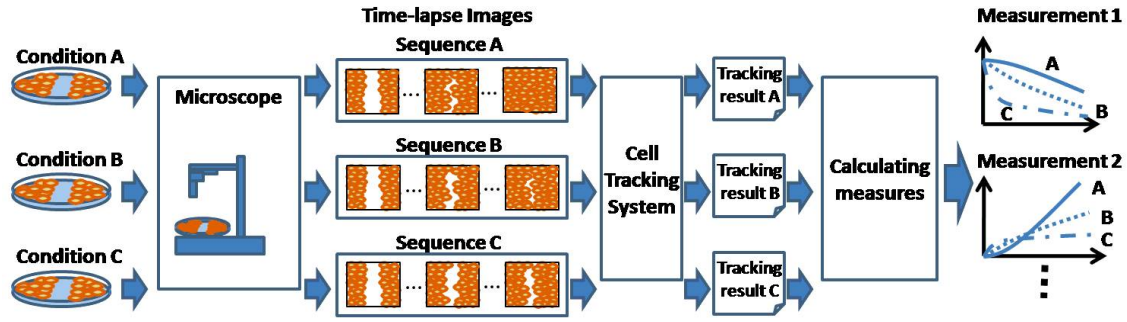
Figure 6.14: Workflow of our wound healing assay experiments under three culture conditions.

6.2.2 Experiments

Figure 6.14 shows the overall workflow of our experiments for the analysis of wound healing assays. First, the culture dishes with a wound area were prepared under difference types of culture conditions. Each dish was monitored by a microscope; as a result, a time-lapse image sequence was generated for each cell population. As the image sequences as input, our tracking system tracked individual cells, and based on the tracking results, various measurements that characterize cell behavior were calculated.

Cell Culture Conditions and Imaging Modality: After bovine aortic endothelial cells (BAEC) were cultured in a dish to form a confluent monolayer, a group of cells at the center of the dish were scratched and displaced. Then different amounts of medicine Latrunculin B, which interferes with cellular activity, were added to three different dishes:

- Condition A : control (no medicine)

- Condition B : 10nM of Latrunculin B

- Condition C : 100nM of Latrunculin B

The wound area was monitored with a Leica DMI 6000B inverted microscope using a 10X objective with phase optics until the area was completely filled with cells. Images were acquired every 5 minutes for 17 hours using a 12-bit CCD camera. Each image consists of 1040×1392 pixels.

131
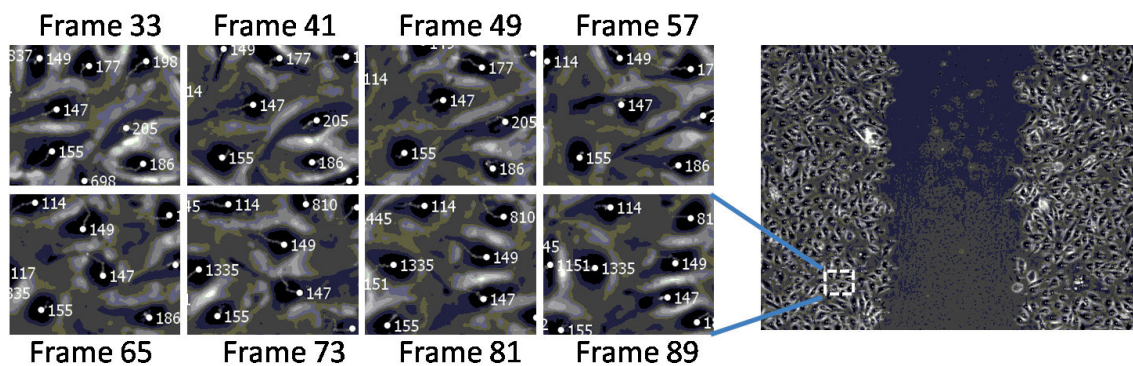
Figure 6.15: Cell tracking results on an input image sequence.

Cell Tracking: We applied our automated cell tracking method to the time-lapse phase contrast microscopy images. Figure 6.15 shows an example of the tracking results. As can be seen in the figure, the tracking system assigned a positive integer ID on each cell as its unique identifier. Each cell also kept its mother cell's ID for maintaining its lineage information. In addition, for each cell, a set of descriptors were computed at each frame, including its centroid position and contour information using chain code. Based on this information, various cell behavior measurements, such as cell confluence and cell migration speed/direction, were computed.

6.2.3 Results

We computed several measurements of cell behavior—cell density, cell migration speed, and cell migration direction.

Cell Density: Figures 6.16 and 6.17 show how the cell density changed over time and location. Since cells generally migrate horizontally, the cell density at a position in the density map was computed over a narrow vertical window of width 40 pixels ($36.5 \mu m$) as shown in Figure 6.17(a). As can be seen in Figure 6.17(b-d), the cell densities under conditions A and B show similar change patterns; at frame 200, both the wound areas were filled with cells and showed similar cell density to other area. On the other hand, the cells under condition C migrated more slowly, and thus the cell density in the wound area was low at the end of the image sequence.

132
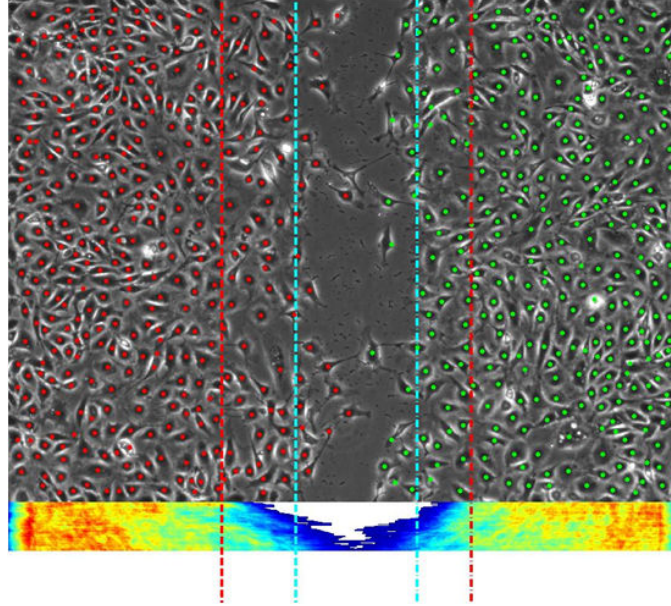
Figure 6.16: Cell density map over time along with tracking results. In the density map, the top row shows the cell density at the initial frame and the bottom row demonstrates the cell density at the current frame. (The density map keeps growing to the bottom as time goes on.) Red and blue colors represent high and low densities, respectively, in the density map. Red dashed lines indicate the front line that precedes 95% of cells at the initial frame, while blue dashed lines indicate the front line at the current frame.
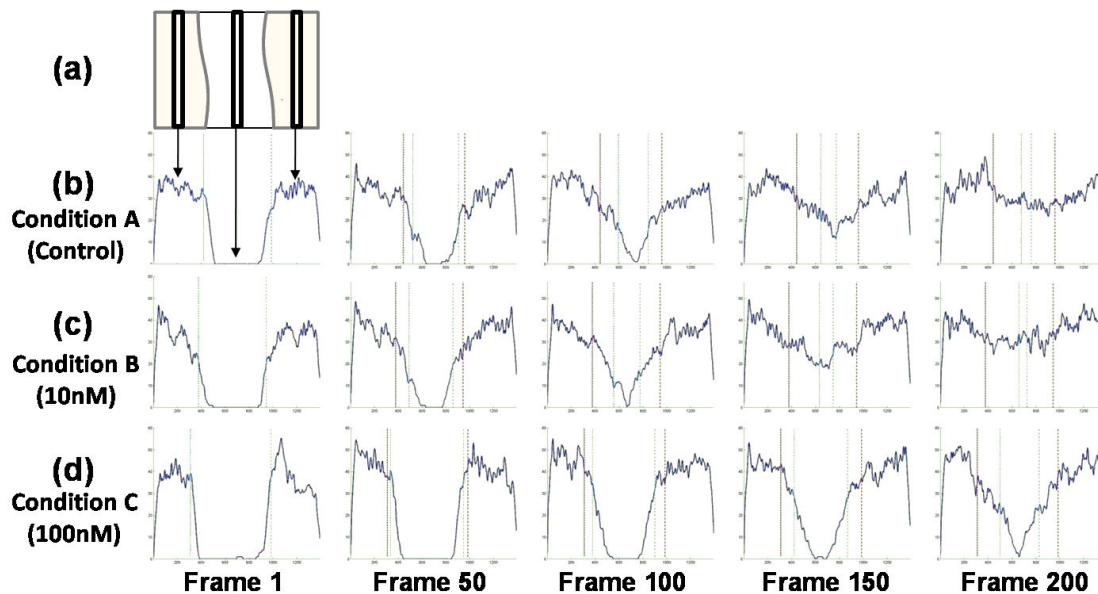
Figure 6.17: Space-time transition of cell density.
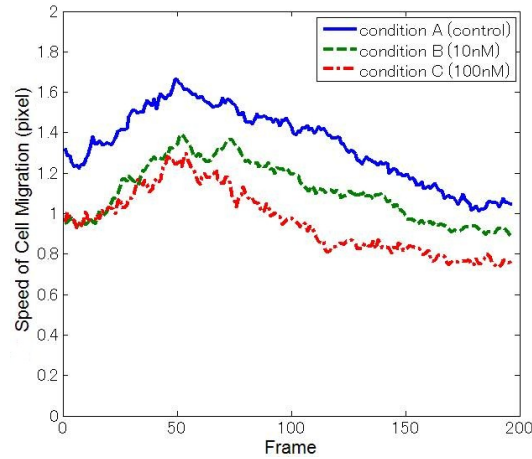
Figure 6.18: The average speed of cell migration over time.
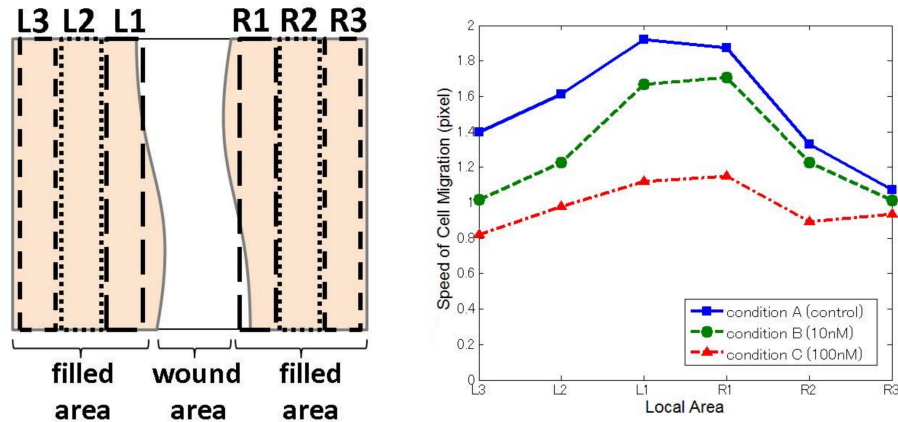
Figure 6.19: Local area division (left) and the average speed of cell migration at each local area (right).

Cell Migration Speed: Figure 6.18 shows that the cell migration speed under the condition A is consistently higher than those in the other conditions, and the speed under the condition C is the lowest. Interestingly, all the migration speeds increase up to frame 50 and then they continuously decrease.

It is conceivable that the speed of cell migration depends on the distance from the wound area. To verify whether this is the case, the filled area (i.e., the left and right sides of the wound area) is divided into six local areas as shown in Figure 6.19: L1, L2, and L3 at left side from the 95% frone line (the line that precedes 95% of cells) to the very left of the field of view, and R1,
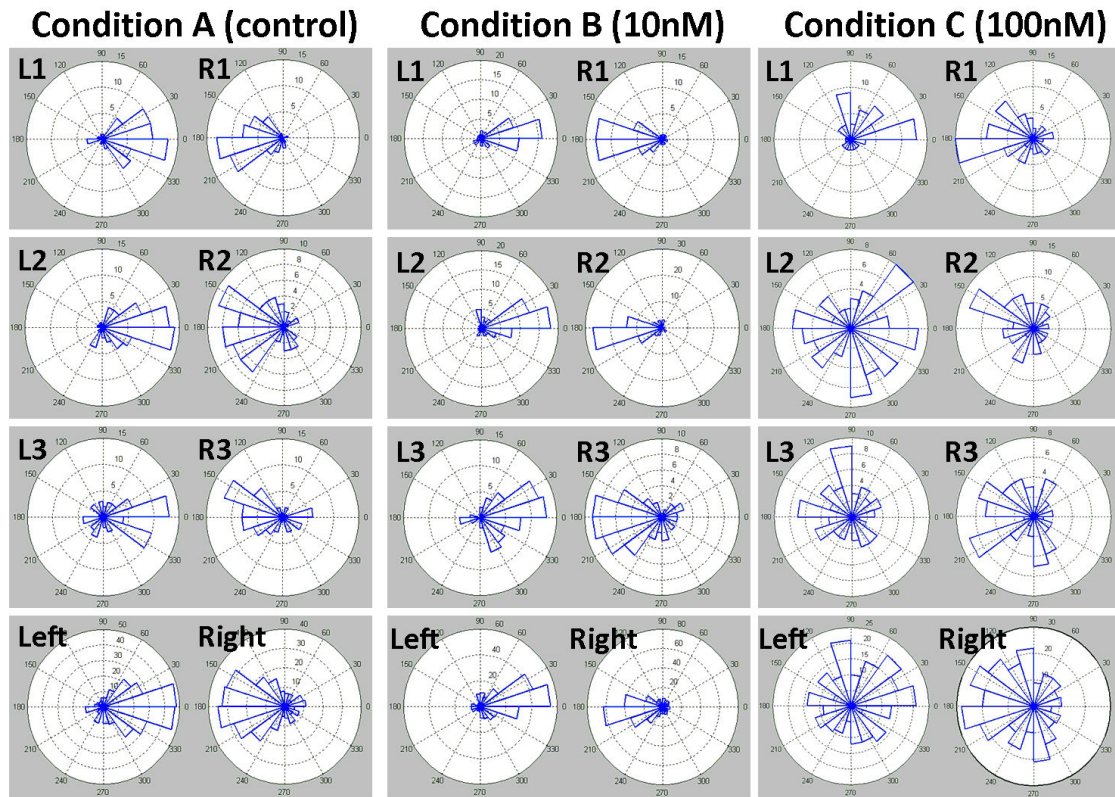
Figure 6.20: Rose diagrams of cell migration directions. The first three rows show the distributions of cell migration directions at each local area. The last row shows the distributions at the entire left and right filled areas.

R2, and R3 at the right side in the same way. Note that as cells migrate toward the center, these local areas are also expanded toward the center. As shown in Figure 6.19, understandably cells move slower as getting farther from the wound area.

Cell Migration Direction: To quantitatively analyze the direction of cell migration, the distribution of cell migration directions under each condition was plotted using a rose diagram (angular histogram) as shown in Figure 6.20. As can be seen in the figure, cells tend to migrate toward the wound area regardless of their locations. Such tendency is strong under conditions A and B, but weak under condition C. Cell migrations in L1 and R1, the closest local areas to the wound area, are the most highly directional to the wound.

Figure 6.21 shows the relationship between migration direction and density slope, or density change, along the horizontal axis; i.e., a positive density slope at some position indicates that cell

135
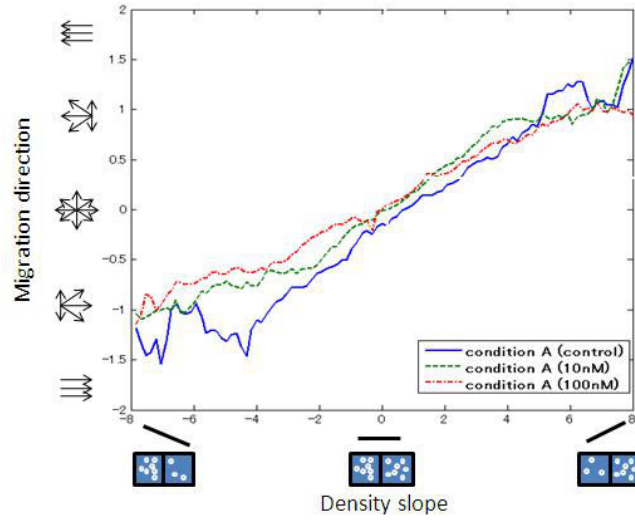
Figure 6.21: The relationship between density slope and migration direction. Density slope means cell density change along with horizontal axis; i.e., a positive density slope at some position indicates that cell density is higher on its right side than its left side.

density is higher on its right side than its left side. As shown in the figure, cells tend to move from high density area to low density area. In the area that shows almost uniform density, cell migration direction is also almost non-directional.

6.3 Summary of Cell Tracking

We have proposed a cell tracking system that incorporates mitosis detection functionality and emprically demonstrated that the information on mitosis occurrence and timing can significantly improve cell tracking accuracy and cell lineage quality. In addition, we applied our cell tracking system to the analysis of cell behavior in wound healing assays and reported the quantitative measurements on cell density, cell migration speed, and cell migration direction.

Our contribution to cell tracking can be summarized as follows:

- We empirically verified that mitosis is important for cell tracking and thus it should be carefully taken into account in cell tracking systems.

- We introduced 48 time-lapse phase contrast microscopy image sequences with partial man-

ual annotation on cell tracking and performed cell tracking on the data and reported cell tracking accuracy. Since such an extensive test has never been performed, our data and results would be a good benchmark for cell tracking.

- We demonstrated that vision-based cell tracking can provide quantitative information on cell behavior in time-lapse microscopy without staining or GFP-tagging and thus has potential to contribute to biological and biomedical research.

Chapter 7

Discussions and Conclusions

In the previous chapters, we have introduced the task of automated cell behavior analysis in non-flueorescent microscopy, and in order to take a step toward achieving the goal, we have proposed computer vision algorithms for detection of three cellular events—mitosis (cell division), apoptosis (programmed cell death), and differentiation—and tracking of cells. Through various experiments, we have also demonstrated that our current system, which includes all celluar detection and cell tracking methods, can effectively and efficiently detect cellular events, track individual cells, and compute biological measurements that can be useful for research in biology.

In this last chapter, we discuss the limitations of our current system and present several ideas to improve or extend the system in Section 7.1, followed by conclusions in Section 7.2

7.1   Discussions and Future Directions

Although our system effectively performs cellular event detection and cell tracking, it has limitations. This chapter discusses several ways to improve and extend the current system.

7.1.1   Detection of Cellular Event as a Process

Currently, cellular event detection is performed by detecting the most noticeable moment of the event (for mitosis and apoptosis) or altered states at one time point (for differentiation). More specifically, for mitosis detection, we detect the completion of mitosis, which is typically visualized as a figure eight shape; for apoptosis detection, we detect the initiation or completion of apoptosis when cells begin to shrink and become bright or show a stationary state after cell death; for differentiation detection, we detect the area occupied by differentiated cells at one time point. Such a strategy to represent cellular events by a phenomenon at a time and location makes the problem and evaluaion clearer and more straightforward without losing most of the important information on cell behavior; i.e., critical information for cell behavior analysis, such as cell lineage information, the total number of cells, and the portion of differentiated cells, is still obtainable by detecting cellular events with our definitioins.

One may wonder what benefits would be gained if a cellular event is detected as a process as it is, i.e., celluar event detection is performed by locating both the starting and ending timings of the event and tracking the cell's position and apperance change during the event. This additional information will provide more quantitative measurements, e.g., the duration of mitosis/apoptosis, mitotic/apoptosis index, which is the ratio of the number of mitotic/apoptotic cells to the total number of cells, cell region growing speed during a muscle myotube forming process, etc. In addition, cell status will be more precisely classified by additionally specifying mitotic and apoptotic cells. Unfortunately, along with the benefits, the problem complexity will also increase. First, deteching the starting or ending timing of an event may not be simple since both the timings may not be prominent. For example, mitosis begins with cell shrinkage, but often the area change is too subtle for even human to notice the change in microscopy with a magnification of 5X. Second, tracking cells during the process of an event is not easy as cells undergoing an event typically show significant change in appearance and brightness. Furthermore, labeling and evaluation would be more complicated since manual annotation needs to be conducted on several

consecutive frames for each event and often only part of an event process would be detected.

7.1.2   Construction of a Unified System

One of our future goals is to construct a unified cell tracking system that incorporates all celluar event detection functionalities. (Currently, our cell tracking system integrates only with mitosis detection.) As we demonstrated in Section 6.1, our cell tracking system shows synergy with mitosis detection. For example, precisely detected mitosis helps the cell tracking system to accurately reveal mother-daughter cell relationship and based on which several measurements, such as cell cycle length, can be more accurately calculated. Note that these benefits can be gained only when cell tracking and mitosis detection functionalities are incorporated into one system. In the same manner, integrating apoptosis and differentiation detection functionalities into the cell tracking system will bring more synergy. Specifically, in the unified system, apoptosis detection can terminate the lineage of a dead cell or change the cell's status to *dead*; based on the information, a lot of measurememts, such as the number of (living) cells or the portion of living cells to dead cells, can be more accurately computed. Differentiation detection helps specify when cell differentiation starts and how it progresses for indivisual cells in the unified system. With such information, it would also be interesting to investigate when cell fates are determined, by tracing back cell lineage to the cell all of whose descendants are differentiated into the same cell type.

7.1.3   Increase of Usability of the System

We aim at not only developing effective computer vision algorithms for cell behavior analysis, but also providing the unified cell tracking system for researchers in biological sciences and biomedical engineering. To achieve this goal, it is critical to increase the usability of our system in order for the real users to conviniently use it.

Figure 7.1 shows our ongoing effort toward the goal. This mitosis annotation and correction tool provides an intuitive graphical user interface for mitosis labeling on the original time-lapse

141
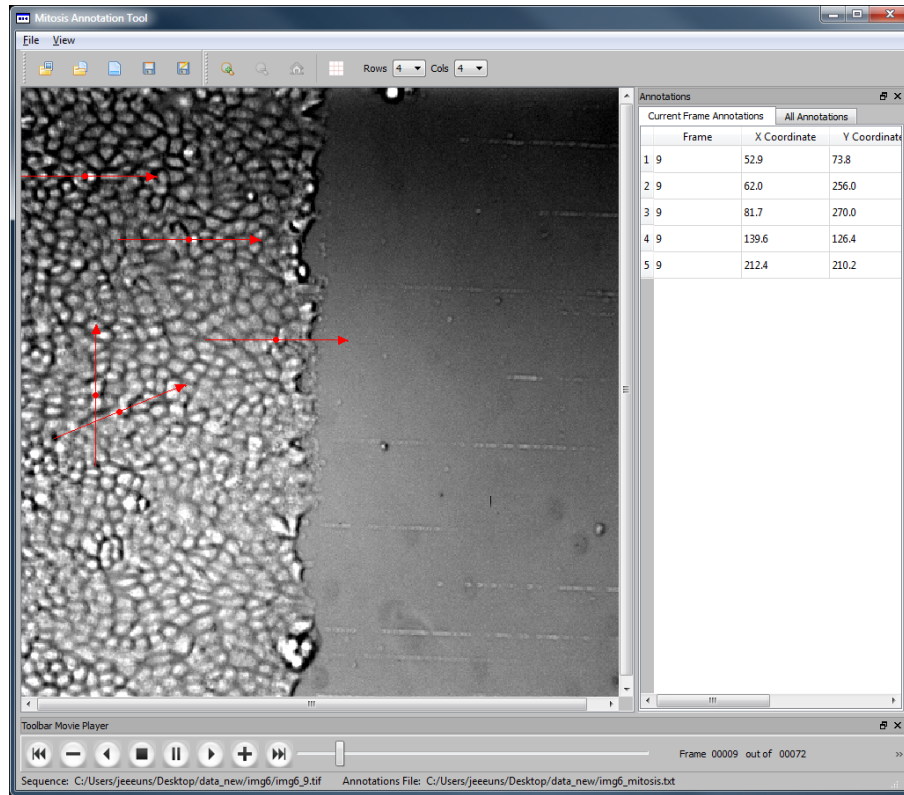
Figure 7.1: Mitosis annotation and correction tool. This tool is used for mitosis labeling in order to obtain sample data for mitosis model training. This tool can also be used for correction of detected mitosis after performing automated mitosis detection.

images and correction on the mitosis detection result. We are planning to integrate the implementation of the proposed mitosis detection algorithm into this tool, constructing a complete mitosis detection module, as a part of our unified system.

7.1.4 Interactive System for Cell Image Analysis

Despite the advantage of automated vision-based systems for cell behavior analysis, such systems have not been popularly used for biology research yet. The major reasons are three-fold. First, the level of accuracy falls short of manual annotation, which most of biologists currently conduct for their research. Second, automated analysis is often not consistent with the change in cell type, cell culture conditon, and microscopy image quality. Third, it is difficult to verify what is

discovered by the automated system; for detection tasks, mis-detected samples (false positives) can be elliminated by manual examination, but undetected samples (false negatives) may not be easily recovered without conducting the whole process of manual annotation.

To address these issues, we plan to develop an interactive system that adopts an online learning framework. Specifically, given a few samples that manually annotated, over them an initial model is learned. Based on the model, the system suggests a few more samples to be annotated, the labels of which can boost the accuracy of the model. As this process is repeated, the system eventually learns an accurate model for the target task with a high chance. We believe that the future of cell behavior analysis, more generally bioimage analysis, is in such an interative system.

7.2   Conclusions

In this thesis, we have proposed computer vision algorithms for detection of three cellular events—mitosis (cell division), apoptosis (programmed cell death), and differentiation—and tracking of cells in phase contrast microscopy, without involving any fluorescent labels. For event detection, we properly defined each event and presented a framework that consists of candidate detection, temporal information incorporation, and candidate validation. For candidate validation for different tasks, we developed two probabilistic temporal models for event detection and adopt a semi-supervised learning framework. We also presented a way to improve phase contrast microscopy by investigating the image formation process in a phase contrast mircoscope. For cell tracking, we proposed a system that intergrates mitosis detection functionality, which is performed independently of cell tracking. Through extensive experiments, we demonstrated that our tracking system outperforms previous cell tracking systems. In addition, we applied the system to an application of cell behavior analysis in would healing assays and showed that our system can produce quantitative cell behavior measurements with minimal human intervention. As huge amount of image data have been generating in biological and biomedical sciences and

consequently the analysis of the images becomes a great bottleneck in the fileds, our work would

be a step toward an automated system that can address the challenge.

Bibliography

[1] S. Abbi, H. Ueda, C. Zheng, L.A. Cooper, J. Zhao, R. Christopher, and J.-L. Guan. Regulation of focal adhesion kinase by a novel protein inhibitor fip200. *Mol. Biol. Cell*, 13(9): 3178–3191, 2002. 6.2.1

[2] O. Al-Kofahi, R.J. Radke, S.K. Goderie, Q. Shen, S. Temple, and B. Roysam. Automated cell lineage construction: A rapid method to analyze clonal development established with murine neural progenitor cells. *Cell Cycle*, 5(3):327–335, 2006. 2.1.1, 2.4.1

[3] National Center for Biotechnology Information (U.S.) American Cancer Society. *Holland-Frei Cancer Medicine*. B.C. Decker Publisher, 6th edition, 2000. 1

[4] M. Arulampalam, S. Maskell, N. Gordon, and T. Clapp. A tutorial on particle filters for online nonlinear/non-gaussian bayesian tracking. *IEEE Trans. on Signal Processing*, 50 (2):174–188, 2002. 2.4.1

[5] T.J. Atherton and D.J. Kerbyson. Size invariant circle detection. *Image and Vision Computing*, 17:795–803, 1999. 3.3.1

[6] M. Baker. Cellular imaging: Taking a long, hard look. *Nature*, 466(7310):1137–1140, 2010. 1

[7] B. Benfold and I.D. Reid. Stable multi-target tracking in real-time surveillance video. In *Proc. IEEE Conference on Computer Vision and Pattern Recognition*, pages 3457–3464, 2011. 1.2

[8] A. Bennett, H. Osterberg, H. Jupnik, and O. Richards. *Phase Microscopy: Principles and Applications*. John Wiley and Sons, Inc., New York, 1951. 1.2

[9] T. Bernas, J.P. Robinson, E.K. Asem, and B. Rajwa. Loss of image quality in photobleaching during microscopic imaging of fluorescent probes bound to chromatin. *Journal of Biomedical Optics*, 10(6):064015, 2005. 1.1

[10] E. Betzig, G.H. Patterson, R. Sougrat, O.W. Lindwasser, S. Olenych, J.S. Bonifacino, M.W. Davidson, J. Lippincott-Schwartz, and H.F. Hess. Imaging intracellular fluorescent proteins at nanometer resolution. *Science*, 3(13):1642–1645, 2006. 1.1

[11] R. Bise, K. Li, S. Eom, and T. Kanade. Reliably tracking partially overlapping neural stem cells in dic microscopy image sequences. In *Proc. International Conference on Medical Image Computing and Computer Assisted Intervention Workshop*, pages 67–77, 2009. 6.1.1

[12] R. Bise, T. Kanade, Z. Yin, and S. Huh. Automatic cell tracking applied to analysis of cell migration in wound healing assay. In *Proc. IEEE Engineering in Medicine and Biology Society*, pages 6174–6179, 2011. 6.2

[13] S. Blackman and R. Popoli. *Design and analysis of modern tracking systems*. Artech House, 1999. 6.1.2

[14] M.V. Boland and R.F. Murphy. Automated analysis of patterns in fluorescence mircoscopy images. *Trends Cell Biol.*, 9:201–202, 1999. 1.1

[15] F. Bourgeois and J. Lassalle. An extension of the munkres algorithm for the assignment problem to rectangular matrices. *Communications of the ACM*, 14(12):802–806, 1971. 3.3.1

[16] J. Bozzola and L.D. Russell. *Electron Microscopy*. Jones & Bartlett Publishers, 2nd edition, 1999. 1, 1.1

[17] T. Brox, Y. Kim, J. Weickert, and W. Feiden. Fully-automated analysis of muscle fiber

images with combined region and edge-based active contours. In *In Bildverarbeitung f́ur die Medizin*, pages 86–90, 2006. 5.2.3

[18] A. Chebira, Y. Barbotin, C. Jackson, T. Merryman, G. Srinivasa, R.F. Murphy, and J. Kova. A multiresolution approach to automated classification of protein subcellular location images. *BMC Bioinformatics*, 8:210, 2007. 1.1

[19] X. Chen, X. Zhou, and S.T. Wong. Automated segmentation, classification, and tracking of cancer cell nuclei in time-lapse microscopy. *IEEE Trans. Biomed. Eng.*, 53(4):762–766, 2006. 1.1

[20] B. Coifman, D. Beymer, P. McLauchlan, and J. Malik. A real-time computer vision system for vehicle tracking and traffic surveillance. *Transportation Research Part C: Emerging Technologies*, 6(4):271–288, 1998. 1.2

[21] D. Comaniciu, V. Ramesh, and P. Meer. Real-time tracking of non-rigid objects using mean shift. In *Proc. Computer Vision and Pattern Recognition*, pages 673–678, 2000. 2.4.1

[22] N. Dalal and B. Triggs. Histograms of oriented gradients for human detection. In *Proc. IEEE Conference on Computer Vision and Pattern Recognition*, pages 886–893, 2005. 1.2, 3.1.1

[23] O. Debeir, P. Van Ham, R. Kiss, and C. Decaestecker. Tracking of migrating cells under phase-contrast video microscopy with combined mean-shift processes. *IEEE Trans. Med. Imaging*, 24(6):697–711, 2005. 2.1.1, 2.4.1

[24] O. Debeir, V.Mégalizzi, N. Warzée, R. Kiss, and C. Decaestecker. Videomicroscopic extraction of specific information on cell proliferation and migration *in virto*. *Exp. Cell Res.*, 314(16):2985–2998, 2008. 2.1.1

[25] C. Decaestecker, O. Debeir, P. Van Ham, and R. Kiss. Can anti-migratory drugs be screened in vitro? a review of 2d and 3d assays for the quantitative analysis of cell migra-

tion. *Med. Res. Rev*, 27(2):149–176, 2007. 2.4

[26] F. Dellaert and C. Thorpe. Robust car tracking using kalman filtering and bayesian templates. In *Conference on Intelligent Transportation Systems*, 1997. 2.4.1

[27] W. Denk, J.H. Strickler, and W.W. Webb. Two-photon laser scanning fluorescence microscopy. *Science*, 248(4951):73–76, 1990. 1.1

[28] N.J. Dimmock, A. Easton, and K. Leppard. *Introduction to Modern Virology*. Blackwell Publishing, 6th edition, 2007. 1

[29] L.A. DiPietro and A.L. Burns. *Wound Healing: Methods and Protocols. Methods in Molecular Medicine*. Totowa, N.J. Humana Press, 2003. 1

[30] R. Dixit and C. Richard. Cell damage and reactive oxygen species production induced by fluorescence microscopy: effect on mitosis and guidelines for non-invasive fluorescence microscopy. *The Plant Journal*, 36:280–290, 2003. 1.1

[31] J.W. Dobrucki, D. Feret, and A. Noatynska. Scattering of exciting light by live cells in fluorescence confocal imaging: Phototoxic effects and relevance for frap studies. *Biophysical Journal*, 93:1778–1786, 2007. 1.1

[32] D. Dormann, T. Libotte, C.J. Weijer, and T. Bretschneider. Simultaneous quantification of cell motility and protein-membrane-association using active contours. *Cell Motil. Cytoskel.*, 52(4):221230, 2002. 2.4.1

[33] J.F. Dorn, G. Danuser, and G. Yang. Computational processing and analysis of dynamic fluorescence image data. *Methods Cell Biol.*, 85(4):497–538, 2008. 1.1

[34] A. Doucet, N. de Freitas, and N. Gordon. *Sequential Monte Carlo Methods*. New York: Springer-Verlag, 2001. 2.4.1

[35] A. Dufour, V. Shinin, S. Tajbakhsh, N. Guillen-Aghion, J.-C. Olivo-Marin, and C. Zimmer. Segmenting and tracking fluorescent cells in dynamic 3-d microscopy with coupled active surfaces. *IEEE Trans. Image Process.*, 14(9):1396–1410, 2005. 2.4.1

[36] O. Dzyubachyk, W.A. van Cappellen, J. Essers, W.J. Niessen, and E. Meijering. Advanced level-set-based cell tracking in time-lapse fluorescence microscopy. *IEEE Trans. Med. Imaging*, 29(3):852–867, 2010. 2.4.1

[37] N.R. El-kholany, M.H. Abielhassan, A.E. Elembaby, and O.M. Maria. Apoptotic effect of different self-etch dental adhesives on odontoblasts in cell cultures. *Arch. Oral. Biol.*, 57 (6):775–783, 2011. 2.2

[38] K.W. Eliceiri, M.R. Berthold, I.G. Goldberg, L. Ibanez, B.S. Manjunath, M.E. Martone, R.F. Murphy, H. Peng, A.L. Plant, B. Roysam, N. Stuurman, J.R. Swedlow, P. Tomancak, and A.E. Carpenter. Biological imaging software tools. *Nature Method*, 9(7):697–710, 2012. 1

[39] S. Eom, R. Bise, and T. Kanade. Detection of hematopoietic stem cells in microscopy images using a bank of ring filters. In *Proc. IEEE International Symposium on Biomedical Imaging*, pages 137–140, 2010. 3.3.1

[40] L. Fang, N. Yang, J. Ma, Y. Fu, and G.S. Yang. microrna-1301-mediated inhibition of tumorigenesis. *Oncol. Rep.*, 27(4):923–934, 2011. 2.2

[41] Z. Fanti, M.E. Martinez-Perez, and F.F. De-Miguel. Neurongrowth, a software for automatic quantification of neurite and filopodial dynamics from time-lapse sequences of digital images. *Dev. Neurobiol.*, 71(10):870–881, 2011. 2.3.1

[42] Y. Freund and R.E. Schapire. A decision-theoretic generalization of on-line learning and an application to boosting. *J. Comput. Syst. Sci.*, 55(1):119–139, 1997. 2.1.1

[43] Y. Fuchs and H. Steller. Programmed cell death in animal development and disease. *Cell*, 147(4):742–758, 2011. 2.2

[44] R.I. Ghauharali and G.J. Brakenhoff. Fluorescence photobleaching-based image standardization for fluorescence microscopy. *Journal of Microscopy*, 198:88–100, 2001. 1.1

[45] S. Gu and J. He. Daphnoretin induces cell cycle arrest and apoptosis in human osteosar-

coma (hos) cells. *Molecules*, 17(1):598–612, 2012. 2.2

[46] A. Gunawardana, M. Mahajan, A. Acero, and J.C. Platt. Hidden conditional random fields for phone classification. In *Proc. Interspeech*, pages 1117–1120, 2005. 3.1.2

[47] A.J. Hand, T. Sun, D.C. Barber, D.R. Hose, and S. Macneil. Automated tracking of migrating cells in phase-contrast video microscopy sequences using image registration. *J. Microsc.*, 234(1):62–79, 2008. 2.4.1

[48] C. Harris and M. Stephens. A combined corner and edge detector. In *Proceedings of the 4th Alvey Vision Conference*, pages 147–151, 1988. 1.2

[49] S. W. Hell. Toward fluorescence nanoscopy. *Nat. Biotechnol.*, 21(11):1347–1355, 2003. 1.1

[50] D. House, M.L. Walker, Z. Wu, J.Y. Wong, and M. Betke. Tracking of cell populations to understand thier spatio-temporal behavior in response to physical stimuli. In *Proc. IEEE Conference on Computer Vision and Pattern Recognition Workshop on Mathematical Methods in Biomedical Image Analysis*, pages 186–193, 2009. 2.4.1

[51] S. Huh and M. Chen. Detection of mitosis within a stem cell population of high cell confluence in phase-contrast microscopy images. In *Proc. IEEE Conference on Computer Vision and Pattern Recognition*, pages 1033–1040, 2011. 3.2

[52] S. Huh, S. Eom, R. Bise, Z. Yin, and T. Kanade. Mitosis detection for stem cell tracking in phase-contrast microscopy images. In *Proc. IEEE International Symposium on Biomedical Imaging*, pages 2121–2127, 2011. 4.1.2, 6.1

[53] S. Huh, D.F.E. Ker, R. Bise, M. Chen, and T. Kanade. Automated mitosis detection of stem cell populations in phase-contrast microscopy images. *IEEE Trans. Med. Imaging*, 30(3):586–596, 2011. 3.1

[54] S. Huh, S. Eom, D.F.E. Ker, L.E. Weiss, and T. Kanade. Mitosis detection of hematopoietic stem cell populations in time-lapse phase-contrast microscopy images. In *Proc. IEEE*

International Symposium on Biomedical Imaging, pages 390–393, 2012. 3.3

[55] S. Huh, D.F.E. Ker, H. Su, and T. Kanade. Apoptosis detection for adherent cell populations in time-lapse phase-contrast microscopy images. In *Proc. International Conference on Medical Image Computing and Computer Assisted Intervention*, pages 331–339, 2012. 4.1

[56] S. Huh, M. Chen, H. Su, and T. Kanade. Diffraction pattern filtering of phase contrast microscopy images for an application of automatic muscle myotube detection. Submitted to a conference, 2013. 5

[57] K.M. Jansen and G.K. Pavlath. Molecular control of mammalian myoblast fusion. *Methods Mol. Biol.*, 475:115–133, 2008. 5.2.3

[58] T. Joachims. *Making large-Scale SVM Learning Practical. Advances in Kernel Methods - Support Vector Learning*. MIT-Press, 1999. 3.2.2

[59] T. Joachims. Transductive inference for text classification using support vector machines. In *Proc. International Conference on Machine Learning*, pages 200–209, 1999. 4.2.2, 4.2.2

[60] M. Kass, A. Witkin, and D. Terzopoulos. Snakes: Active contour models. *International Journal of Computer Vision*, 1(4):321–331, 1988. 2.4.1

[61] T.M. Keenan, A. Hooker, M.E. Spilker, N. Li, G.J. Boggy, P. Vicini, and A. Folch. Automated identification of axonal growth cones in time-lapse image sequences. *J. Neurosci. Methods*, 151(2):232–238, 2006. 2.3.1

[62] S.S. Kelly, C.B.S. Sola, M. de Lima, and E. Shpall. *Ex vivo* expansion of cord blood. *Bone Marrow Transplantation*, 44(10):673–681, 2009. 3.3.2

[63] M. Kim, S. Kumar, and V. Pavlovic. Face tracking and recognition with visual constraints in real-world videos. In *Proc. IEEE Conference on Computer Vision and Pattern Recognition*, pages 1–8, 2008. 1.2

[64] C.B. Kimmel, W.W. Ballard, S.R. Kimmel, B. Ullmann, and T.F. Schilling. Stages of embryonic development of the zebrafish. *Dev Dyn.*, 203(3):253–310, 1995. 1

[65] B. Kumar, A. Mahalanobis, and R.D. Juday. *Correlation Pattern Recognition*. Cambridge University Press, 2005. 3.3.1

[66] S. Kumar and M. Herbert. Discriminative random fields: A framework for contextual interaction in classification. In *Proc. IEEE International Conference on Computer Vision*, pages 1150–1157, 2003. 3.1.2, 3.2.3

[67] J. Lafferty, A. McCallum, and F. Pereira. Conditional random fields: probabilistic models for segmenting and labelling sequence data. In *Proc. International Conference on Machine Learning*, pages 282–289, 2001. 3.1.2, 3.2.3, 3.2.3

[68] I. Laptev and P. Pérez. Retrieving actions in movies. In *Proc. IEEE International Conference on Computer Vision*, pages 1–8, 2007. 1.2

[69] S. Lazebnik, C. Schmid, and J. Ponce. A sparse texture representation using local affine regions. *IEEE Trans. Pattern Anal. Mach. Intell.*, 27(8):1265–1278, 2005. 3.1.1

[70] A. Levin, D. Lischinski, and Y. Weiss. A closed form solution to natural image matting. *IEEE Trans. Pattern Anal. Mach. Intell.*, 30(2):228–242, 2008. 6.1.1

[71] K. Li and T. Kanade. Nonnegative mixed-norm preconditioning for microscopy image segmentation. In *Proc. International Conference on Information Processing in Medical Imaging*, pages 362–373, 2009. 2.1.1, 3.1.4, 3.4

[72] K. Li, E. Miller, L.E. Weiss, P.G. Campbell, and T. Kanade. Online tracking of migrating and proliferating cells imaged with phase-contrast microscopy. In *Proc. Comput. Vision Pattern Recognit. Workshop*, pages 65–72, 2006. 2.4.1

[73] K. Li, E.D. Miller, M. Chen, T. Kanade, L.E. Weiss, and P.G. Campbell. Computer vision tracking of stemness. In *Proc. IEEE International Symposium on Biomedical Imaging*, pages 847–850, 2008. 2.1.1, 3.1.1, 6.1.3, 6.2, 6.1.3, 6.3

[74] K. Li, E.D. Miller, M. Chen, T. Kanade, L.E. Weiss, and P.G. Campbell. Cell population tracking and lineage construction with spatiotemporal context. *Med. Image Anal.*, 12(5): 546–566, 2008. 2.4.1, 6.1, 6.1.2

[75] C.C. Liang, A.Y. Park, and J.L. Guan. *In vitro* scratch assay: a convenient and inexpensive method for analysis of cell migration *in vitro*. *Nat. Protoc.*, 2(2):329–333, 2007. 6.2.1, 6.2.1

[76] G. Lin, M.K. Chawla, K. Olson, J.F. Guzowski, C.A. Barnes, and B. Roysam. Hierarchical, model-based merging of multiple fragments for improved 3-d segmentation of nuclei. *Cytometry A*, 63(1):20–33, 2005. 1.1

[77] J. Lippincott-Schwartz and G.H. Patterson. Development and use of fluorescent protein markers in living cells. *Science*, 300:87–91, 2003. 1.1

[78] A-A Liu, K. Li, and T. Kanade. Mitosis sequence detection using hidden conditional random fields. In *Proc. IEEE International Symposium on Biomedical Imaging*, pages 580–583, 2010. 2.1.1, 3.1.2, 3.1.3, 3.1.4

[79] M.-Y. Liu, O. Tuzel, S. Ramalingam, and R. Chellappa. Entropy rate superpixel segmentation. In *Proc. IEEE Conference on Computer Vision and Pattern Recognition*, pages 2097–2104, 2011. 5.2.2

[80] D.G. Lowe. Distinctive image features from scale-invariant keypoints. *Int. J. Comput. Vision*, 60(2):91–110, 2004. 3.1.1, 3.2.1, 3.12, 3.2.2, 3.2.3

[81] V. Mahadevan, W. Li, V. Bhalodia, and N. Vasconcelos. Anomaly detection in crowded scenes. In *Proc. IEEE Conference on Computer Vision and Pattern Recognition*, pages 1975–1981, 2010. 1.2

[82] M. Marszalek, I. Laptev, and C. Schmid. Actions in context. In *Proc. IEEE Conference on Computer Vision and Pattern Recognition*, pages 2929–2936, 2009. 1.2

[83] I. Martin, H. Baldomero, A. Tyndall, D. Niederwieser, and A. Gratwohl. A survey on

cellular and engineered tissue therapies in europe in 2008. *Tissue Eng. Part A*, 16(8): 2419–2427, 2010. 3.3.2

[84] E. Meijering, O. Dzyubachyk, I. Smal, and W.A. van Cappellen. Tracking in cell and developmental biology. *Semin, Cell Dev. Biol.*, 20(8):894–902, 2009. 2.4, 2.4.1

[85] M.L. Mendelsohn, W.A. Kolman, and R.C. Bostrom. Initial approaches to the computer analysis of cytophotometric fields. *Ann. N. Y. Acad. Sci.*, 115:998–1009, 1964. 1.1

[86] M.L. Mendelsohn, W.A. Kolman, B. Perry, and J.M.S. Prewitt. Morphological analysis of cells and chromosomes by digital computer. In *6th IBM Medical Symposium*, 1964. 1.1

[87] K. Mikolajczyk and C. Schmid. Scale and affine invariant interest point detectors. *International Journal of Computer Vision*, 60(1):63–86, 2004. 1.2

[88] R. Möhle and L. Kanz. Hematopoietic growth factors for hematopoietic stem cell mobilization and expansion. *Seminars in Hematology*, 44(3):193–202, 2007. 3.3.2

[89] L.P. Morency, A. Quattoni, and T. Darrell. Latent-dynamic discriminative models for continuous gesture recognition. In *Proc. Computer Vision and Pattern Recognition*, pages 1–8, 2007. 3.1.2, 3.1.2, 3.1.2, 3.2.3, 3.2.5

[90] D.P. Mukherjee, N. Ray, and S.T. Acton. Level set analysis for leukocyte detection and tracking. *IEEE Trans. Image Process.*, 13(4):562–572, 2004. 2.4.1

[91] D.B. Murphy. *Fundamentals of Light Microscopy and Electronic Imaging*. John Wiley and Sons, Inc., 2001. 1, 1.1, 4.1.1, 5.1.2

[92] D.B. Murphy, R. Oldfield, S. Schwartz, and M.W. Davidson. Introduction to phase contrast microscopy, unpublished manuscript. http://www.microscopyu.com/articles/phasecontrast/phasemicroscopy.html. 4.1.1

[93] E.M. Nadel. Computer analysis of cytophotometric fields by cydac and its historical evolution from the cytoanalyzer. *Acta Cytologica*, 9:203–206, 1965. 1.1

[94] D. Needell and R. Vershynin. Signal recovery from incomplete and inaccurate measure-

ments via regularized orthogonal matching pursuit. *IEEE J. Sel. Top. Signa.*, 4(2):310–316, 2010. 5.1.3, 5.1.3, 2

[95] W. Ng, J. Li, S. Godsill, and J. Vermaak. A hybrid method for online joint detection and tracking for multiple targets. In *Proc. IEEE Aerosp. Conf.*, pages 2126–2141, 2005. 2.4.1

[96] D.L. Nikolić, A.N. Boettiger, D. Bar-Sagi, J.D. Carbeck, and S.Y. Shvartsman. Role of boundary conditions in an experimental model of epithelial wound healing. *Am. J. Physiol-Cell Ph.*, 291(1):C68–75, 2006. 6.2.1

[97] T. Ojala, M. Pietikäinen, and T.T.Mäenpää. Multiresolution gray-scale and rotation invariant texture classification with local binary pattern. *IEEE Trans. Pattern. Anal. Mach. Intell.*, 24(7):971–987, 2002. 4.1.2, 5.2.2

[98] D. Padfield, J. Rittscher, and B. Roysam. Coupled minimum-cost flow cell tracking. In *Proc. International Conference on Information Processing in Medical Imaging*, pages 374–385, 2009. 2.4.1

[99] D. Padfield, J. Rittscher, N. Thomas, and B. Roysam. Spatio-temporal cell cycle phase analysis using level sets and fast marching methods. *Med. Image Anal.*, 13(1):143–155, 2009. 2.1.1, 2.4.1

[100] J. Pan, T. Kanade, and M. Chen. Heterogeneous conditional random field: Realizing joint detection and segmentation of cell regions in microscopic images. In *Proc. IEEE Conference on Computer Vision and Pattern Recognition*, pages 2940–2947, 2010. 1.2

[101] J.B. Pawley. *Handbook of Biological Confocal Microscopy*. Springer, Berlin, 3rd edition, 2006. 1

[102] J. Pearl. *Probabilistic Reasoning in Intelligent Systems: Networks of Plausible Inference*. Morgan Kaufmann, 1988. 3.1.2, 3.2.3

[103] H. Peng. Bioimage informatics: a new area of engineering biology. *Bioinformatics*, 24 (17):1827–1836, 2008. 1

[104] W.H. Press, S.A. Teukolsky, W.T. Vetterling, and B.P. Flannery. *Numerical Recipes: The Art of Scientific Computing*. New York: Cambridge, 3rd edition, 2007. 2.4.1, 5.2.1

[105] J.M.S. Prewitt and M.L. Mendelsohn. The analysis of cell images. *Ann. N. Y. Acad. Sci.*, 128:1035–1053, 1966. 1.1

[106] D. Qi and M. Fu. Cardiomyocyte apoptosis in heart development: Methods and protocols. *Cardiovascular Development: Methods in Molecular Biology*, 843:191–197, 2002. 2.2

[107] H. Quastler and F.G. Sherman. Cell population kinetics in the intestinal epithelium of the mouse. *Exp. Cell Res.*, 17(3):420–438, 1959. 2.1

[108] A. Quattoni, M. Collins, and T. Darrell. Conditional random fields for object recognition. In *Proc. Neural Information Processing Systems*, pages 1097–1104, 2004. 3.1.2

[109] A. Quattoni, S. Wang, L. Morency, M. Collins, and T. Darrell. Hidden conditional random fields. *IEEE Trans. Pattern Anal. Mach. Intell.*, 29(10):1848–1853, 2007. 2.1.1, 3.1.2, 3.1.2, 3.1.3, 3.2.3, 3.3.1, 3.3.1, 4.1.2, 4.2.3

[110] P. Ramm, Y. Alexandrov, A. Cholewinski, Y. Cybuch, R. Nadon, and B.J. Soltys. Automated screening of neurite outgrowth. *J. Biomol. Screen.*, 8(1):7–18, 2003. 2.3.1

[111] J. Renströma, M. Krgera, C. Peschela, and R.A.J. Oostendorp. How the niche regulates hematopoietic stem cells. *Chemico-Biological Interactions*, 184(1–2):7–15, 2010. 3.3.2

[112] B. Ristic, S. Arulampalam, and N. Gordon. *Beyond the Kalman Filter: Particle Filters for Tracking Applications*. Artech House, 2004. 2.4.1

[113] M.W. Roomi, N.W. Roomi, B. Bhanap, M. Rath, and A. Niedzwiecki. Nutrient mixture inhibits in vitro and in vivo growth of human acute promyelocytic leukemia hl-60 cells. *Exp. Oncol.*, 33(4):212–215, 2011. 2.2

[114] S. Roweis and Z. Ghahramani. A unifying review of linear gaussian models. *Neural Comput.*, 11(2):305–345, 1999. 2.4.1

[115] H.A. Rowley, S. Baluja, and T. Kanade. Human face detection in visual scenes. In *Proc.*

Neural Information Processing Systems, pages 875–881, 1996. 1.2

[116] M.J. Rust, M. Bates, and X. Zhuang. Sub-diffraction-limit imaging by stochastic optical reconstruction microscopy (STORM). *Nat. Methods*, 3(10):793–796, 2006. 1.1

[117] B. Schölkopf, C.J.C. Burges, and A.J. Smola. *Advances in Kernel Methods: Support Vector Learning*. MIT Press, Cambridge, MA, 1999. 3.2.2, 3.2.2

[118] F. Sha, Y. Lin, L.K. Saul, and D.D. Lee. Multiplicative updates for nonnegative quadratic programming. *Neural Computation*, 19(8):2004–2031, 2007. 5.1.3, 7, 6.1.1

[119] H. Shen, G. Nelson, S. Kennedy, D. Nelson, J. Johnson, D. Spiller, M.R.H. White, and D.B. Kell. Automatic tracking of biological cells and compartments using particle filters and active contours. *Chem. Intell. Lab. Syst.*, 82(1-2):276–282, 2006. 2.4.1

[120] I. Smal, K. Draegestein, N. Galjart, W. Niessen, and E. Meijering. Particle filtering for multiple object tracking in dynamic fluorescence microscopy images: application to microtubule growth analysis. *IEEE Trans. Med. Imaging.*, 27(6):789–804, 2008. 1.1, 2.4.1

[121] H. Su, Z. Yin, T. Kanade, and S. Huh. Phase contrast image restoration via dictionary representation of diffraction patterns. In *Proc. International Conference on Medical Image Computing and Computer Assisted Intervention*, pages 615–622, 2012. 5.1, 5.1.4

[122] W.E. Tolles. Applications and methods of counting and sizing in medicine and biology. *Ann. N. Y. Acad. Sci.*, 99:231–334, 1962. 1.1

[123] K. Urish, J. August, and J. Huard. Unsupervised segmentation for myofiber counting in immunofluorescent microscopy images. In *ISC/NA-MIC/MICCAI Workshop on Open-Source Software*, 2005. 5.2.3

[124] A.M. VanHook. Focus issue: Organ development from beginning to end. *Sci. Signal.*, 1: eg10, 2008. 1

[125] P. Viola and M. Jones. Rapid object detection using a boosted cascade of simple features. In *Proc. Computer Vision and Pattern Recognition*, pages 511–518, 2001. 2.1.1, 3.2.2

[126] S.B. Wang, A. Quattoni, L.-P. Morency, D. Demirdjian, and T. Darrell. Hidden conditional random fields for gesture recognition. In *Proc. Computer Vision and Pattern Recognition*, pages 1521–1527, 2006. 3.1.2, 3.1.3, 3.2.4

[127] J. Wolf, W. Burgard, and H. Burkhardt. Robust vision-based localization by combining an image-retrieval system with monte carlo localization. *IEEE Trans. Robot.*, 21(2):208–216, 2005. 2.4.1

[128] H. Wu, H. Zhang, C. Wang, Y. Wu, J. Xie, X. Jin, J. Yang, and J. Ye. Genoprotective effect of hyaluronic acid against benzalkonium chloride-induced dna damage in human corneal epithelial cells. *Mol. Vis.*, 17:3364–3370, 2011. 2.2

[129] Y. Wu, J. Lin, and T.S. Huang. Analyzing and capturing articulated hand motion in image sequences. *IEEE Trans. Pattern Anal. Mach. Intell.*, 27(12):1910–1922, 2005. 2.4.1

[130] T. Xiang, S. Gong, and J. Ponce. Video behavior profiling for anomaly detection. *IEEE Trans. Pattern Anal. Mach. Intell.*, 30(5):893–908, 2007. 1.2

[131] F. Yang, M.A. Mackey, F. Ianzini, G. Gallardo, and M. Sonka. Cell segmentation, tracking, and mitosis detection using temporal context. In *Proc. International Conference on Medical Image Computing and Computer Assisted Intervention*, pages 302–309, 2005. 2.1.1, 2.4.1

[132] J.C. Yarrow, Z.E. Perlman, N.J. Westwood, and T.J. Mitchison. A high-throughput cell migration assay using scratch wound healing, a comparison of image-based readout methods. *BMC Biotechnol.*, 4(21), 2004. 6.2.1

[133] Z. Yin, T. Kanade, and M. Chen. Understanding the phase contrast optics to restore artifact-free microscopy images for segmentation. *Med. Image Anal.*, 16(5):1047–1062, 2012. 4.1.1, 4.1.1, 5.1.1, 5.1.2, 5.1.3, 5.1.4, 6.1.1, 6.1.1

[134] H. Zhao, H. Xu, X. Xu, and D. Young. Predatory stress induces hippocampal cell death by apoptosis in rats. *Neurosci. Lett.*, 421(2):115–120, 2007. 2.2

[135] C. Zimmer, B. Zhang, A. Dufour, A. Thebaud, S. Berlemont, V. Meas-Yedid, and J.-C.O. Marin. Can anti-migratory drugs be screened in vitro? a review of 2d and 3d assays for the quantitative analysis of cell migration. *IEEE Signal Processing Magazine*, 23(3):54–62, 2006. 2.4